UNIVERSITY of CALIFORNIA
Santa Barbara

Nitrogen-vacancy center ensembles in diamond: diamond growth and ensemble characterization for ensemble magnetometry

A dissertation submitted in partial satisfaction of the
requirements for the degree of

Doctor of Philosophy

in

Physics

by

Claire Allison McLellan

Committee in charge:

Professor Ania C. B. Jayich, Chair
Professor Mark Sherwin
Professor Leon Balents

June 2018

The dissertation of Claire Allison McLellan is approved:

Professor Mark Sherwin

Professor Leon Balents

Professor Ania C. B. Jayich, Chair

June 2018

This thesis is dedicated to Jimmy Chen and my parents for their infinite support and love.

Acknowledgements

Many people made my doctoral path possible. First and foremost, I need to thank my adviser, Prof. Ania Jayich. She has taught me how to be a experimental physicist. I have learned both experimental skills such as optics, nanofabrication, and machining in her lab as well as a deeper theoretical understanding of quantum physics. I greatly appreciate her always expecting more from me than I thought possible. Her open door, excellent feedback, and encouraging personality created a great space to grow as a physicist.

Next, I would like to thank my committee members Mark Sherwin and Leon Balents. Mark has taken the time during his office hours to give a range of advice and knowledge ranging from explaining how photonic crystals work as during my first year to career advice when looking for a post-doctoral position. I have enjoyed working on the Climate Task Force with Leon and appreciate his advice on my progress as a doctoral candidate.

My coworkers in the Jayich lab are phenomenal. I could not have asked for a better cohort of people to surround myself with every day. Bryan Myers was the most patient person with me. I am grateful for the many hours of acid cleaning of our diamond where he would calmly explain the difference between T_2^* and T_2 for the fifth time. He always had smart solutions to problems and was thorough with his experiments.

Preeti Ovartchaiyapong is best nanofabrication scientist I have met. His ability to make any nano-structure out of diamond is amazing. He taught me many recipes and techniques in the cleanroom which made this thesis possible.

Laetitia Pascal was the first person I worked with in the Jayich lab. She also taught me many nanofabrication techniques. I am grateful for her help in getting me started.

Ken Ohno was the first grower on the UCSB diamond growth tool. The quality of the diamond we grow is significantly in part to the time he put into the diamond growth plasma enhanced chemical vapor deposition (PECVD) tool during his doctoral studies. Ken taught me how to be a careful diamond grower. He is an excellent mix of physicist

and material scientist.

Kenny Lee has been with me every step of the way in the Jayich lab. He taught me how to build and optics experiment. His knowledge of the literature is excellent and always kept a fun atmosphere in the lab.

Alec Jenkins has always kept a calm demeanor and can handle any situation. I appreciate all the times he helped me with acid cleaning and nanofabrication.

Jeff Cady will always be the senior graduate student to me. His wit makes long work days pass by quickly. It has been very exciting to see the additions you made to the PSB confocal set-up.

Simon Meynell has an infectious enthusiasm. I am sad only to have gotten to work with you for one year. I have already learned a lot about material science techniques and theory from working with you. I am I left the growth tool in good hands with Simon and Jeff.

I haven't gotten to work with Zhiran as much as the other graduate students. I have enjoyed our conversations and am excited to see where your experiments in graduate school take you.

Amila Ariyatne is probably the wisest scientist I have met. I am impressed with his ability to try new things and combine expertise in many areas.

I am still in awe of Matt Pellicionne's ability to build an experiment. His method and organization is something I try to follow when building experiments (although notably not as well). I had much more fun working in PSB after Matt and Alec started building the cryo-setup.

There have been many excellent undergraduates and masters students and too many to list here, but there are a few who I would particularly like to mention and thank. The student with the best questions is Dolev. I always enjoy discussing experiment ideas with him due to Dolev's creativity and passion for NV centers. My first undergraduate intern

was Rusty who helped in the nascent stages of the TEM project and contributed to getting those experiments started. Gabriel built quite a few systems on the TIRF microscope that are still used, such as the GUI for the motor stage and the magnet holder. Thank you to Jungbae who helped us get started on some new equipment upstairs. I have also had the pleasure of mentoring a high-school student, Jacob. He helped get some simulations running and asked excellent questions. His enthusiasm for physics is a superb addition upstairs.

Last of the graduate lab members but certainly not least. Tim Eichhorn has been my partner in crime for the previous four years. He is the NMR/EPR expert in our lab and is incredible at getting lab equipment to work. He is a very deep thinker and creates ingenious experiments to probe aspects of our diamond we didn't think possible. I did a significant part of my thesis in collaboration with Tim.

All of the staff at UCSB are phenomenal, and there are a few staff members, in particular, I would like to thank. First, the building manager at UCSB Physics, Mike Deal, was always around when the building might be causing troubles. I am so lucky to have someone to call at 11:30 in the evening on a Saturday when the humidifier breaks and the lab humidity starts creeping towards 100%. UCSB Physics is lucky to have you! I greatly appreciate how much Jennifer Farrar cares about the graduate students. I'd like to thank Holly Woo with all of her help over at CNSI.

There are many excellent technical staff at UCSB, but Lee Sawyer and Deryck Stave, in particular, have been particularly helpful for this thesis. Lee kept the NCF cleanroom and helped me maintain the diamond growth chamber. Deryck helped keep the annealing chambers running was always very helpful when I wanted to try new things such as oxygen annealing.

I would like to take a few sentences to thank mentors from previous institutions. Professors Oana Jurchescu and Keith Bonin at Wake Forest encouraged me to pursue

research and always found time to help me grow as a student and person. The person who may have started this journey was my high school physics teacher, Allen Burton. He created a learning environment where I was taught to think creatively but with a mathematical mind. He encouraged me to learn past what he showed in the classroom. I don't think I would have pursued this career without the start I was given.

The people who have been with me the entire time throughout this journey are my parents. They have given me endless support for the past twenty-eight years. Their kindness and encouragement to keep going when graduate school was difficult helped me finish this program.

Finally, I am fortunate to have gone through the adventure of graduate school with Jimmy Chen. You made the adventure that much better by having someone to share the ups and downs of graduate school every day. I am looking forward to spending many more ups and downs of life with you in the future.

Curriculum Vitæ

Claire Allison McLellan

Education

2018 Ph.D., Physics, University of California, Santa Barbara

2015 M.A., Physics, University of California, Santa Barbara

2012 B.S., Physics, Wake Forest University, Winston-Salem NC

First author publications

"Fabrication of organic thin-film transistors by spray-deposition for low-cost, large-area electronics", Natalia A. Azarova, Jack W. Owen, **Claire A. McLellan**, Marsha A. Grimminger, Erik K. Chapman, John E. Anthony, Oana D. Jurchescu *Organic Electronics* 11, 12 (2010)

"Variation of the Side Chain Branch Position Leads to Vastly Improved Molecular Weight and OPV Performance in 4, 8-dialkoxybenzo [1, 2-b: 4, 5-b'] dithiophene/2, 1, 3-benzothiadiazole Copolymers", Robert C. Coffin, Christopher M. MacNeill, Eric D. Peterson, Jeremy W. Ward, Jack W. Owen, **Claire A. McLellan**, Gregory M. Smith, Ronald E. Noftle, Oana D. Jurchescu, David L. Carroll *Journal of Nanotechnology* 2011, (2011)

"Deterministic coupling of delta-doped nitrogen vacancy centers to a nanobeam photonic crystal cavity" Jonathan C. Lee, David O. Bracher, Shanying Cui, Kenichi Ohno, **Claire A. McLellan**, Xingyu Zhang, Paolo Andrich, Benjamin Aleman, Kasey J. Russell, Andrew P. Magyar, et al. *Applied Physics Letters* 105, 26 (2014)

"Patterned formation of highly coherent nitrogen-vacancy centers using a focused electron irradiation technique" **Claire A. Mclellan**, Bryan A. Myers, Stephan Kraemer, Kenichi Ohno, David D. Awschalom, Ania C. B. Jayich *Nano letters* 16, 4 (2016)

" Hyperfine-enhanced gyromagnetic ratio of a nuclear spin in diamond" S. Sangtawesin, **Claire A. McLellan**, Bryan A. Myers, Ania C. B. Jayich, David D. Awschalom, Jason R. Petta *New Journal of Physics* 18, 8 (2016)

"Using NV center ensembles for characterizing growth and NV formation techniques " Tim Eichhorn*, **Claire A. McLellan***, Ania C. B. Jayich *in Preparation* (2018)

* represents equal work contributed

Abstract

Nitrogen-vacancy center ensembles in diamond: diamond growth and ensemble characterization for ensemble magnetometry

by

Claire Allison McLellan

Magnetic sensing is a non-invasive imaging modality which is ubiquitous across length scales. For example, magnetic resonance imaging (MRI) is commonly performed in hospitals to image entire human organs. On the other end of the spectrum superconducting quantum interference devices (SQUIDs) are capable of nanometer scaled objects. However, both of these techniques have limitations. MRI cannot be used on small length scales while SQUIDs must be operated at cryogenic temperatures and thus are incompatible with biological samples. A magnetometer with both biocompatibility and high spatial resolution could have many exciting applications. For example, such a magnetometer could image the magnetic signals associated with a neuron's action potential The most advanced methods of measuring neuronal activity, including patch clamping and voltage sensitive dyes, rely on sensing electric fields. However, the highly invasive nature of patch clamping and the toxicity of voltage sensitive dyes limits these methods. Alternatively, neurons produce longitudinal current an correspondingly small magnetic fields when firing an action potential. These magnetic fields can be used to infer the

neuron's behavior. Sub nanoTesla/$\sqrt{\text{Hz}}$ is necessary for sensing neuron action potentials. This thesis focuses building a biocompatible magnetometer based on the nitrogen vacancy (NV) center in diamond, improving the sensitivity of the magnetometer, and applying it to biological systems.

The NV center is a point defect with an atom-like energy structure that is sensitive to magnetic fields. Uniquely the NV center retains its quantum properties under ambient conditions and room temperature. Because the NV center's energy structure is optically addressable and diamond is biocompatible, NV centers are an exciting and unique candidate to measure biological magnetic fields. An outstanding challenge for using NV centers is improving the sensitivity of NVs to make them useful sensors for biological samples. The fundamental sensing limit for a NV ensemble (η) scales inversely with the number of centers in the sensing volume (N) and, because it is a quantum sensor, scales with the inverse of its coherence time (T_2^*). $\eta \propto \frac{1}{\sqrt{NT_2^*}}$. To achieve the requisite magnetic sensitivity, we take two main approaches: increasing the density of coherent NV centers, and further increasing coherence using engineered control pulses to decouple the NV from its environment. Chapter 2 describes the basic underlying physics of an NV center which is used for the magnetometry experiments.

In order to create a dense and coherent NV center ensemble, I developed an NV center creation technique which combines plasma enhanced chemical vapor deposition (PECVD) diamond growth with electron irradiation from a transmission electron microscope (TEM). Nitrogen is incorporated during growth, and vacancies are formed by the

electron irradiation. Subsequent annealing of the diamond forms the NV center. The growth process is described in chapter 3. By using 145 keV electrons, we limit excess damage to the diamond lattice, maintaining long coherence times in our diamond while increasing the density of our NV ensemble. Additionally, this formation technique also allows us to measure the displacement energy of a carbon atom in the diamond lattice directly. Electron irradiation techniques and analysis are described in chapter 4.

With members of the Jayich lab, I built a wide-field total internal reflection microscope equipped with microwaves to probe the quality of our NV center ensembles and do magnetometry experiments. The equipment used to detect ensembles of NV centers is described in chapter 5.

One of the primary sources of environmental decoherence is the ensemble of nitrogen atoms not converted to NV centers known (P1 centers). The P1 centers are paramagnetic and thus can couple to NV center, decohering them. These spins are difficult to measure due to their small spin number. To understand the limiting factors of our sensitivity we, Tim Eichhorn and I, developed a recipe to characterize the spin-bath in our diamond. Using double electron-electron resonance (DEER) techniques we can give quantitative values to spin bath concentrations in our diamond. These techniques are described in chapter six.

We have integrated our coherent NV ensembles in diamond with total internal reflection (TIRF) optics, microwave electronics, and patch clamping equipment to create a biocompatible magnetometer. Using the set-up we demonstrate a proof-of-principle

by plating Aplysia Californica neurons on diamond and have stimulating and recording action potentials with patch-clamp electronics while simultaneously recording the NV fluorescence. The current advances toward bio-imaging in the Jayich lab are described in chapter 7.

This thesis concludes in chapter 8 with a path towards improving the sensitivity further to use this magnetometer to probe neurological networks and other condensed matter systems. To further improve the sensitivity of our grown diamond sample, we use spin control measurements to decouple the NV center ensemble from its environment. By applying carefully timed radio frequency pulses to the P1 center, we decouple the P1 centers from the NV centers, thus eliminating this source of decoherence. I also describe the effects of temperature changes, strain and electric field noise on the sensitivity of our NV ensemble and how to mitigate their decoherence. With these advances, we have achieved a 1 nT/$\sqrt{\text{Hz}}$ sensitivity in a 5x5 μm^2 area.

Permissions and Attributions

1. Many of the growth parameters and theory in Chapater 3 came from the thesis of Kenichi Ohno [84].

2. The content of Chapter 4 and section 6.10 of are reproduced with permission from C.A. McLellan *et al* Nano Letters 2016, 16, 4, 2450-2454. Copyright (2016) American Chemical Society.

3. The wide-field microscope in Chapter 5, the experiments in Chapters 7 and 8, and the ensemble measurements in Chapters 3 and 4 are the result of a collaboration with Tim Eichhorn

4. The confocal and microwave electronics designs in Chapter 5 were based off of prior designs by Bryan Myers, Kenneth Lee, and Preeti Ovartchaiyapong.

5. We borrowed the patch clamp equipment in Chapter 5 and received guidance for the experiments in Chapter 7 from Prof. Carol Vandenberg

6. The procedures in Chapter 7 were adapted from the Glanzman Lab at UCLA.

7. We performed the *Aplysia californica* dissections in the Oakley lab with the help of Desmond Ramirez.

Contents

List of Figures

List of Tables

Chapter 1

Magnetometry

Magnetometry is a class of techniques to sense magnetic fields. Magnetic field spatial mapping can be used for non-invasive imaging [15], detecting chemical structures [93], and probing fundamental physics in materials [82]. There are a range of very powerful platforms used for magnetic sensing. Although this thesis is focused on the the nitrogen vacancy (NV) center in diamond, I will start with an overview of different magnetic sensing platforms and their strengths and limitations. Please note that sensitivity and spatial resolution are inverse to one another. When I note figures of merit for different magnetometers the devices with state of the art spatial resolution with the same platform usually do not have the state of the art sensitivity for that platform.

1.1 Compass

Invented by the Han dynasty in China between 300 and 200 B.C. the compass is the original magnetometer [70]. Consisting of a magnetized needle which will align it self to the Earth's magnetic field, the compass has been used as a navigation tool for millennia.

1.2 Nuclear magnetic resonance

Nuclear magnetic resonance (NMR) and the closely related magnetic resonance imaging (MRI) are a powerful form of magnetometry for detecting oscillating magnetic fields[12]. It was first developed in the early twentieth center and is still being developed to this day. It has led to many breakthroughs in physics, chemistry, and biology [12]. NMR consists of applying a large magnetic field to polarize the nuclear spins of a system. Then, applying resonant microwaves and tuning the magnetic field, it is possible to detect the Larmor frequency of precessing nuclear spins. Because the Larmor precession is different for each nuclear species, one may use this information to extract chemical and structural information [93]. The frequency of the precessing spins is usually on the order of 1 MHz to 1 GHz depending on the external magnetic field applied [93].

1.2.1 Magnetic resonance imaging

MRI is closely related NMR. A field gradient is placed on top of the external mangnetic field. The precessing spins have a gradient of Larmor frequencies. The frequency change

over space gives the user a 3-d image of nuclear spins. This technique is commonly used in hospitals to noninvasively detect abnormalities in the human body [15].

1.3 Electron paramagnetic resonance

Electron paramagnetic resonance (EPR) is the close cousin of NMR where electron spins are detected rather than nuclear spins. Due to the gyromagnetic ratio of an electron being three orders of magnitude larger in electrons this form of spectroscopy is highly sensitive [102]. Sensing the NV center, which is the focus of this thesis, can be considered a sub-field of EPR. The NV center is a single electron spin which is probed to discover information about its environment. Many of the techniques used in this thesis were first developed for traditional EPR experiments.

1.4 Atomic vapour cells

Atomic vapour cells are some of the most sensitive magnetometers available. They consist of a gas of resonant atoms such as rubidium, cesium or potassium. This gas is then pumped and probed with lasers on resonance to detect shifts in the atomic energy levels due to magnetic field changes [16]. The sensitivities of these magnetometers have reached 10^{-15} T/$\sqrt{\text{Hz}}$ [61] and the spatial resolution goes down to millimeters [6].These magnetometers are great at detecting small magnetic fields where spatial resolution is not a critical parameter.

1.5 Superconducting quantum interference devices

Superconducting quantum interference devices (SQUIDs) offer an excellent range of spatial resolution and sensitivities. A SQUID consists often consists of a ring of superconducting metal with a Josephson junction. One measures a voltage across a small resistor bridging a loop of superconducting material with a persistant current. Changes in voltage describe changes in the external magnetic field. This style of magnetometer can have spatial resolution in the 100s of nm [57] and sensitivities as good as $< 10^{-18}$ T/$\sqrt{\text{Hz}}$ [37] although not at the same time. A challenge with SQUIDs is the need to be at cryogenic temperatures. The temperature constraint limits the bio-compatibility of these sensors.

1.6 Hall Bars

A Hall bar uses the phenomena that the voltage across a piece of metal will change under a magnetic field [43]. With scanning probe techniques it is possible to detect magnetic fields on the length scales of ≈ 100 nm [19].

1.7 NV Centers in diamond

The nitrogen vacancy (NV) center in diamond is a point defect with an atomic like energy structure [32]. The NV ground state is a spin 1 system which can be optically spin polarized and optically read out. The energy levels of the ground state change with external magnetic field. With millisecond long coherence times at room temperature

and all optical preparation and readout, the NV center has become a very promising magnetometry platform.

Devices with single NV centers and ensembles of NV centers have been demonstrated and both have been useful for different types of magnetometry.

1.7.1 Single NV centers

A single NV center has superb spatial resolution. It is capable of doing NMR studies with the sensing volume of a few nm^3 [72, 107]. When placed inside a scanning probe the NV center can be used to image magnetic phenomena [71, 90, 118, 115].

The properties of the NV center which make it an excellent magnetometer also make it promising for other quantum technologies [120, 65]

1.7.2 NV center ensembles

Where the single NV center shines is its high spatial resolution, but it is slow to map the magnetic field in large area ($> 0.1\mu m^2$). To probe a large viewing area quickly it is beneficial to use ensembles of NV centers. One also gains in the sensitivity of the magnetometer because the sensitivity scales with $1/\sqrt{N}$, where N is the number of NV centers used in the measurement. Ensembles of NV centers have already been used to probe biological signals [9], NMR signals [42], copper ions [104], and current flow in graphene [116].

There are also other uses for ensembles of NV centers such as memory [30] which are

outside the scope of this thesis.

1.8 Other magnetometry methods

There are many magnetometry methods which I am not going into detail such as magneto optical Kerr effect (MOKE) microscopy [92], magnetic force microscopy [99], and magnetometry with organic materials [5]. Magnetometry is a very useful field with many interesting platforms. I encourage the reader to explore magnetometry more.

1.9 Choosing the correct platform for the application

With all of these platforms it is important to choose the correct magnetometer for the problem at hand. While NMR and EPR are great at detecting precessing magnetic fields, they struggle mapping out static fields because the detector is usually a resonator designed to retrieve a specific frequency. While scanning probe techniques like scanning SQUID, single NV centers, and scanning Hall probes have excellent spatial resolution, mapping out large areas is tedious and it is difficult to correlate magnetic field fluctuations in space and time. Atomic vapour cells have excellent sensitivities and have been employed in many environments but their spatial resolution is limited to a few mm^3. NV center ensembles are a promising candidate for sensing static or quasi-static magnetic fields on length scales limited by the diffraction limit of light (300 nm) and with viewing

areas of a standard wide field microscopy ($> 100s\text{mm}^2$). Combining these properties with the bio compatibility of diamond will allow magnetometry to probe phenomena which was difficult if not impossible to probe before. An outstanding challenge is improving the sensitivity of the NV ensembles to be useful sensors.

This thesis focuses on how to improve upon the sensitivity of ensemble magnetometers and integrate them with biological sensing to image biological magnetic phenomena.

Chapter 2

Nitrogen vacancy center ensembles in diamond

The nitrogen vacancy (NV) center in diamond is a point defect consisting of two adjacent lattice sites being replaced with a nitrogen and a vacancy, see figure 2.1. Although NV center ensembles have been studied since before the 1970s [69] many research groups started studying the NV centers once a single NV center was isolated and its spin state was read out and manipulated [45]. Uniquely, the NV center retains its quantum properties under ambient conditions and room temperature. In 2009 it was shown that a single NV center could possess a coherence time exceeding a second at room temperature [7]. Because the NV center's energy structure is easily optically addressable and maintains a long coherence time, it has become a candidate for many quantum technologies. Many excellent theses have been written about the NV center [22, 94, 3] and its applications

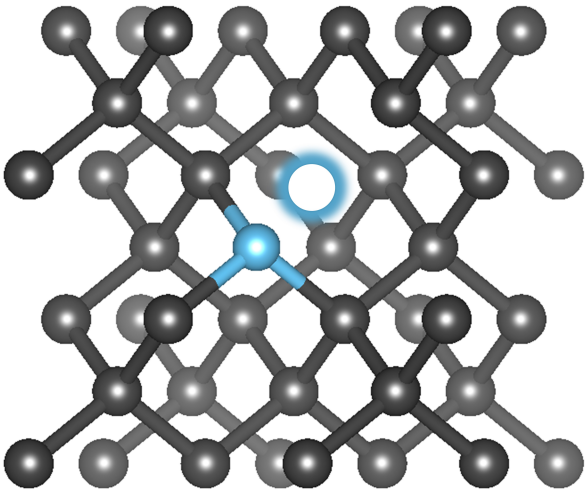

Figure 2.1: Diamond crystal structure with a nitrogen vacacancy center defect. The grey atoms are carbon and the blue atom is a nitrogen. The vacancy is represented by a white circle with a blue halo. The figure was created using Vesta software [78]

in quantum computing [120], Hybrid quantum systems [87, 66], and quantum assisted sensing with a single NV [80]. This sampling is just a small selection, there are many others. This thesis focuses on how small ($10^3 - 10^6$ total spin number) NV center ensembles can be used as high sensitivity magnetometers with spatial resolution which is diffraction spot limited.

This chapter gives the basic theory of the NV center as it pertains to ensemble magnetometry. I will discuss also simple quantum control and readout protocol.

2.1 NV center energy structure and ground state Hamiltonian

The NV center demonstrates C_{3v} symmetry. When negatively charged the electronic energy structure can be derived from symmetry arguments while exact values for energy spacing have been found experimentally [32, 94]. Figure 2.2 shows a schematic of the ground state ($^3A_2$), excited state (^3E), and meta-stable states ($^1A_1$, ^1E). The labels come from group theory. More detail on the symmetry arguments and group theory for NV centers can be found in [94]. On the right in Fig. 2.2 is the fine and hyperfine structure of the ground state. The ground state can be described by the canonical spin Hamiltonian of a trigonal defect [32, 111]. An ensemble of NV centers can be treated with the same Hamiltonian as the single NV center. Inhomogeneity between the NV center's environment in the ensemble is introduced as a decoherence term.

$$\hat{H}_{NV} = D(\hat{S}_z^2 - \frac{S(S+1)}{3}) + A_{gs}^{\parallel}\hat{S}_z\hat{I}_z + A_{gs}^{\perp}(\hat{S}_x\hat{I}_x + \hat{S}_y\hat{I}_y) + P_{gs}\left(\hat{I}_z^2 - \frac{I(I+1)}{3}\right) \quad (2.1)$$

S is the total spin number. $\hat{S}_z, \hat{S}_x, \hat{S}_y$ are the spin matrices for a spin 1 system. $A_{gs}^{\parallel}$ and $A_{gs}^{\perp}$ are the axial and no-axial magnetic hyperfine parameters for the ground state. P_{gs} is the nuclear electric quadrupole parameter. D, 2.872 GHz, is the crystal field splitting of the spin-triplet caused by electronic spin-spin interactions [32]. $A_{gs}^{\parallel}$ and $A_{gs}^{\perp}$ for ^{15}N have been measured to be 3 MHz [38]. $A_{gs}^{\parallel}$ and $A_{gs}^{\perp}$ for ^{14}N have been measured to be 2.3 MHz and 2.1 MHz respectively [48]. The nuclear-electronic quadrupole value

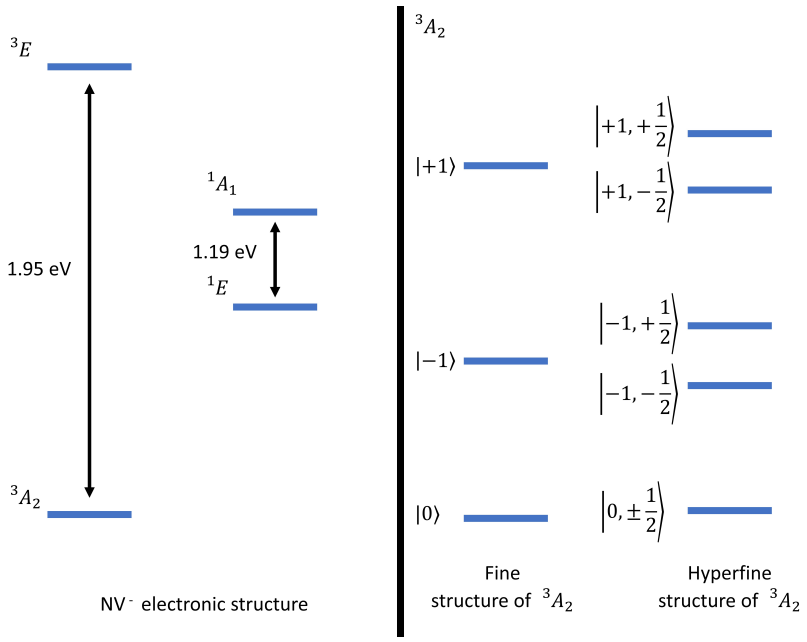

Figure 2.2: Energy diagram of the NV^- center. The image on the left is the general structure of the ground and excited state. The diagram on the right is the ground state spin 1 system fine structure and hyperfine structure.

is 5 MHz [48].Nitrogen 14 has a nuclear electronic quadrupole moment and nitrogen 15 does not.

2.1.1 NV coupling to external fields

The NV center ensemble energy levels can be further modified by coupling to external fields. Equation 2.2 shows how the NV centers energy structure is modified by an external magnetic field. μ_B is the Bohr magneton and $\overrightarrow{B}$ is an external magnetic field. H_{dipole} takes into account the coupling of the NV center ensemble to the P1 electron paramagnetic spin bath and the ^{13}C nuclear spin bath. Dipolar coupling will be discussed in further chapters where I demonstrate density measurements of the dipolar spin bath. The NV center can also couple to temperature (T), strain (d), and electric fields (E). For the purposes of

this thesis they will be ignored. Please see other theses and review papers for a more detailed discussion on coupling to temperature, strain and electric fields [87, 66, 32].

$$H_{\text{sensing}} = \mu_B g_{gs}^{\parallel} \hat{S}_z B_z + \mu_B g_{gs}^{\perp} (\hat{S}_x B_x + \hat{S}_y B_y) + H_{\text{dipole}} + ...(T, d, E) \tag{2.2}$$

2.2 Optically detected magnetic resonance

Critical to the usefulness of the NV center as a magnetometer is the simple optical preparation and readout of the ground state electronic spin. The phenomenon of optical preparation and readout comes from the spin selective coupling to the meta-stable states. The ground state is a spin triplet consisting of a 0 spin state, $|0\rangle$, and the spin 1 state, $|\pm 1\rangle$. Under excitation by photons with energy above 1.94 eV (637 nm, 540 THz) the $|0\rangle$ state will be excited and decay back into the ground state, producing a photon ranging from 620 - 800 nm in wavelength. The $|\pm 1\rangle$ states will go through the non-radiative meta-stable states about 1/3 of the time during excitation. The meta-stable states are long lived (400 ns) compared to the excited state (10 ns) [117]. This pathway makes the NV center fluoresce fewer photons compared to the $|0\rangle$ state. The meta-stable states are not spin conserving and the NV center will decay to the $|0\rangle$ state. By detecting the number of photons collected in a short window of time (400 ns - 10 μs depending on excitation power) it is possible to detect the spin state of the NV center [117] . By leaving the laser on the NV center will become polarized into the $|0\rangle$ state. This class of measurements is called optically detected magnetic resonance (ODMR).

2.2.1 Continuous wave electron spin resonance

The most simple way to apply ODMR to probe the NV center's energy spectrum is to perform continuous wave electron spin resonance (CW-ESR). As the name implies the laser is continuously exciting the NV center while microwaves are being applied and photons are collected . The microwave frequency is swept and as it comes into resonance the fluorescence of the NV center will drop. Figure 2.3 demonstrates how to use CWESR to detect the spin energy levels of the NV center. Shifts in the energy levels are caused by changes in the external magnetic field (or electric field, temperature etc.) and can be used to sense the external magnetic field.

2.2.2 Sensitivity of ODMR

It is possible to optimize the CWESR for magnetic field sensing by tuning in the microwave power and laser power for counts, contrast, and linewidth. [33, 91]

The optimized sensitivity for an ensemble of NV centers with Lorentzian line shape is shown in Eqn. 2.3.

$$\eta_{ESR} = \frac{1.53\hbar}{g\mu_B} \frac{1}{\alpha\sqrt{\beta T_2^*}} \tag{2.3}$$

α is the contrast of the CWESR peaks, β is the total counts measured, and T_2^* is the coherence time of the spin and is inversely related to the linewidth. The correction factor 1.53 comes from the Lorentzian profile of the NV centers energy levels. Increasing the number of NVs (N) in the ensemble while maintaining linewidth and contrast increases

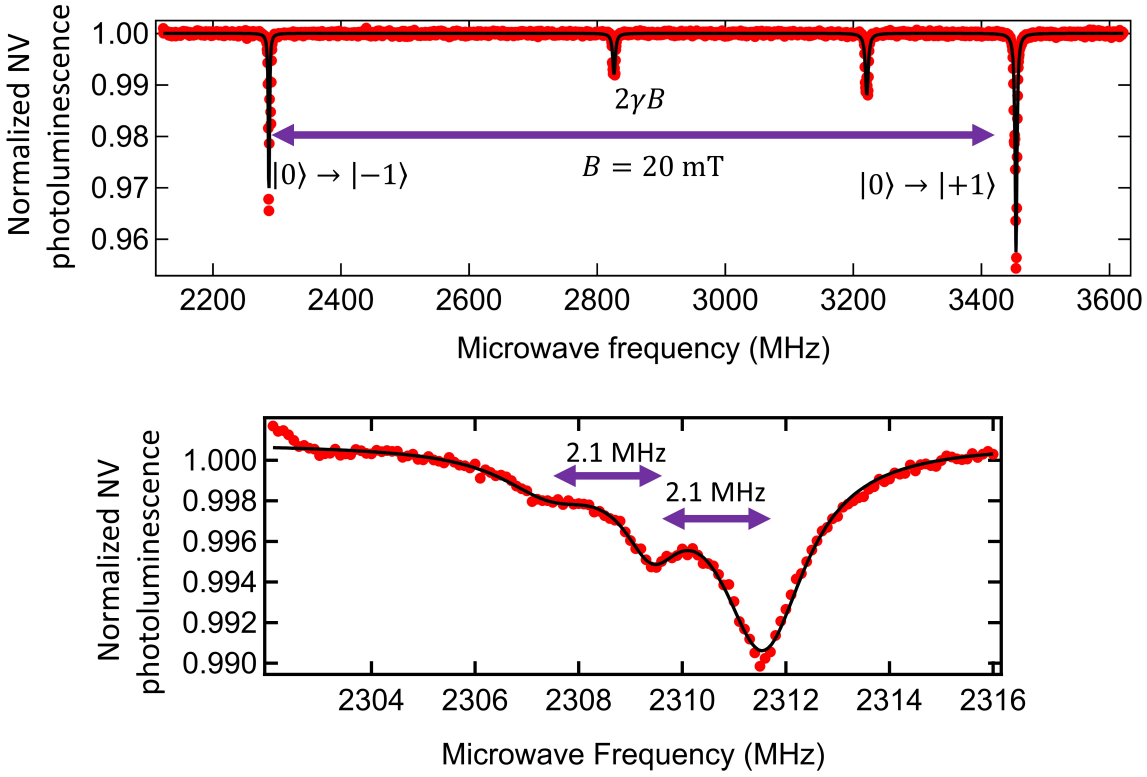

Figure 2.3: CWESR spectrum of an ensemble of NV centers. The top plot shows the entire spectrum. One NV orientation is aligned to the external magnetic field. The aligned NV center ensemble's transitions are labeled. The misaligned NV centers have overlapping spectrum and are the two smaller peaks. They are smaller and shifted from being centered on 2.87 GHz due to mixing from the perpendicular magnetic field. The bottom plot is a zoom in of the $|0\rangle \rightarrow |-1\rangle$ transition showing the hyperfine structure for the ^{14}NV ensemble. The nuclear spin is slightly hyper polarized, which causes the three hyperfine peaks to be different depths.

the the counts detected proportionally. This method of detecting magnetic field improves in sensitivity by $\frac{1}{\sqrt{N*T_2^*}}$

2.3 Coherent manipulation of the NV center spin

The NV center is considered a quantum sensor because it can be coherently manipulated. Quantum control protocols allow for more sensitive measurements of the NV center's environment compared to the CWESR method, which is not a quantum sensing protocol. This section gives a brief introduction to manipulating the spin state of the NV center with microwaves, how to theoretically treat the NV center, and three basic quantum protocols used often in this thesis: the Rabi, Ramsey and Hahn echo experiments. For the curious reader a useful reference material on the rotating wave approximation, density matrix formalism, the Rabi experiment, and other quantum control protocols is the textbook *Introductory Quantum Optics* by Gerry and Knight [40].

2.3.1 NV center interaction Hamiltonian

First, under large B_z one may treat the NV center as a quasi 2-level system between the $|0\rangle$ and the $|-1\rangle$ or between the $|+1\rangle$ states. When introducing microwaves to the system the interaction Hamiltonian becomes

$$H_{NV} = \hbar D(\sigma_z^2) + \hbar \mu_B g B_z \sigma_z + 2\hbar\Omega \cos(\omega_1 t)\sigma_x \tag{2.4}$$

where σ_x and σ_z are Pauli matrices, Ω is the Rabi frequency of the spins, which is

proportional to the strength of the magnetic field, and ω_1 is the frequency of the applied microwaves. This Hamiltonian uses Zeeman splitting from Eqn. 2.1 and the magnetic field interaction along the z-axis from Eqn. 2.2

Rotating wave approximation

To simplify this Hamiltonian even further, let us bring the Hamiltonian into the rotating frame. Using the unitary matrix, U_0, which describes the rotating driving field, the Hamiltonian can be transformed to the rotating frame in the following way.

$$U_0 = \begin{bmatrix} 1 & 0 \\ 0 & e^{-i\omega_1 t} \end{bmatrix} \tag{2.5}$$

$$\tilde{H}_{NV} = i\hbar \frac{\partial U_0}{\partial t} U_0^\dagger + U_0 H_{NV} U_0^\dagger \tag{2.6}$$

$$\tilde{H}_{NV} = \frac{\Omega}{2}\sigma_x + \delta\sigma_1 \tag{2.7}$$

Where δ is the offset of the microwave frequency to the transition frequency and σ_1 is the one state matrix. The one state matrix causes precession when driving off resonance.

$$\delta = D + \omega_0 - \omega_1 \tag{2.8}$$

$$\sigma_1 = \begin{bmatrix} 0 & 0 \\ 0 & 1 \end{bmatrix} \tag{2.9}$$

2.3.2 Density matrix under rotation

Using this Hamiltonian it is possible to see how a spin will evolve after a rotation by microwaves are applied and in the presence of a magnetic field. To simulate each experiment one starts with a polarized density matrix, then apply a Hamiltonian for the amount of time that it does not change. When the Hamiltonian changes in time the new Hamiltonian is applied. At the end of the sequence, one read outs the state of the NV center by taking the trace of the final density matrix after applying a projection along a measurement axis.

The NV center can be prepared into the $|0\rangle$ state so the starting density operator is

$$\rho_0(t=0) = \begin{bmatrix} 1 & 0 \\ 0 & 0 \end{bmatrix} \tag{2.10}$$

The time evolution unitary matrix, $U_N(t)$, when the Hamiltonian is constant in time is

$$U_N(t) = \exp\left(-\frac{i}{\hbar}\int_{t_{\text{initial}}}^{t_{\text{final}}} d\tau H_N(\tau)\right) \tag{2.11}$$

The density matrix changes over time by

$$\rho(t) = U_N(t-t_{n-1})...U_2(t_2-t_1)U_1(t_1)\rho(0)U_1^\dagger(t_1)U_2^\dagger(t_2-t_1)...U_N^\dagger(t-t_{N-1}) \tag{2.12}$$

The final spin state of the NV center is found by taking the trace of the density

operator projected along σ_y, σ_0 or σ_1. The trace taken depends on the measurement and which projection is finally measured.

$$NV_{\text{State}} = tr(\rho(t)\sigma_{(y,z,1,or0)} \tag{2.13}$$

2.3.3 Rabi experiment

The Rabi experiment consists of applying microwaves pulses to the NV center with varying time lengths and reading out the state of the NV center. Figure 2.4 demonstrates the sequence used for preparation microwave application and readout.

$$\rho(t) = U_1(t)\rho(0)U_1^{\dagger}(t) \tag{2.14}$$

Where the Hamiltonian used for U_1 is found in Eqn. 2.6 The probability of being found in the $|0\rangle$ or $|1\rangle$ states is

$$P_{|0\rangle}(t) = Tr(\sigma_0\rho(t))P_{|0\rangle}(t) = \frac{\delta^2}{\Omega^2+\delta^2} + \frac{\Omega^2}{\delta^2+\Omega^2}\cos^2(\frac{t}{2}\sqrt{\Omega^2+\delta^2}) \tag{2.15}$$

$$P_{|1\rangle}(t) = Tr(\sigma_1\rho(t))P_{|1\rangle}(t) = \frac{\Omega^2}{\delta^2+\Omega^2}\sin^2(\frac{t}{2}\sqrt{\Omega^2+\delta^2}) \tag{2.16}$$

Because the NV center is bright in the $|0\rangle$ state and dark in the $|1\rangle$, the oscillations in Fig. 2.4 show the oscillations between the two states. Later in the text I will discuss calibrating a Rabi to take into account B1 in homogeneity and linewidth to properly

calibrate the π flip.

2.3.4 Ramsey experiment

A Ramsey consists of applying a microwave pulse for so the spin is in a superposition of the $|0\rangle$ and $|1\rangle$ states called a $\pi/2$ pulse. If the pulses are applied off-resonance the spin will start to precess in the rotating frame. This precession rate is proportional to the offset frequency. After a given time another $\pi/2$ pulse is applied and the state is readout. I Small changes in the frequency of the spin due to an external change in magnetic field will result in a different phase accumulated. The decay time of this measurement is called the T_2^*. The decay occurs due to fluctuations in the energy levels of the NV center due to inhomogeneous magnetic or electric fields or temperature. This decay is sometimes called a dephasing.

The sensitivity η_{Ramsey} for this sequence is calculated in Pham's thesis [91] and seen in equation 2.17. One gains about a factor of 5 in sensitivity compared to CWESR because higher laser powers and microwaves can be used, increasing the contrast and count rate of the NV center.

$$\eta_{Ramsey} = \frac{\hbar}{g\mu_B} \frac{1}{\alpha\sqrt{\beta T_2^*}} \tag{2.17}$$

The fit used in figure 2.5 is

$$y_0 + A_1 \cos(2\pi\delta_1 + \phi_1) * \exp(-(t/T_{2_1}^*)^{-n_1}) + A_2 \cos(2\pi\delta_2 + \phi_2) * \exp(-(t/T_{2_2}^*)^{-n_2}) \tag{2.18}$$

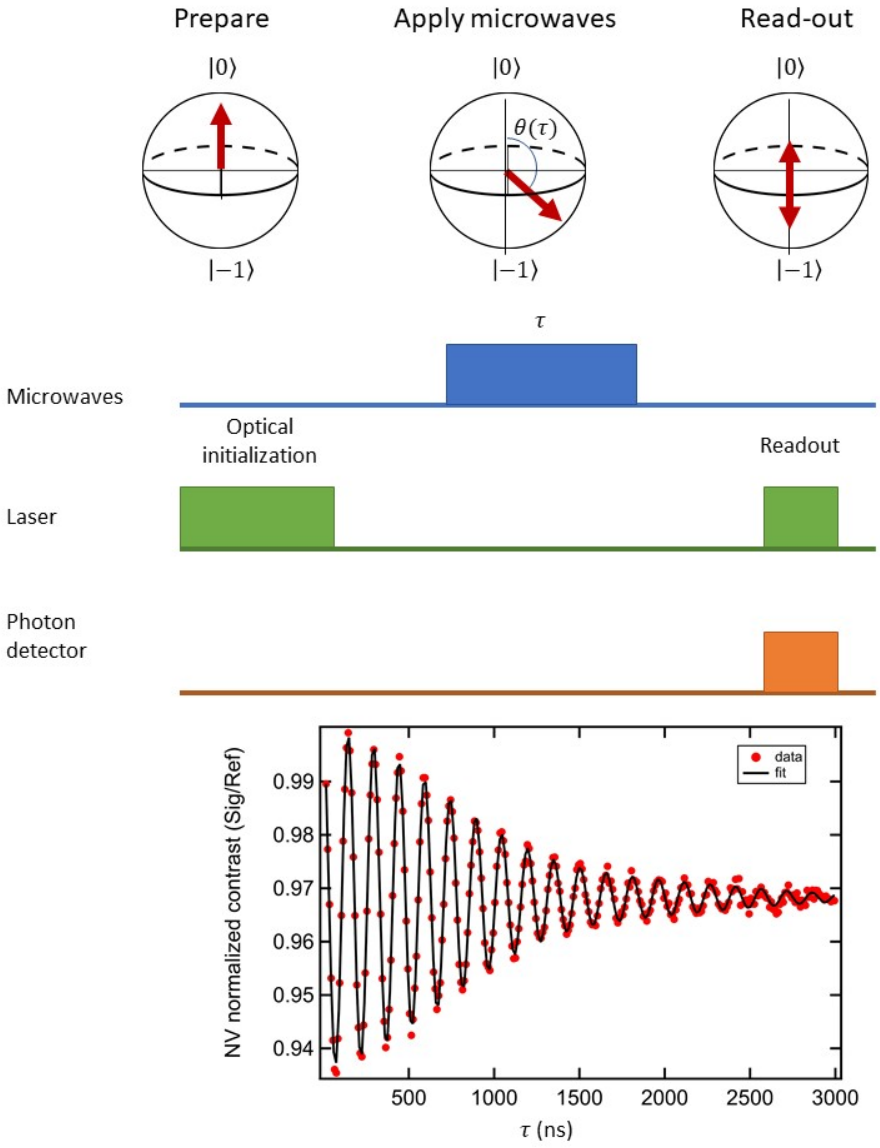

Figure 2.4: Rabi experiment: The top schematic shows how the a laser optically initializes the NV center. A microwave pulse of varying length is applied. Then the spin state is optically read out. Below is the result of the Rabi experiment. The points of lowest contrast are when the spin has fully rotated to the $|1\rangle$ state and is called a π pulse. The fit to the data is described in the text

This measurement was done by finding the difference between the $|0\rangle$ and $|1\rangle$ projections. If this measurement is perfectly balanced when the signal has totally decayed the projection is the same and the offset y_0 should be 0. A_1 and A_2 are amplitudes of the signal in photon counts. δ_1 and δ_2 are the offset frequency of the driving frequency to the resonance frequency. $T^*_{2_1}$ and $T^*_{2_2}$ are the coherence times for both resonance lines being driven. ϕ_1 and ϕ_1 are phase offsets of the signal. n_1 and n_2 are the exponential factor going into the decay. For a perfectly Markovian bath this exponential factor should be 1 [96]. Because we achieve our best fit for $n \neq 1$ we can assume we do not have a Markovian bath. The values of the fit parameters in firgure 2.5 are

- $y_0 = 0.70 \pm 3$photon counts
- $A_1 = 1830 \pm 90$photon counts
- $A_2 = 2670 \pm 100$photon counts
- $\delta_1 = 0.0010 \pm 0.0000013$GHz
- $\delta_2 0.004 \pm 0.0000008$GHz
- $\phi_1 = 0.22 \pm 0.013$
- $\phi_2 = 4.25 \pm 0.009$
- $T^*_{2_1} = 900 \pm 90$ns
- $T^*_{2_2} = 960 \pm 70$ns

- $n_1 = 0.56 \pm 0.03$
- $n_2 = 0.56 \pm 0.02$

2.3.5 Hahn echo experiment

Finally, it is possible to decouple static components of the magnetic field causing dephasing by applying dynamical decoupling sequences. The most simple of these sequences is the Hahn Echo, where a π pulse is applied in between the the Ramsey sequence as seen in figure 2.6. The coherence for the NV ensemble lasts longer because it is now decoupled from static sources of dephasing. This sequence is not sensitive to static magnetic fields. One can couple in specific DC signals into a Hahn Echo to better isolate and understand the NV ensemble's environment. This trick will be used in further in the double electron-electron chapter.

The Hahn Echo data shows a small oscillation, which comes from precessing nuclear ^{13}C spins [21]. This signal is small and most data will be taken at the nodes of the Hahn Echo sequence for the rest of the thesis.

The fit used for Hahn Echos when only fitting the nodes of ESEEM is

$$y_0 + A * \exp\left(-(t/T_2)^n\right) \tag{2.19}$$

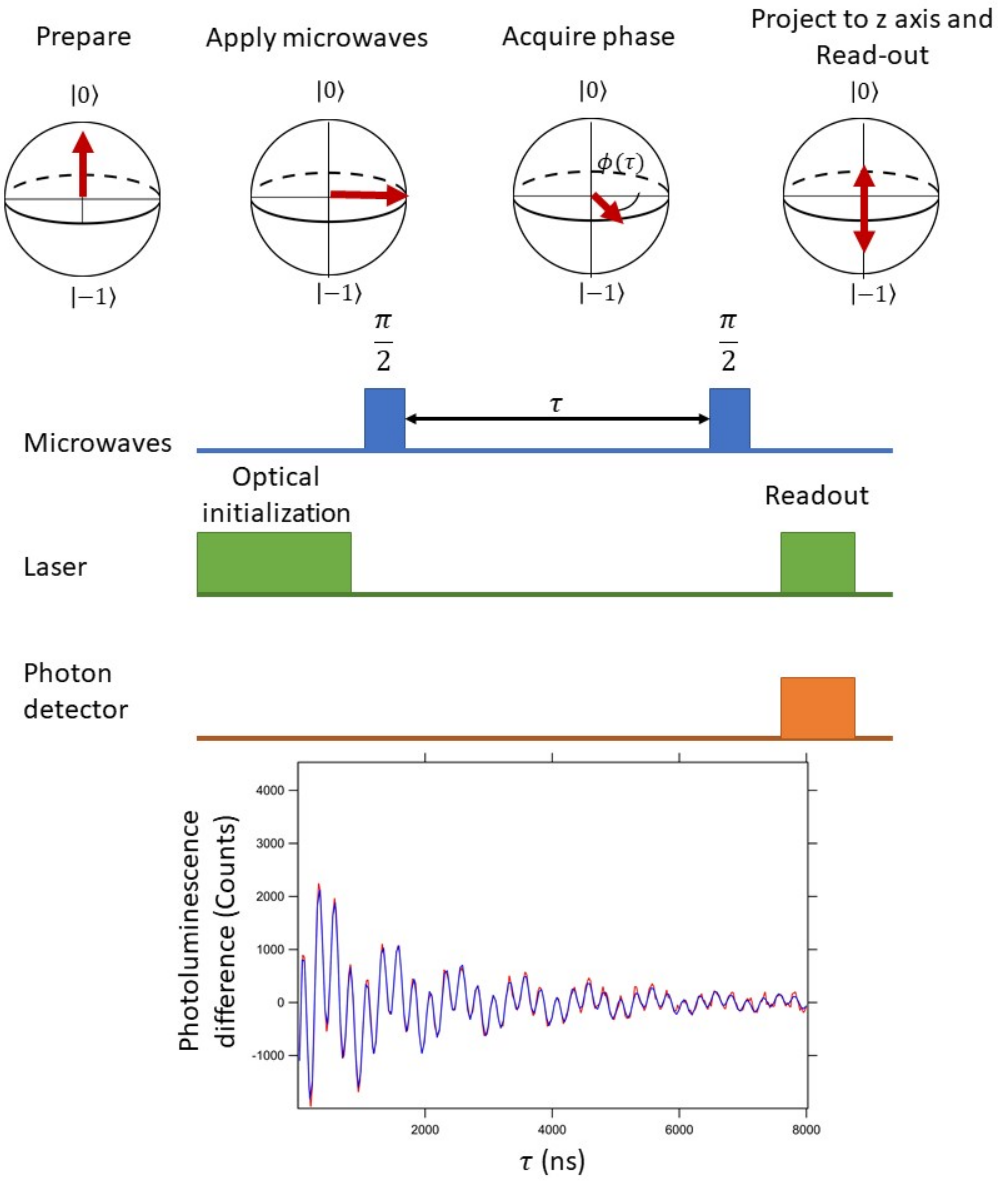

Figure 2.5: Ramsey experiment: This experiment consists of driving the spin off resonance. When the spin is in a superposition state, it will start to precess in the rotating frame. There are two spin classes being probed due to the hyperfine interaction which causes multiple beating. This phase accumulated during the time between $\pi/2$ pulses is proportional to the external magnetic field. The decay of this curve is $1.38 \pm 0.3\mu s$. The fit is in blue and the red is data.

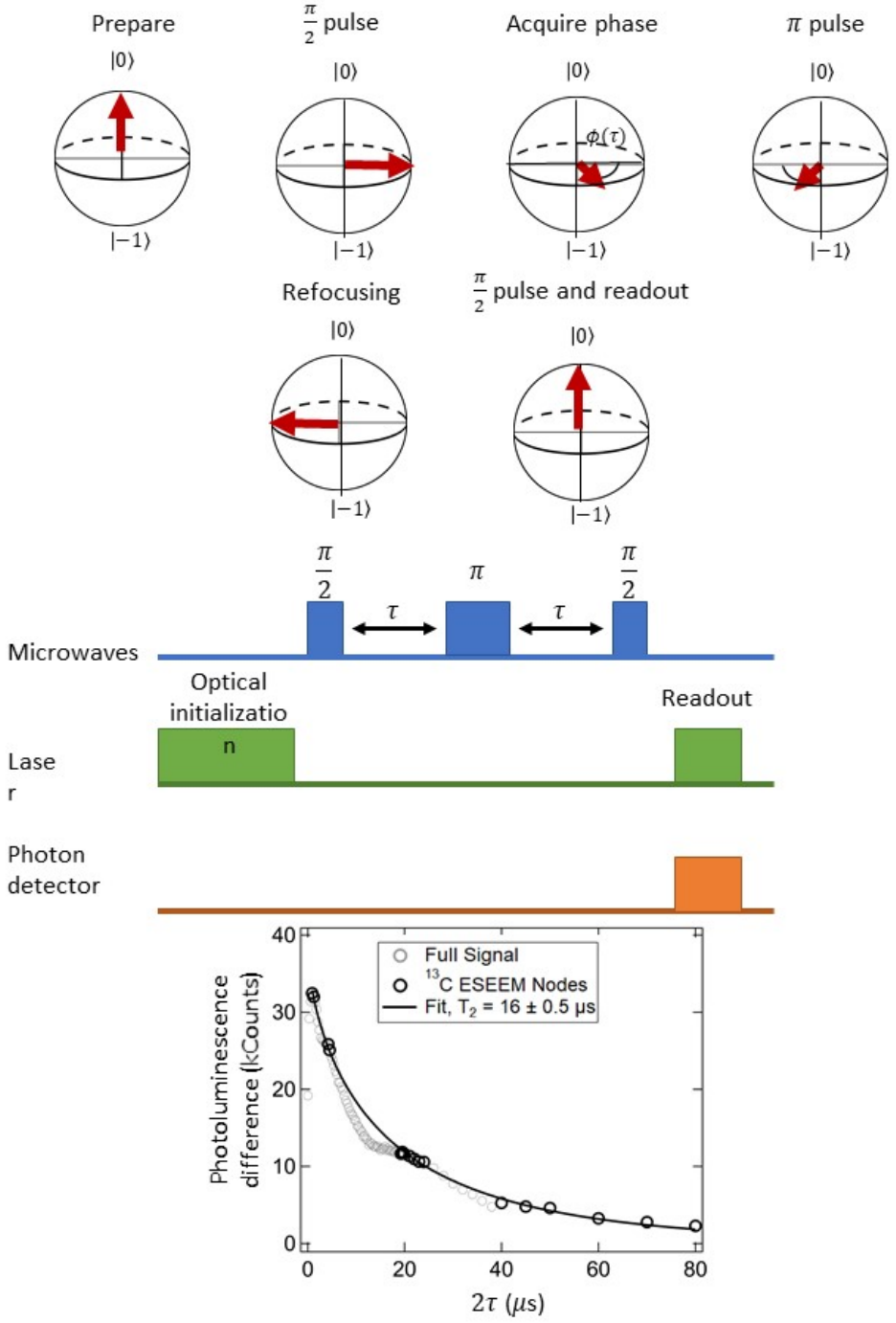

Figure 2.6: Hahn echo experiment: This spin sequence uses a central π pulse to refocus any precession that occurred after the initial $\pi/2$ pulse. This sequence decouples the spins from static magnetic fields increasing the coherence time, but removing the ability for sensing static fields.

2.4 Alternate read out schemes

I would like to note that other forms of NV center readout can be used for enhanced sensitivity for specific cases. Namely, spin to charge read out has been shown to increase the sensitivity of T_2 measurement times [103]. When the NV center is below 20 K the excited state becomes coherent and resonant excitation and readout is possible [121]. Spin to current readout has also been explored [14]. These methods are not used in this thesis. I leave references for the reader for further exploration.

2.5 Chapter Summary

From this chapter I would like to emphasize that to create a highly sensitive ensemble of NV centers it is important to both have long coherence times and large ensembles. In the next chapter I will discuss how to create an ensemble and our method which addresses these two challenges.

Chapter 3

Creation of NV ensembles in diamond

This chapter focuses on the diamond growth and NV formation techniques we used to create highly sensitive NV center ensemble sensors. I detail the process of forming diamond with ensembles of NV centers from diamond growth, vacancy incorporation, annealing, and surface treatments. The growth is done using plasma enhanced chemical vapor deposition (PECVD) with nitrogen doping growth. We introduce the vacancies of the NV centers through electron irradiation and form NVs with subsequent annealing. By tuning the electron irradiation energy and dosage it is possible to tune the density of NV centers and hence the sensitivity of the NV center ensemble. The chapter ends with a brief discussion of other future discussions for higher sensitivity ensembles.

The PECVD diamond growth with nitrogen doping techniques used at UCSB were

developed by a former graduate student in the Awschalom lab, Kenichi Ohno. His thesis details how the recipe was developed [84]. Bryan Myers, a former Jayich lab graduate student, extended Ken's work to understanding depth dependence in single NV centers [80]. This chapter is an extension of Ken and Bryan's research into the NV center ensemble regime.

3.1 Introduction to diamond growth

For single crystal diamond there are two main growth techniques: high pressure high temperature (HPHT) growth and homoepitaxial PECVD. While HPHT is capable of growing millimeter cubed volumes of diamond very quickly, the precision of a nitrogen layer placement is not possible [81, 68, 135]. Plasma enhanced deposition of diamond allows for control over growth rate from nanometers/hour [85] - 100s microns/hour [134] by tuning parameters such as microwave power, pressure, partial pressures of methane, and temperature. There are many excellent texts describing this process in detail [60]. I will briefly explain the step flow growth process and growth conditions that are tuned to optimize single crystal growth of diamond.

3.1.1 Step flow growth

Step flow growth of a crystal, sometimes called the terrace ledge kink model, is used to describe atoms which attach to a surface crystal and diffuse along the surface until finding a crystal step edge. The energy difference between the adatom on the terrace

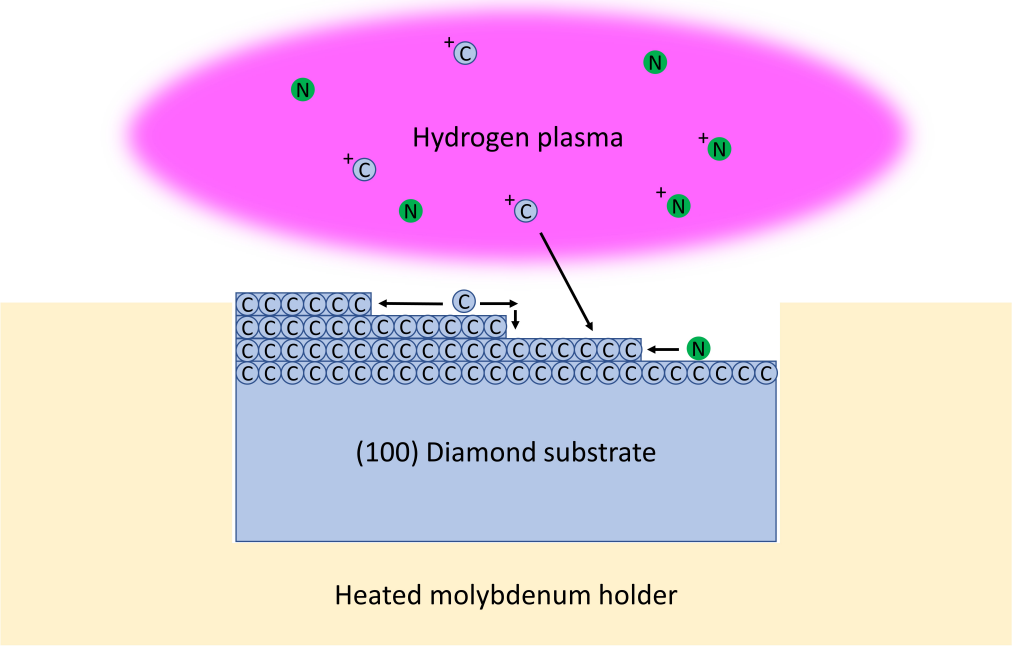

Figure 3.1: Schematic of the diamond inside the hydrogen plasma. The diamond is housed in a Molybdenum puck which is heated. The increased temperature increases the diffusivity of adatoms at the surface. The black arrows represent how ions in the plasma can adhere to the terraces of the steps and diffuse towards the step edge.

or on the step edge causes crystal growth to occur in the direction of the step edges. The core reason is that when an adatom finds a step edge it bonds with two carbon atoms rather than one, which is a more stable configuration. In the basic theory of step flow growth, the growth rate is controlled by the amount of available atoms to become adatoms, the miscut angle of the starting crystal, and the temperature. The discussion in this subsection follows the explanation from Kenichi Ohno's thesis and chapter six of Tsao's text on molecular beam epitaxy growth [84][124]. 3.1 is a schematic of the step flow growth model with diamond.

The velocity of the growth rate, v_{step} can be described as

$$v_{step} = jL \tag{3.1}$$

where j is the deposition rate of adatoms and L is the length of a step edge. During growth an adatom can be deposited anywhere on the step terrace and will diffuse on the surface with a rate

$$v_{adatom} = L/t_{Diffuse} \tag{3.2}$$

where $t_{Diffuse}$ is the time to travel the length of the step edge and is proportional to the diffusivity, D.

$$t_{diffuse} = L^2/D \tag{3.3}$$

To encourage single crystal growth and prevent aggregates of adatoms the growth rate of the step edge must be slower than the diffusivity of adatoms on the surface. $v_{step} < v_{adatom}$. This leads to the relation

$$jL^2/D < 1 \tag{3.4}$$

which must be met for single crystal growth.

The parameter j may be tuned by changing the amount of precursor gas in the chamber, in the the case of diamond growth this is increasing the methane. The parameter L can be tuned by the miscut angle. Finally, the parameter D can be tuned by the temperature.

3.1.2 Hydrogen plasma effect on growth

An added complexity to diamond growth is the effect of the hydrogen plasma in the growth chamber. The hydrogen plasma both prepares the surface and prevents aggregates of adatoms from forming through isotropic etching. At high temperatures ($> 800^\circ$ C) hydrogen will primarily etch along dimer rows while at lower temperatures ($< 500^\circ C$) the etch becomes more anisotropic [106]. By etching the diamond at $800^\circ C$ for 15 minutes step bunching caused during polishing will be removed resulting in a highly polished surface [47][84][106].

The hydrogen plasma also maintains the single crystal orientation of the diamond during growth. Once methane is introduced into the chamber and diamond growth starts, the isotropic nature of the hydrogen plasma will etch away adatom aggregates that form on the step terraces and grow in directions other than the (100) crystal orientation. The etch rate of the diamond is highly temperature dependent so it is necessary to tune the temperature system to balance the diffusivity of the adatoms with the etch rate of the plasma. It is also necessary to balance this rate with the partial pressure of methane in the chamber. If the partial pressure is too high and adatoms are added too quickly then aggregates will form. Low partial pressures $0.05 - 0.025\%[CH_4]/[H_2]$ are used during growth to maintain the single crystal surface. It is best to start with a known recipe and tune one parameter at a time until single crystal diamond growth is achieved. Please see Ken Ohno's thesis for a detailed study on how to tune these parameters [84].

3.1.3 Other growth considerations

Other considerations to take into account during growth are pressure and microwave power. Ken Ohno's thesis details the steps taken to optimize single crystal growth in the UCSB PECVD chamber [84]. The microwave power used for this thesis is 750 W. This power allows for low growth rate and control over nitrogen plasma. The pressure is 25 Torr, a parameter also optimized by Ken Ohno.

3.2 Sample preparation

Because homoepitaxial growth is highly sensitive to the starting seed, our diamond growth is limited by the quality of our starting substrate surface. The following steps are used to prepare a single crystal diamond for PECVD growth. Figure 3.2 demonstrates a flow chart for diamond preparation with AFM surface roughness scans between critical steps.

We start with an electronic grade diamond from Element Six. The standard starting size is 2x2x0.5 mm. The growth surface is the {100} orientation of the diamond. These substrates are chosen for their low impurities, < 5 ppb nitrogen and < 1 ppm boron, giving them negligible background fluorescence. As received, the Element Six samples have a surface roughness of 3 nm RMS and a miscut angle between 0 to 3°. The samples are then sent to Syntek, a diamond polishing company, for slicing and further polishing. Syntek maintains the original miscut angle while polishing the growth surface below 1 nm RMS.

Parameter	Value	Unit
Forward bias	500	W
Reverse bias	200	W
Argon flow rate	25	sccm
Chlorine flow rate	50	sccm
Pressure	0.7	Pa

Table 3.1: Parameters used while etching diamond in argon chlorine plasma. The resulting etch rate is 3 $\mu m/hr$

The polishing from both Syntek and Element six produce subsurface strain and damage which is removed through plasma etching of the surface.

Before plasma etching the diamond is cleaned with boiling sulfuric/nitric acid with a 1:1 proportion for 1 hour, followed by a NanoStrip etch at 100 C for 1 hour and sonication in acetone followed by isopropanal alcohol for 15 minutes each.

AFM scans are taken between each step which modifies the surface to ensured the surface maintained a sub nanometer polishing. If particles remain on the surface of the diamond the cleaning process is repeated and checked with an AFM topography scan until the diamond has no noticeable particles on the surface. Any particles on the surface can mask the diamond during etching resulting in a "grassy" surface.

Plasma etching is done using an inductively coupled plasma (ICP) tool. A plasma of Ar/Cl is created to etch 500 nm of diamond. Because neither Ar or Cl reacts strongly with diamond it is can be considered a gentle mechanical etch to release strain from the surface [64]. Table 3.1 gives the parameters used in our ICP etching. Forward and reverse bias are the microwave powers used to create the plasma. The flow rates give the proportion of gases in the plasma.

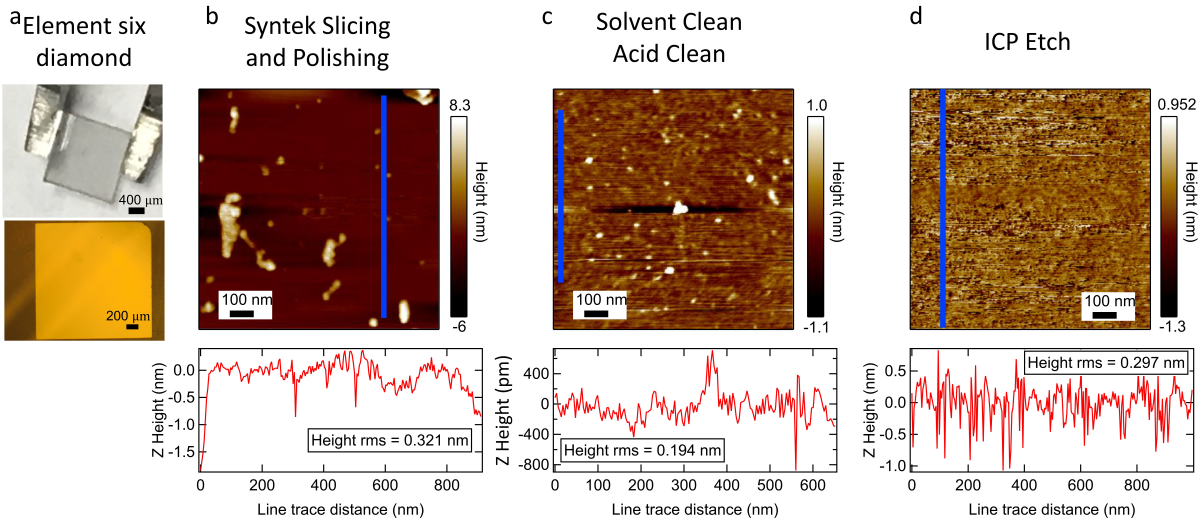

Figure 3.2: Flow chart outlining the steps taken for preparing a diamond substrate for growth.

After etching the diamond a final AFM scan is taken to ensure the surface is free from large defects and polishing was maintained during the etch. Occasionally particles are seen on the surface but are removed after an acid clean. See 3.2.

Finally, before inserting the diamond into the growth chamber the diamond is cleaned with with boiling sulfuric/nitric acid with a 1:1 proportion for 1 hour, followed by a NanoStrip etch at 100 C for 1 hour and sonication in acetone followed by isopropanal alcohol for 15 minutes each. To minimize contamination of the surface it is beneficial to do the final clean immediately before loading the sample.

This starting substrate can be used for many different growth parameters, including nitrogen δ-doped, thick nitrogen doping, and growths ranging from 10 nm to 10 μ m diamond layers.

The next section details the growth parameters used for producing a highly sensitive

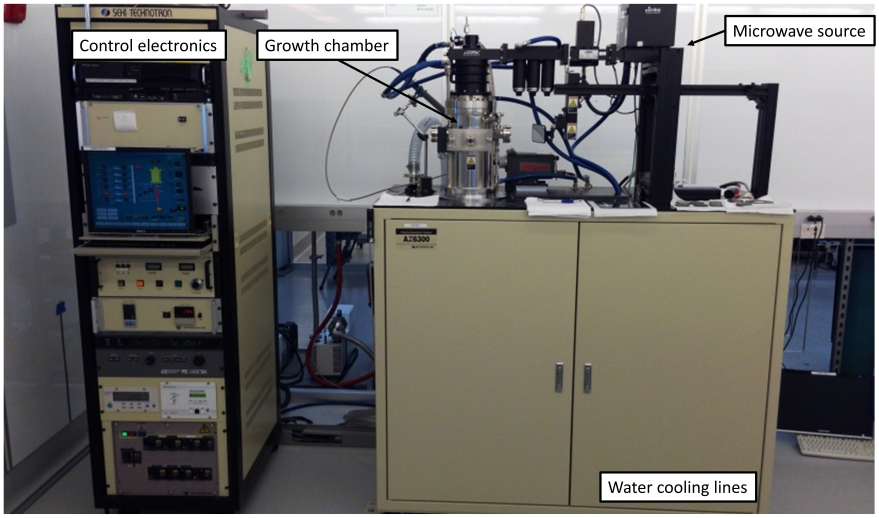

Figure 3.3: SEKI AX6300 plasma enchanced chemical vapor deposition diamond growth tool. The growth chamber and microwave source are labeled. The water cooling lines are inside the cabinet. To the left is the control electronics for the tool. This image was modified from the CNSI website [1].

diamond ensemble.

3.2.1 Growth recipe

At UCSB we use a SEKI AX6300 plasma enhanced chemical vapor deposition tool 3.3. The following steps are the backbone for diamond growth. The parameters that were tuned for optimizing an NV ensemble sensitivity are the nitrogen and methane flowrates, doping time, and isotope of nitrogen, and isotopic purity of ^{12}C used.

Upon loading the diamond into the chamber and pumping down to $< 10^{-5}$ Pa the chamber is ready for growth. The low background pressure is needed to prevent contamination in our diamond. Nitrogen 14 and carbon 13 in the air will damage the growth isotopic quality. The turbo pump used for achieving low pressures is turned off and a

roughing pump controls the pressure of the chamber for the remainder of the growth. I outline the steps of diamond growth below.

1. Starting the plasma
    (a) Set the chamber pressure to 3 torr.
    (b) Set the hydrogen flow rate to 25 sccm.
    (c) Wait for the chamber to stabilize.
    (d) Start the RF for plasma at 450 W. Tune the microwave impedance to minimize back reflection
    (e) Increase the chamber pressure to 25 torr
    (f) Increase the hydrogen flow rate to 400 sccm
    (g) Wait for the chamber to stabilize.
    (h) Set the RF for the Plasma to 750 W. Tune the microwave impedance to minimize back reflection
2. Hydrogen etching
    (a) Set the temperature to 800 C and wait for the chamber to stabilize (6 minutes)
    (b) Let the surface be etched by the hydrogen for 15 minutes. This step releases the step edges described earlier needed for growth. More details on this step can be found in the thesis of Ken Ohno [84].
3. Create a buffer layer of diamond
    (a) Start the methane flow rate at 0.1 sccm. This flowrate produces a 13 nm/min of diamond. The flow rate was checked via secondary ion mass spectroscopy,

as seen in Figure 3.5

(b) Wait for four hours, creating a 52 nm buffer layer

4. Create a nitrogen doped layer.

   (a) Increase the nitrogen flow rate to a value between 0.1 sccm - 5 sccm. The nitrogen incorporation goes linearly with the flow rate during growth. These measurements are further explored in the next chapter. Figure 3.7 shows the data taken to confirm this claim.

   (b) Wait for nitrogen incorporation to be incorporated into a desired layer thickness. For example, 15 minutes is enough time for δ doping of nitrogen while 38.5 hours creates a 500 nm layer with minimal surface defects.

5. Create a 50 nm cap layer of diamond. This cap prevents the NV ensemble from being limited by the surface while being close enough to not limit sensitivity.

   (a) Wait for 3.8 hours to create a 50 nm cap of diamond.

6. End the growth by turning of the methane, microwaves, heater, pressure, and hydrogen in that order.

To optimize this growth recipe for ensembles, the flow rates of the methane and nitrogen were explored as well as the thickness of the layers.

3.3 Characterizing growth

To understand the quality of the growth a range of techniques were used. To measure growth rate, isotopic purity, and whether nitrogen incorporation occured, secondary ion mass spectroscopy was used. To measure the density of nitrogen incorporated, double electron-electron resonance techniques were used. DEER will be further explored in the following chapters. NV center ODMR as described in chapter 1 was used to measure the NV spin properties.

3.3.1 Surface defects

Dislocations in the diamond lattice can cause aggregates of adatoms to accumulate. The longer a growth occurs the more aggregates of adatoms can grow. 3.4 shows the different quality of surfaces than can be achieved during growth. C020 was grown for only 60 nm and shows minimal surface damage. A zoom in of a hillock formed during growth is shown. C031 was a 600 nm growth on a 20 μm sample. Due to the fragile nature of 20 μm thick starting substrates it is difficult to clean teh substrates. I suspect that poor cleaning prior to growth of C031 was the cause of large surface defects formed during long growth. C041 was 150 μm thick starting substrate which went through careful surface cleaning minimizing large surface defects. The growth direction did result in a wave like structure on the surface, which is optically visible. Although proper cleaning can minimize surface defects differences in starting substrates from element six can result in different growth qualities.

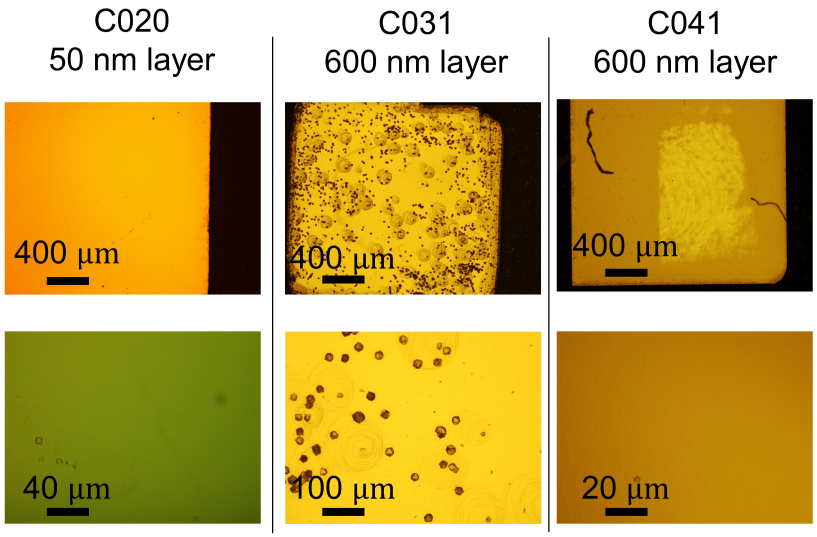

Figure 3.4: Three samples with different overgrowth layers are shown.

3.3.2 Secondary ion mass spectroscopy

Secondary ion mass spectroscopy is a way to determine the elemental composition of a material as a function of depth. Using a Physical Electronics 6650 Dynamic Secondary Ion Mass Spectrometer at the Materials Research Laboratory we are able to detect elemental changes with a depth resolution down to 3 nm and concentration detection levels down to ppb. A cesium ion beam is used to produce negative ions from elements in the diamond. The ions are then sent through a magnet which sorts the ions by their mass. 3.5 shows the results of that data for two samples, C038 and C039. By measuring the depth when the isotopic purity of carbon changes and knowing the growth time, we are able to calibrate our growth rate for different methane partial pressures.

In sample C039, I used a methane flow rate of 0.1 sccm and was grown for 6 hours and 50 min and achieved a layer of 91 nm. From this data we extract a growth rate of

13 nm/min. SIMS also gives us the confinement of our δ-doped nitrogen layer. In C039, which had a flow rate 5 sccm ^{15}N and was doped for 15 min, the cyanide ion peak had a Gaussian profile with σ of 5 nm. The large $^{12}C^{15}N$ signal at the beginning comes from substances on the surface being removed from the ion beam.

In sample C038, I used a methane flow rate 0.2 sccm and grew for 7 hours and achieved a layer of 127 nm. From this data we extract a growth rate of 18 nm/min. Nitrogen incorporation with a flow rate of 0.1 sccm ^{15}N for 30 minutes did not show a signal above the noise of the spectrometer. Also, NV characterization did not show ^{15}NV. I suspect that nitrogen incorporation did not occur in this sample.

Understanding the limits of nitrogen incorporation with different flow rates of methane and nitrogen during growth is a parameter which can be further explored.

In Figure 3.6 we analyze the isotopic purity using different flow rates. We see with higher flow rates of methane the isotopic purity improves. We are unsure why the isotopic purity of the diamond changes. One suspicion is carbon monoxide, CO, on the walls of the chamber are not efficiently pumped out and contribute to the ^{13}C background. Growing more quickly would incorporate less CO from the walls.

3.3.3 Flowrate versus P1 density

The level of nitrogen in the chamber is low enough that increasing the partial pressure of nitrogen will increase the density of nitrogen in the diamond. Nitrogen incorporated into the diamond is called a P1 center. Figure 3.7 shows the control we have over the P1

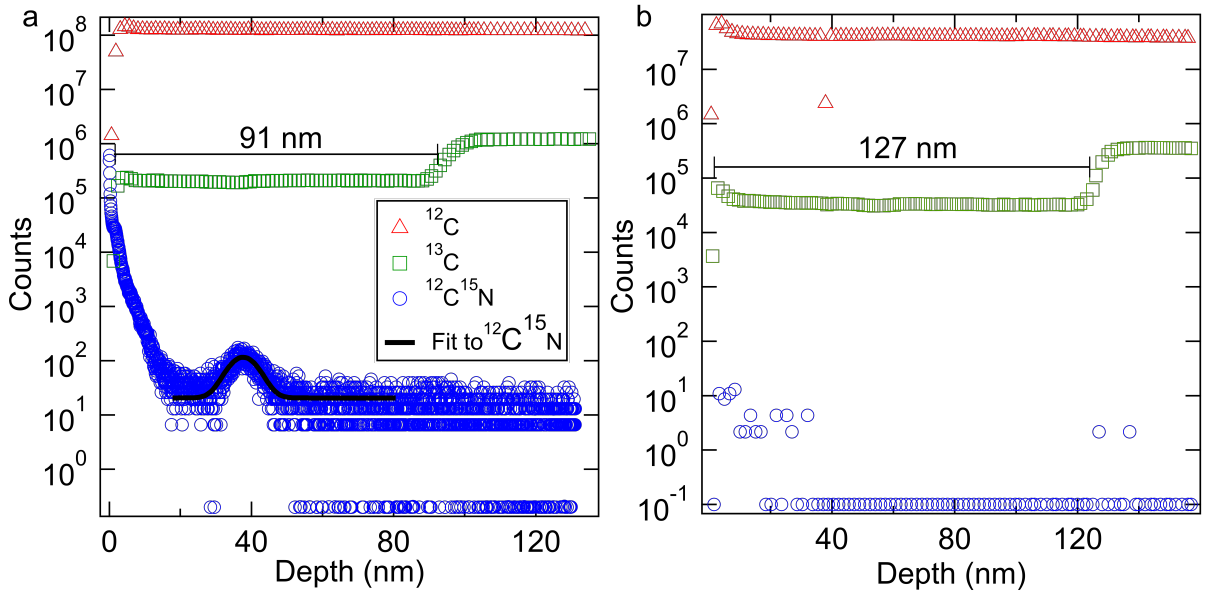

Figure 3.5: Data taken with secondary ion mass spectroscopy (SIMS). Counts of ions of ^{12}C and ^{13}C isotopes and cyanide isotope $^{12}C^{15}N$ versus the depth of the SIMS measurement. Fig. a is data taken from sample C039. This sample was growth with a flow rate of 0.1 sccm ^{12}C methane for 6 hrs and 50 min. We extract a growth rate of 13 nm/min. Nitrogen was incorporated with a flow rate of 5 sccm ^{15}N. The Gaussian fit to the nitrogen peak shows a delta doping with a σ of 5 nm. Fig. b is a data taken on sample C038 which was grown with a flow rate of 0.2 sccm ^{12}C methane for 7 hours. We extract a growth rate of 18 nm/min with these parameters.

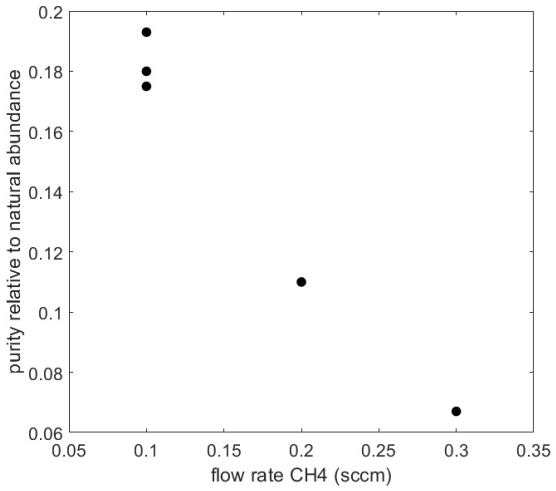

Figure 3.6: The isotopic purity of diamond using 99.99% ^{12}C carbon. We see with larger flow rates of methane the final diamond has better isotopic purity

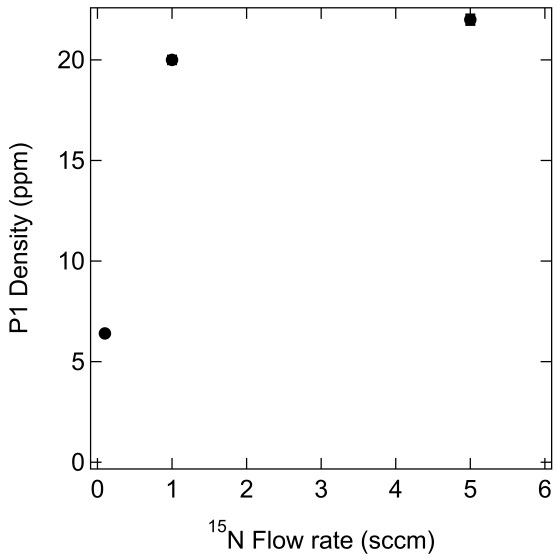

Figure 3.7: Nitrogen flow rate versus P1 density. Density measurements were performed using DEER as described in chapter 6

density. Chapter 6 describes how we are able to measure the P1 density in our grown diamond using double electron-electron resonance (DEER) techniques.

3.4 Future directions

Thin film diamond growth with nanometer precision of impurities is still a relatively nascent field with many directions to explore. One trait mentioned earlier in the chapter is we do not understand why increasing methane flow rate improves the isotopic purity of the diamond. When growing for 24 hours at 0.3 sccm ^{12}C and 50 sccm N_2 with all other growth rates the same as stated in the chapter, the growth rate dropped to 10 nm/hr and nitrogen incorporation was in the 50 ppb level. It is unclear why increasing those parameters, which nominally should increase growth rate and nitrogen incorporation gave

dramatically different results. Finally, exploring how the miscut angle and phase effects diamond growth quality is a parameter which has not been explored much in our lab.

Chapter 4

Vacancy formation in diamond

Large sections of this chapter are adapted with permission from C.A. McLellan *et al* Nano Letters 2016, 16, 4, 2450-2454. Copyright (2016) American Chemical Society.

After diamond growth there is minimal lattice damage, which means there are minimal vacancies which can migrate the the nitrogen to form an NV center. It is necessary to introduce vacancies into the diamond lattice via an second step. This chapter describes the electron irradiation techniques explored during my graduate work. Much of this chapter can be found in the reference [76]. The method of using low energy electrons produces highly coherent NV centers useful for ensemble magnetometry. By having deterministic process we can perform dose tests on a single diamond substrate allowing us to optimize our magnetometer quickly.

Research groups have explored a variety of patterning methods to place NV centers deterministically. However, many of these methods result in severely compromised NV

spin coherence times and/or require post microfabrication processes. For instance, Toyli et al. demonstrated lateral control of NVs by ion implanting through nanofabricated apertures [123],but the resulting coherence times were relatively short ($< 20\,\mu$s). Focused nitrogen-ion [53, 67, 77] and helium-ion [52] implantation can also localize NV centers but the resulting coherence times are either short, $< 1\mu$s, or not reported. Electron irradiation from a transmission electron microscope was used to form NVs in type-1B diamond with broad spin resonance line widths indicating short coherence times[56]. Long NV coherence times (700μs) were demonstrated in nitrogen -doped diamond via carbon implantation through apertures [86]. However, we have not seen as high of an P1 conversion to NV center conversion efficiency compared to electron irradiation. With these challenges in mind, we explored low energy electron irradiation of diamond ($<$ 200 keV electrons) to create NV centers.

4.1 TEM irradiation

Vacancies were introduced locally into the diamond via focused electrons from an FEI Technai G2 Sphera transmission electron microscope (TEM) at room temperature 4.1. The TEM provides in situ tuning of the energy, current, and areal dose of the electron irradiation. We investigated energies ranging from 120 to 200 keV, doses ranging from 10^{14} to 10^{22} e/cm^2, and spot sizes ranging from 0.0220 μm.

By using a $\delta-$doped diamond sample, we could test the quality of this process without being P1 spin-bath limited. Figure 4.2 shows that for a $\delta-$doped sample we can obtain

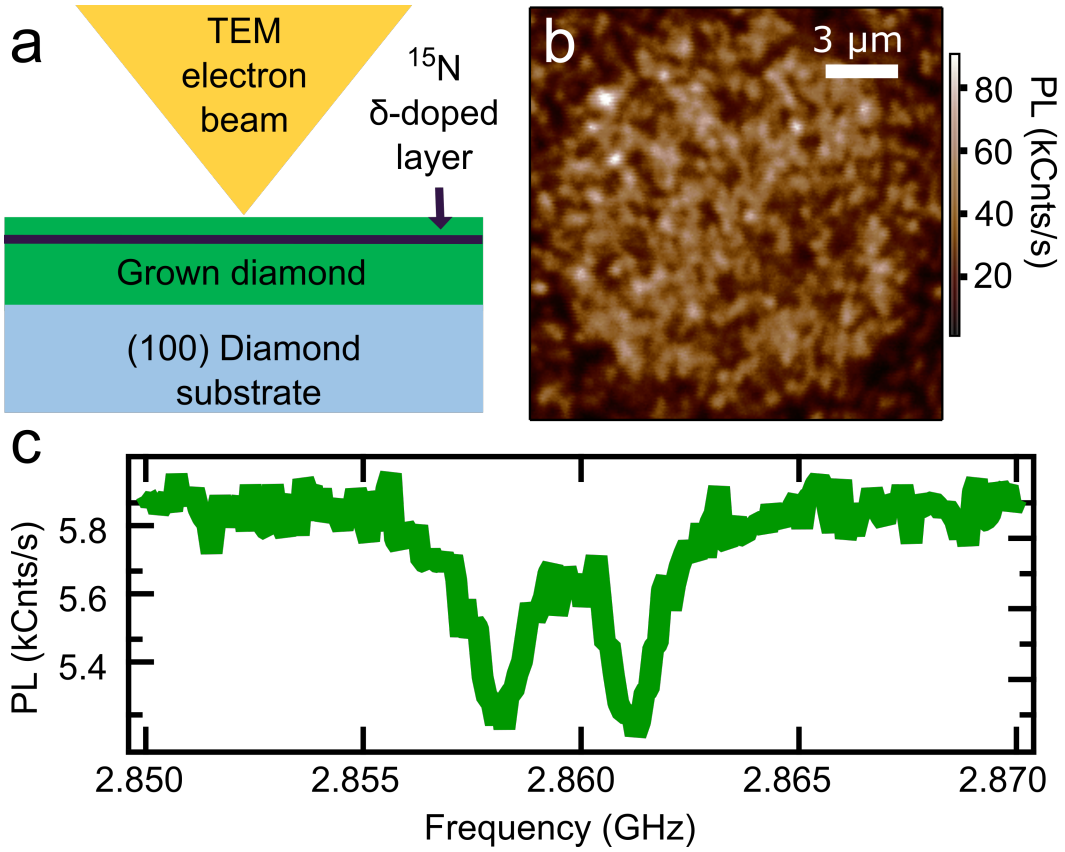

Figure 4.1: a. A schematic of the TEM irradiation method used b. confocal photoluminesence image showing the area of diamond irradiated creates NV centers. c. optically detected magnetic resonance spectrum showing the ^{15}N hyperfine signature
. Figure adapted with permission from C.A. McLellan *et al* Nano Letters 2016, 16, 4, 2450-2454. Copyright (2016) American Chemical Society. [76]

consistently long coherence times ($> 100\mu$s) and multiple NV spin-echo coherence times greater than 1 ms.

This technique can be expanded for ensemble magnetometers by increasing the thickness of the nitrogen doped layer and increasing the size of the electron beam. Critical to improving the sensitivity of an ensemble magnetometer is increasing the NV center density. We can tune the density by tuning the electron irradiation dosage. In Figure 4.3, a δ-doped layer is electron irradiated and the change in NV density from 10^{14} to 10^{18} e/cm^2 is shown.

For large of ensembles of NV centers, we can also tune the density of NV centers. In Figure 4.4 the change in density is shown for different electron irradiation. The density between samples and spot sizes consistently increases with electron irradiation. Because this data was taken on a wide-field microscope, we suspect the smaller spots (500 nm and 1μm) have artificially low densities because the background is overwhelming the measurement. I am showing the data for completeness.

The data for this section was analyzed using the spin counting techniques described in Chapter 6.

4.2 Minimizing lattice damage

To maximize coherence of the NV center ensembles one wants minimize excess damage to the lattice. Another challenge of over damaging the lattice is the background fluorescence from the diamond can increase. To understand the depth extent to which NVs are

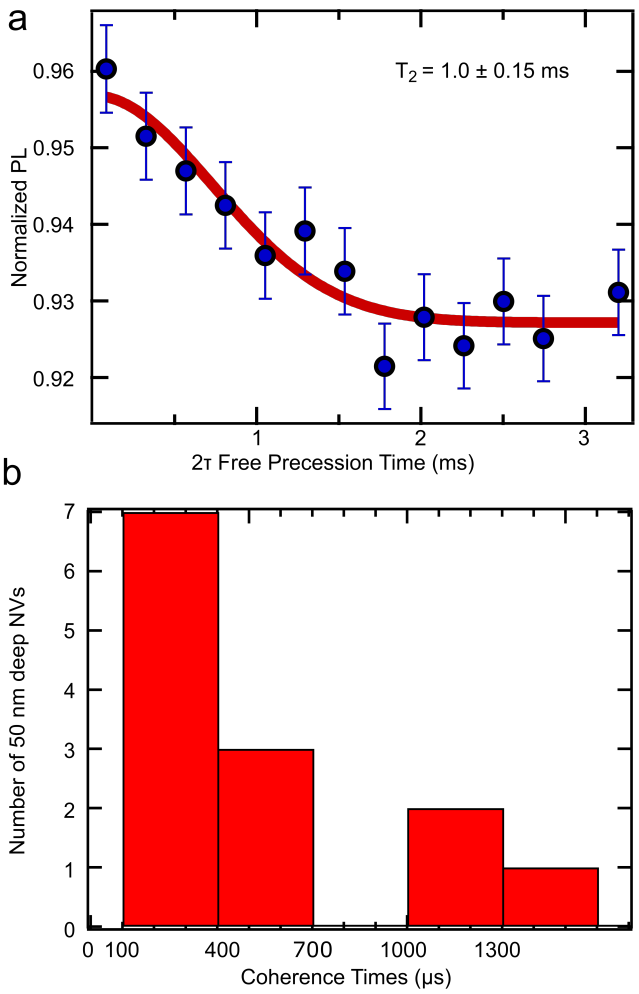

Figure 4.2: a. A characteristic Hahn echo coherence measurement. The NV center measured had a coherence time of 1 ms b. A histogram of coherence times measured showing all NVs had coherence times longer than 100 μs

. Figure adapted with permission from C.A. McLellan *et al* Nano Letters 2016, 16, 4, 2450-2454. Copyright (2016) American Chemical Society. [76]

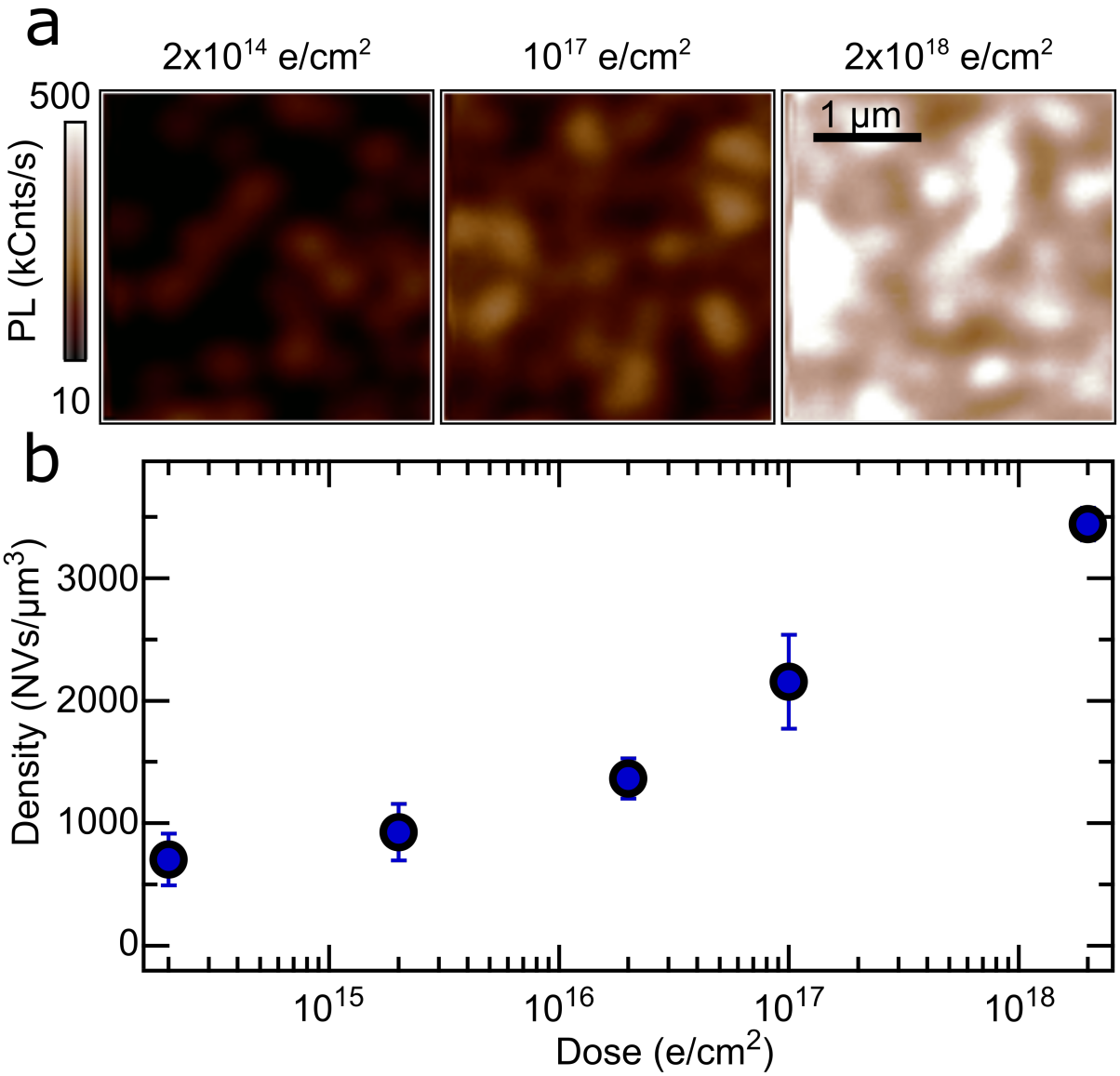

Figure 4.3: a. Confocal photoluminesence images showing that increasing the electron irradiation dosage increases the number of NVs as seen by the increasing photluminesence. b. The change of density of NV centers versus electron irradiation dose. The error bars are from the measuring the density in multiple 5x5 μm spots. This sample was a δ-doped sample with 0.1 sccm ^{15}N used during growth. The sample's name is C020. Figure adapted with permission from C.A. McLellan *et al* Nano Letters 2016, 16, 4, 2450-2454. Copyright (2016) American Chemical Society. [76]

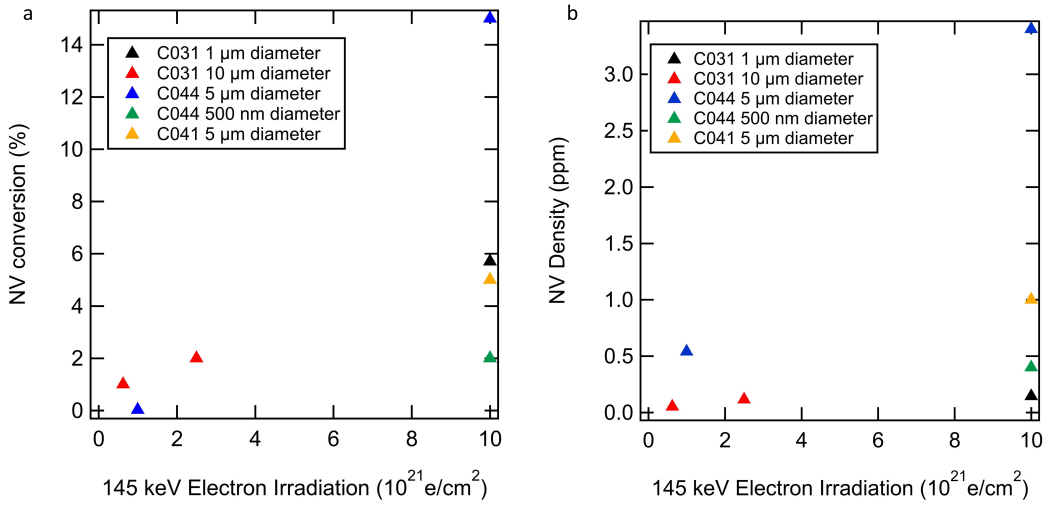

Figure 4.4: NV ensemble formation with electrons: a) shows the conversion efficiency in percent NVs to total nitrogen incorporation b) shows the same set of data but the total NV density in ppm. Different sample have different nitrogen incorporation. C031 is 6 ppm, C041 is 20 ppm and C044 is 22 ppm.

formed in the diamond and understand how to mimizize damage we looked at the depth of NV centers formed with different electron energies. To quantitatively map out this dependence, the formation of ^{14}NV in the bulk diamond is used as a marker. The depth of an NV was determined by the microscope's focus height with aberrations accounted for in a wave-optics model [122]. Optical diffraction and spherical aberrations also limit the measurement precision as the focal plane extends deeper into the diamond. Although the vacancies diffuse during annealing, previous diffusion studies suggest that under our annealing parameters, vacancies only migrate hundreds of nanometers [28, 73], a value smaller than the uncertainty in our optical depth measurement. Figure 4.5 plots the depth of the deepest observed NV, where NVs were formed in a layer that extends from the surface down to this measured depth. A linear fit to the NV depth versus irradiation energy data yields the minimum threshold energy (ET) required to form an NV center right at the surface, ET = 145 $\pm$ 16 keV. The slope of the linear fit is 1.05 $\pm$ 0.04 μm/keV, that is, increasing the electron energy by 1 keV results in the formation of NVs 1 μm deeper in the diamond.

Using CASINO V2, a Monte Carlo simulator of electron trajectories in solids [34], we simulated the maximum travel depth of electrons before their energies fall below ET = 145 keV. The results of the simulation are shown as a green line in Figure 4. Though ET has been fit from the data, the slope of the green line (1.05 $\pm$ 0.01 μm/keV) is not an adjustable parameter. The good agreement between data and simulation indicates that NV creation is a good marker for vacancy formation. Using a collision model from

Campbell et al. we calculate the displacement energy Ed for a carbon to be removed from the diamond lattice to be 30 ± 4 eV, which is in good agreement with previous studies [13, 17, 25, 59].

We have also seen evidence that increasing the energy of the electron irradiation creates more g=2 spins and increases the amount of ^{0}NV, neutral NV centers, in our diamond. Both of these two contributions lowers the sensitivity of our magnetometer.

With these findings we have seen that operating at 145 keV electron irradiation dosages produces the best sensitivity.

Figure 4.6 demonstrates how increasing the dosage of our electron irradiation produces a more sensitive magnetometer. We are currently exploring how to build an electron gun which can produce more than 10^{23} e/cm^2 in a reasonably sized area ($>$ 1mm^2). With a TEM irradiation with 10 nA of current this experiment would take 500 years but using an electron gun with 1 mA of current that time drops down to a few days.

4.3 TEM irradiation for deterministic placement

An attractive feature of TEM irradiation is its facile ability to laterally localize NV centers in a point-and-shoot fashion. This ability is especially useful for placing NV centers deterministically into nano-structures. Although this capability is not the highlight of this thesis, I wanted to briefly mention our progress with deterministic placement. To demonstrate this capability, we focused a 200 keV electron beam down to a 20560 nm diameter spot size and irradiated an array of 12 spots spaced 3 μm apart, as schematically

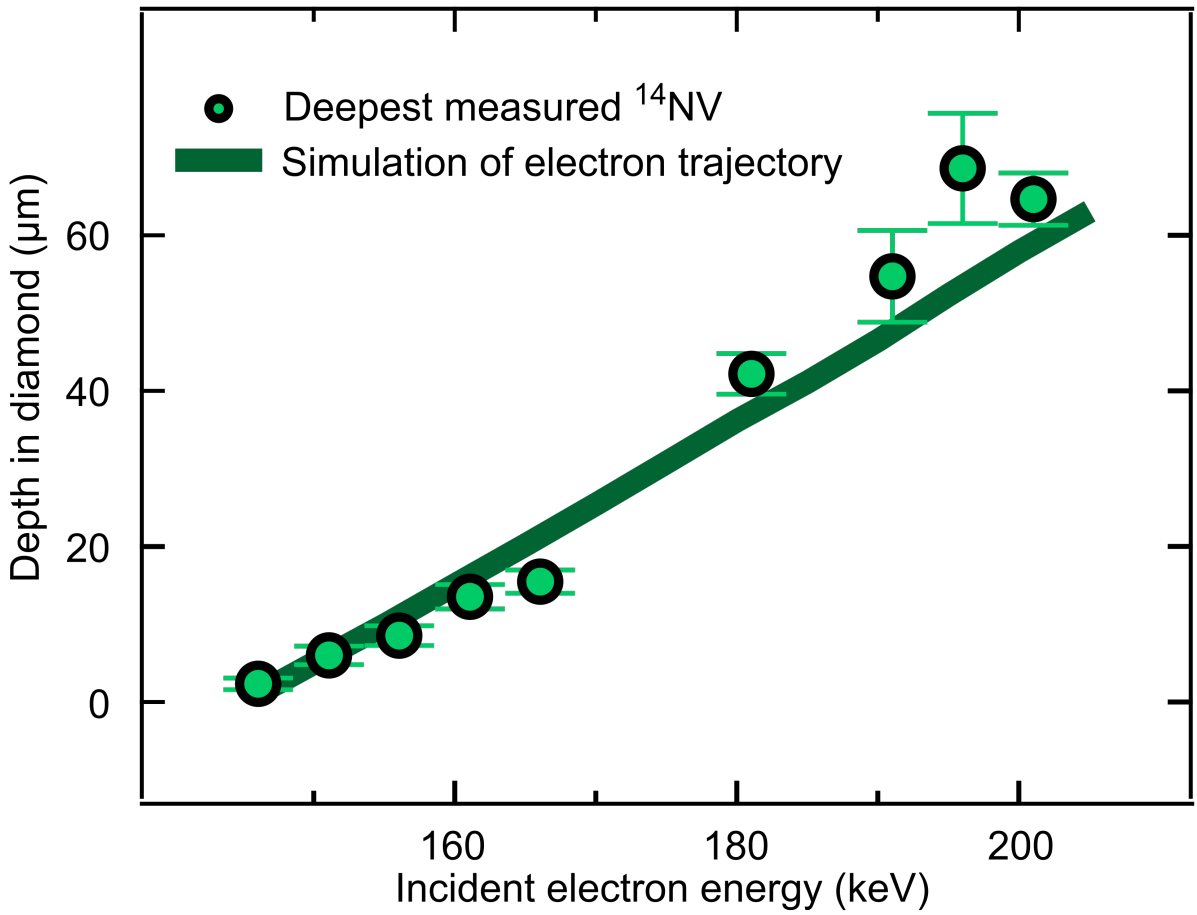

Figure 4.5: By tuning the electron irradiation energy it is possible to tune the depth of vacancy formation. This plots shows the depth of NV formation in the bulk of the diamond with different energy levels. The simulations are done using CASINO to simulate the electron distance in diamond. We use the threshold energy calculated from the x-axis intercept. The displacement energy of a carbon matches previous measurements. Figure adapted with permission from C.A. McLellan *et al* Nano Letters 2016, 16, 4, 2450-2454. Copyright (2016) American Chemical Society. [76]

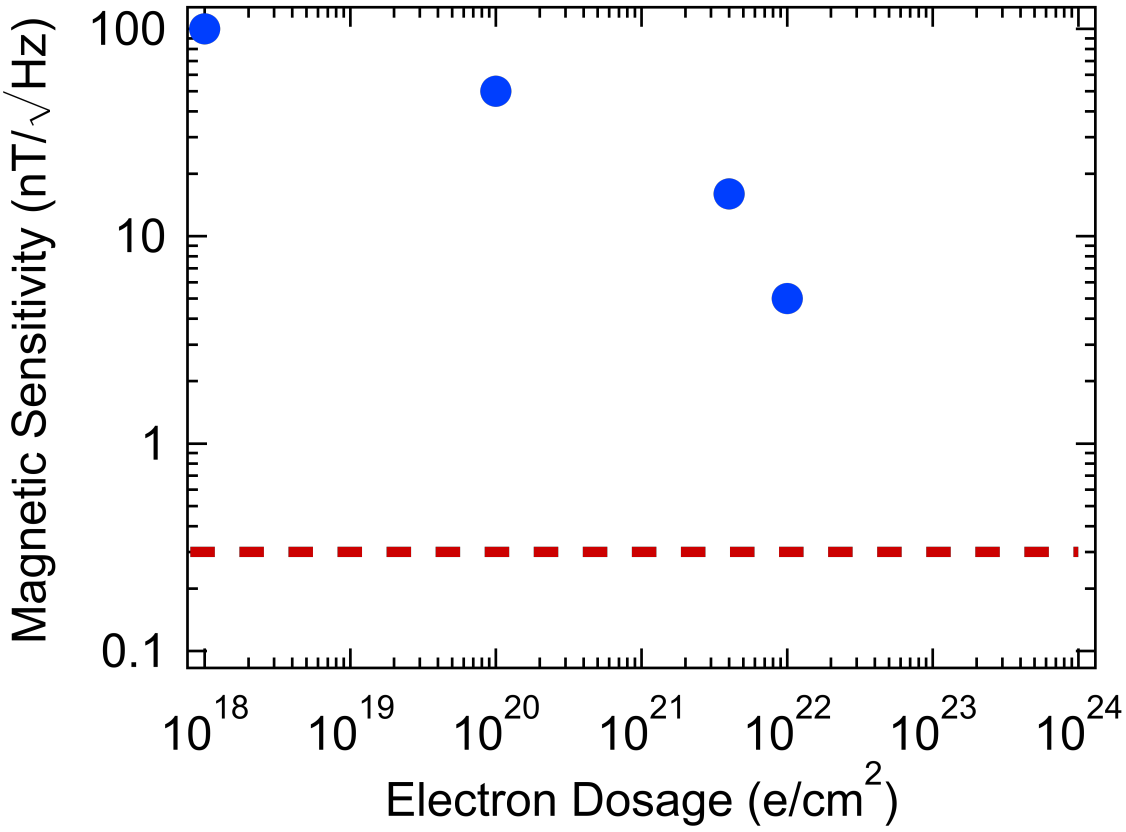

Figure 4.6: Electron irradiation vs sensitivity: This plot shows the magnetometer sensitivity for a 5x5x0.5 mm^3 sensing volume. The sample has roughly 6 ppm density of P1 centers. As the electron irradiation increases more P1 centers are converted to NV centers increasing the sensitivity of the magnetometer.

shown in Figure 4.7. Figure 4.7 also shows a confocal PL scan of the irradiated area after subsequent annealing. The irradiation pattern is faithfully replicated by NV center PL, where each irradiated spot contains one to several NV centers, as confirmed through ODMR measurements. For the 20 nm irradiated spots, optical diffraction limits our ability to claim NV localization to better than 450 nm, the full width half-maximum of the PL spots. We note that width of the PL profiles from the 20 nm spots are the same as those from single NV centers, indicating it is likely that the NV centers are localized to a much smaller area. A highly desirable future prospect is to use the TEM's imaging capabilities to locate a prepatterned feature, such as a diamond nanopillar or photonic crystal cavity, and locally irradiate to form an NV in the desired location. The likelihood of forming a high-quality NV in a nanofabricated device is high because TEM irradiation creates a high density of NVs with long coherence times. To deterministically engineer NV centers approaching a lateral accuracy of 10 nm, an increased nitrogen concentration may be needed which may in turn decrease the NV coherence times. Future measurements will explore this high-density regime.

4.4 Annealing Parameters and surface treatment

To form the NV centers after irradiation samples were annealed and the surface was oxygen terminated. For δ-doped samples, annealing occured at 850 c in H_2/Ar (5%/95%) forming gas for 2 hours. The sample was then boiled for 1 hour in a 1:1:1 mixture of nitric: sulfuric: perchloric acids. The Nitric acid is 70% concentration. The sulfuric acid

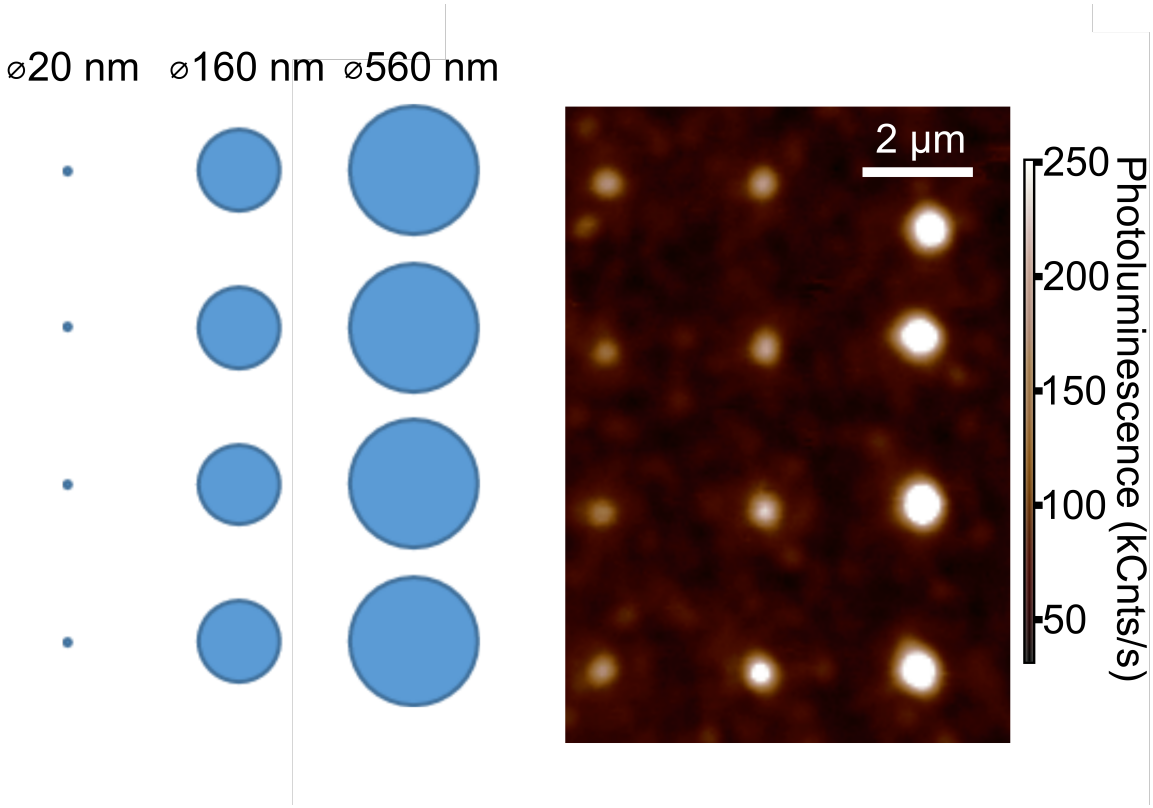

Figure 4.7: Focused TEM irradiation:Lateral position control of NV formation. Photoluminescence image showing NV centers formed in an array of TEM irradiation spots of diameters 20, 160, and 560 nm and electron doses of 1.6 × 1022, 2.5 × 1020, 2 × 1019 e/cm2 respectively. The pattern made with the TEM is shown on the left. Figure adapted with permission from C.A. McLellan *et al* Nano Letters 2016, 16, 4, 2450-2454. Copyright (2016) American Chemical Society. [76]

is 99% concentration. The perchloric is 70% concentration. We boil the mixture at 200 c. Finally, the sample is oxygen annealed in high purity oxygen for 2 hrs at 450 c.

For 500 nm nitrogen doped layers the process is very similar except the annealing in forming gas at 850 is done for 48 hours. The oxygen annealing is done for 4 hours.

For samples with substrates 20 μm the tri-boiling acid step is skipped because the samples are easily lost.

4.5 Future work

To create highly coherent NV centers it is important to minimize damage. We also want to minimize NV centers formed in the bulk diamond. We are working towards exploring annealing while irradiating at 145 keV to achieve these goals. We are also working on exploring how to place NV centers deterministically inside nano-structures using the TEM. By using a cathode luminescence holder we are hoping to in-situ determine if an NV center was formed.

Chapter 5

Magnetometer equipment

During the course of my doctoral studies, I helped design and build two optical set-ups. The first is a confocal microscope used to characterize NV centers. The second was built with Tim Eichhorn and consisted of a wide field microscope used to probe ensembles of NV centers. The wide field set-up could be used as a characterization set-up and a magnetometer. This chapter describes the design of each set-up. I end by describing some simple magnetometry experiments done on the wide-field magnetometer.

5.1 Confocal Microscopy

The data taken in Chapters 2 and 3 was done using a confocal microscope. The basic design used was described in previous theses [80, 87, 66]. The benefits of a confocal are its high spatial resolution, which is limited by the numerical aperture (NA) of the objective and wavelength of light being used for excitation. Confocal microscopes block out a lot of

the ambient light just by design because only the focused light is sent through a pinhole. This type of microscope is ideal for single NV centers which are not very bright (80 kCnts/s).

5.2 Wide field magnetometer

The homebuilt wide-field magnetometer used in our set-up was designed to be used with neurons. The main design feature was having an enclosure for the liquid in which the neurons were housed. There are four main components of our wide field magnetometer: laser, excitation and collection optics, camera, and spectrometer. The laser is a homebuilt system consisting of a current driver controlling a laser diode mounted in a thermoelectric cooling device. The excitation optics can be operated in normal excitation or total internal reflection fluorescence (TIRF) mode. The camera used for most of our measurements was an electron multiplier charge coupled device (EMCCD) and an avalanche photodiode (APD) was used for pulsed measurements. We are working towards using a camera for pulsed measurements. I briefly express our progress to that end. Finally, we can redirect our excitation light through a spectrometer to better probe our camera.

5.2.1 Laser box

The widefield magnetometer uses a homebuilt laser box. It consists of a laser diode being controlled by a current source and housed in a thermo-electric cooling device. This style

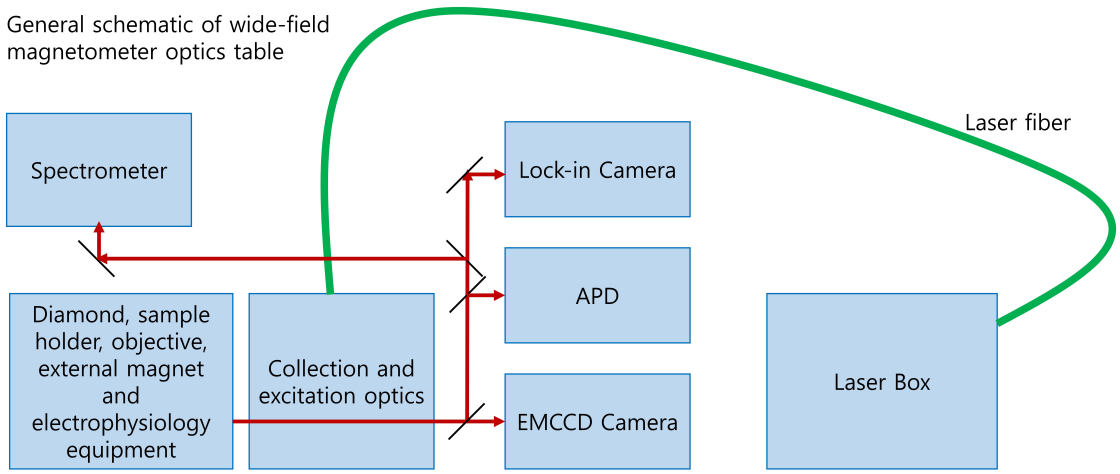

Figure 5.1: General schematic of wide-field magnetometer optical table. Photo and schematic credit to Jungbae Yoon.

of laser allows us to choose the excitation length by changing the laser diode being used. We can also tune the laser power by tuning the current flowing through the diode. For a typical 520 nm laser diode with power up to 120 mW, we can expect up to 10 mW on the diamond. This laser can be used for low power excitation in the wide field. The flexibility in wavelength and power has made this a very useful design for characterization of the widefield magnetometer. Figure 5.2 shows the schematic and an image of our laser. After the photodiode we have optics for shaping the beam before sending it through the acoustic optic modulator (AOM). The AOM is used to pulse the laser. The laser is then fiber coupled and brought to the experiment.

The parts list for the laser box is found in table 5.1.

Because we decided to use a current driver and diode mount from different companies

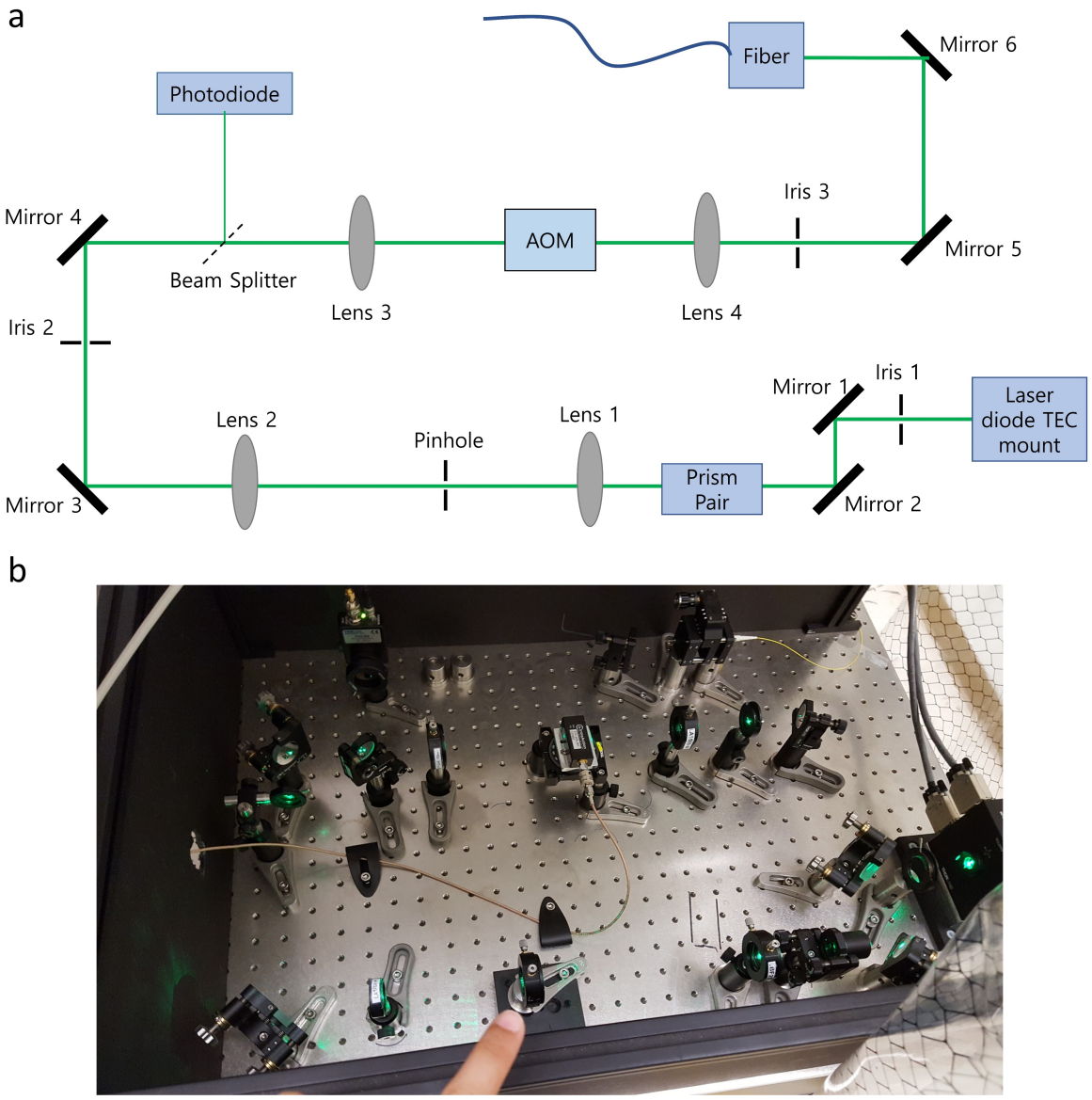

Figure 5.2: Homebuilt laser box

Part	Description	Purpose	Vendor	Part Number
Prism Pair	3x Mag.	Correct laser spot size	Thorlabs	PS879-A
L1	f = 200 mm	Confocal Pair 1	Thorlabs	LBF254-200-A
L2	f = 100 mm	Confocal Pair 2	Thorlabs	LA1509-A
L3	f = 150 mm	Focus beam into AOM	Thorlabs	LA1433-A
L4	f = 100 mm	Collimate beam after AOM	Thorlabs	LA1509-A
Beam Splitter	1 - 10% beam pick-off	Monitor power of laser	Thorlabs	BSF10-A
Pinhole	50 μm	clean-up laser spot	Thorlabs	P50H
AOM	Tellurium oxide	Pulse laser	Intraaction	ATM-200.3C1
Photodiode	Si Switchable Gain Detector	Track laser power	Thorlabs	PDA36A

Table 5.1: Laser optics box parts

TEC Mount	Diode mount	Hold diode and cool	Thorlabs	TCLDM9
Current Control	500mA - Laser Diode Controller	Control current of diode and TEC	Arroyo	6305 ComboSource
Asphere lens	8 mm focal length	Collimating laser	Thorlabs	C240TME-A
Diode	520 nm 120 mW diode G pin code	Thorlabs	L520P120	

Table 5.2: Laser control box

we needed to make our own cables. The main idea when making these cables is to make sure the current is being sent through the diode in the correct direction. Because the laser diode we used did not have a built in photodiode for feedback we use a ThorLabs photo-diode to feedback to the current source and maintain constant power. In Tables 5.3 and 5.4, I detail how to connect pins correctly for the photodiode, TEC mount and current source used in our experiments. The data for the pin labels are found in the manuals for Thorlabs TCLMD9 [119] and Arroyo 6305 combo source [54].

When both LD and PD are anode grouded,LD is connected to pin 2 of the Thorlabs TEC and PD is connected to pin 7 of the Thorlabs TEC. Pin 2 is then connected to the laser anode of the Arroyo controller. Pin 7 is connected to the laser cathode of the Arroyo controller. Figure 5.3 shows how the pins of the laser diode are connected to the TEC pins. At the end of the day one wants to make sure the current is flowing through the laser diode in the correct direction. If the laser is noisy, floating the system sometimes

Thorlabs Pin Number	Description	Arroyo Pin Number	Description
1	TEC Lockout (+)	N/A	N/A
2	+Thermister	7	Sensor (+)
3	-Thermister	8	Sensor (−)
4	+TEC	1,2, or 9	TE (+)
5	-TEC	3,4, or 10	TE(−)
6	NA	NA	NA
7	AD 592 (−)	N/A	NA
8	NA	NA	NA
9	AD 592(+)	NA	NA

Table 5.3: TEC control cables

Thorlabs Pin Number	Description	Arroyo Pin Number	Description
1	Interlock	1	Interlock +
2	Photodiode cathode	9	Laser anode
3	Laser ground (case)	8	Laser Anode Voltage Sense
4	Photodiode cathode	3	Earth ground
5	Interlock return	2	Interlock -
6	Laser diode voltage (cathode)	NA	NA
7	Laser diode cathode	5	Laser cathode
8	Laser diode anode	NA	NA
9	Laser diode voltage (anode)	NA	NA

Table 5.4: Laser control cables: Table which explains which pins to connect for combining a Arroyo Instruments 6305 with a Thorlabs TCLD9

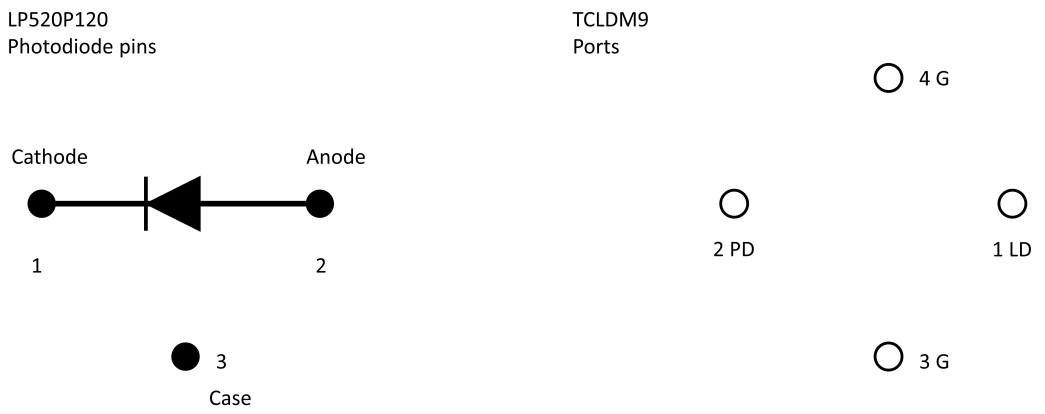

Figure 5.3: Laser diode pins and TEC pin holders: How to connect pins of laser diode to pins of Thorlabs TEC mount

helps.

5.2.2 Excitation and collection optics

Figure 5.4 shows the excitation and collection paths for the wide-field magnetometer. The lenses are used to adjust the beamsize and focus on the back focal plane of the objective. It is necessary to have a polarizing beamsplitter and two half wave plates to optimize the polarization on the NV centers. The NV center fluorescence is maximized when the electric field of the excitation light is polarized parallel to the NV center.

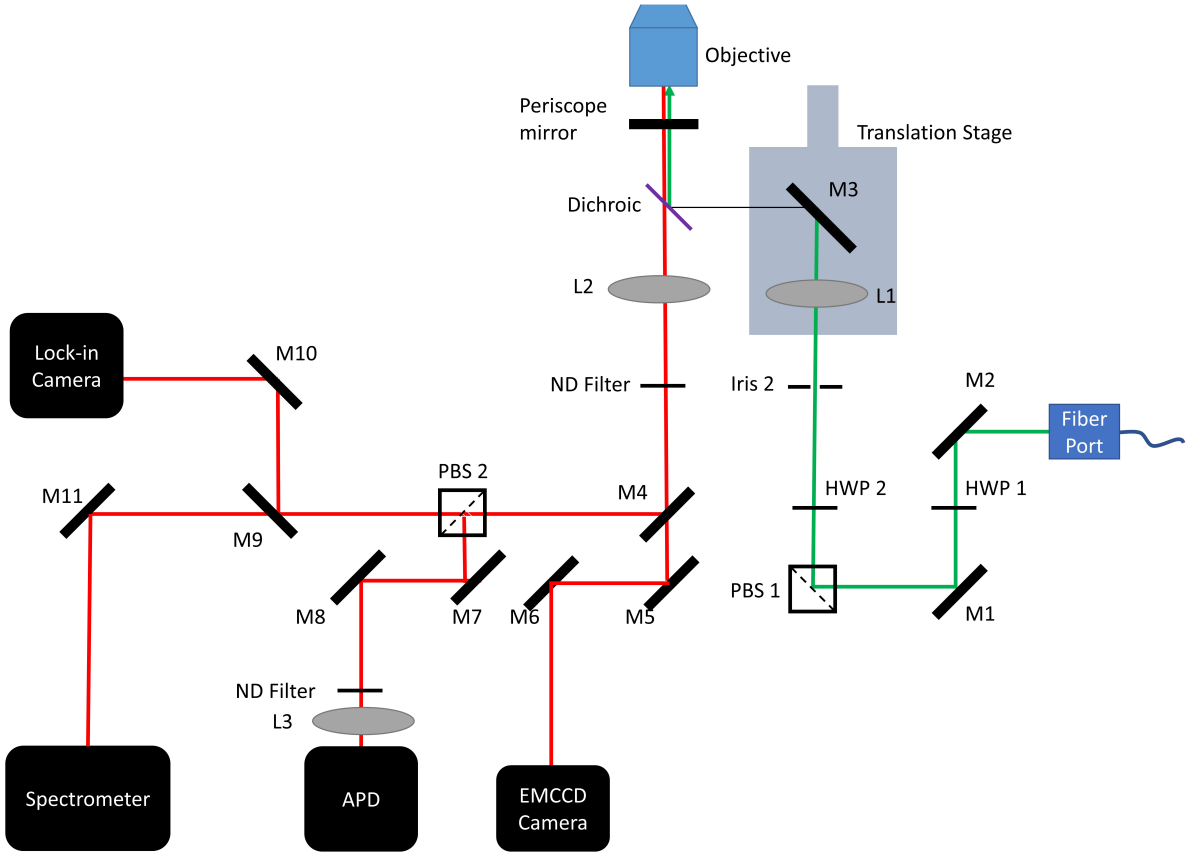

Figure 5.4: Wide field magnetometer optics. Schematic credit to Jungbae Yoon.

Lenses	Description	Purpose	Vendor	Part Number
Objective	NA = 1.49, Mag = 60x, oil	TIRF excitation	Olympus	APON 60XOTIRF
Fiber port	f = 4 mm	Asphere to collimate laser 1	Thorlabs	C610TME-A
L1	f = 40 mm	Confocal Pair 1	Thorlabs	LA1422-A
L2	f = 400 mm	Confocal Pair 2	Thorlabs	LA1172-A
L3	f = 500 mm	Focusing Lens	Thorlabs	LA1908-A
L4	f = 500 mm	Imaging Lens	Thorlabs	LA1908-B
Lenses	Description	Purpose	Vendor	Part Number
Dichroic	560 nm dichroic	Separate green laser from red signal	Semrock	FF560-FDi01-25x36
Long Pass	594 nm long pass filter	Remove non-red photons	Semrock	BLP01-594R-25

Table 5.5: TIRF Lenses

Lenses	Description	Purpose	Vendor	Part Number
M1-4	Silver	Guide beam and image	Thorlabs	PF10-03-P01
DC	560 nm dichroic	Separate green laser from red signal	Semrock	FF560-FDi01-25x36
LP	594 nm long pass filter	Remove non-red photons	Semrock	BLP01-594R-25

Table 5.6: TIRF Mirrors and Filters

5.2.3 Sample Holder

The sample holder was designed to maintain ambient conditions for biological samples, particularly neurons. Neurons, even from cold-blooded animals, put stringent requirements on the sample holder. In chapter 7 the details of the neuron experiment are described. When designing the sample holder we needed to have the neuron encased in an aqueous solution. Every thing had to be non-toxic. Non-toxicity limited which glues and metals we could use. We could also not use optical oil with neurons. The RF waveguide needed to be isolated from the aqueous solution, because the ions in the solution created a loss source in the waveguide. The waveguides needed to produce homogenous microwave fields across the viewing area. Finally, everything had to be small enough to fit the magnet, top-down optics, and electro-physiology equipment.

The design we came up with is shown in figure 5.5

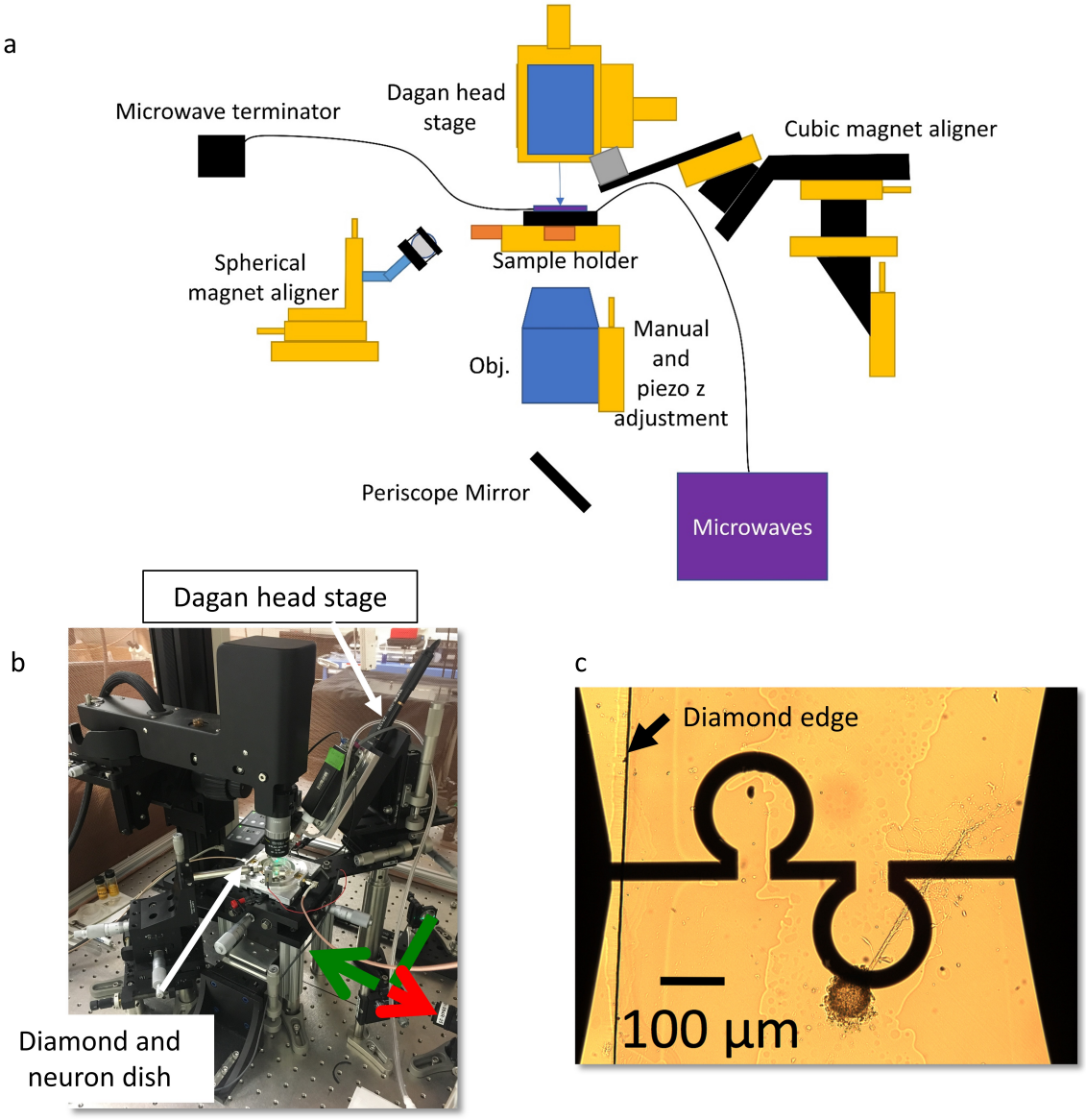

Figure 5.5: Diagram and images of the sample holder. a) The schematic demonstrates how we align our magnetic fields, electrophysiology equipment and optics. b) a large image of the wide-field magnetometer showing the neurophysiology in the background. c) a zoom in of the diamond and omega waveguides. There is a live Aplysia Californica neuron on top of the diamond.

Ω waveguides design and recipe

The omega waveguide was designed by Bryan Myers for earlier experiments in the Jayich lab. We modified it by adding a silicon dioxide layer on top of the gold. I recommend using PECVD to create a homogenous silicon dioxide layer. Do the PECVD SiO_2 layer in two steps to prevent pin-holes from forming.

The recipe for making the omega waveguides is below. Figure 5.5 shows the final omega waveguides in part c.

1. Start with 75x25x0.140 mm^3 glass coverslips
2. Solvent clean the coverslips by sonicating in acetone followed by IPA for 5 min each and dry with nitrogen
3. Bake at 80 C for 5 minutes to make sure all solvent has evaporated
4. spin HMDS at 4000 kRPM for 30 seconds
5. Bake at 115 C for 60 seconds
6. Spin AZ5214-IR at 400 kRPM for 30 seconds
7. Bake at 95 C for 60 seconds
8. Use contact lithography tool SUSS MJB-3 at 7.5 mW/cm^2 of power
    (a) Expose for 5 seconds
9. Post-exposure bake at 110 C for 60 seconds

10. Flood exposure at 7.5 mW/cm^2 for 60 seconds

11. Develop 45 seconds in AZ300MIF

12. Rise in DI water for 3 minutes

13. Deposit 10 nm Ti, 400 nm Au, and 10 nm Pt using electron beam evaporation (E-beam 3 in UCSB nanofabrication facility)

14. Lift off using acetone and follow with an IPA clean

15. Deposit 100 nm of SiO2 using PECVD 2

    (a) Do this step in two 50 nm steps to prevent pin holes forming in the SiO2 layer

5.2.4 Electro-physiology

A Dagan 3900A integrating patch clamp was used for the electrophysiology experiments. These experiments are explained in more detail in chapter 7. This equipment lets us detect the small electrical currents and voltage changes produced by neurons whey they fire signals called action potentials. At its core the patch clamp is a very sensitive amplifier.

5.2.5 Cameras and photodiodes

There were three main photon collection sources used for our experiments: an emccd camera, an APD, and a lock-in camera.

Electron Multiplier Charge Coupled Device Cameras

Electron multiplier charge coupled device (EMCCD) cameras have excellent quantum efficiencies. We use an Andor iXon 897. This camera is capable of detecting single NV centers. The dynamic range of these cameras is the larges of the three detection methods. With a quantum efficiency above 90% and pixel fill factors of 100% it is possible to detect down to single NV centers up to millions of NV centers.

The challenge of this camera is the slow readout. With a pixel readout speed of 10MHz, it is possible to expose for short times. The frames per second of the camera ranges from 30 - 10000 depending on how many rows are being read. A 10x10 pixel frame will take about 1 ms for readout.

This time range makes this camera ideal for continuous wave electron spin resonance. In a single sweep ESR signals can be detected. Magnetometry of static magnetic signals is shown at the end of this chapter.

5.2.6 Avalanche photo-diode

To overcome the speed limitations of the EMCCD camera and characterize our samples using pulsed sequences, we focused the entire fluorescence of our sample onto an avalanche photodiode (APD). Because APDs can only handle up to about 1 million photons per second, we needed to put optical density filters in front of our APD. Our NV center ensembles produce GCnts/s of signal. All pulse sequence data in this thesis was done using an APD. We used an Excelitas SPCM - AQRH-14.

Lock-in Cameras

We have recently started exploring using a Heliotis camera to detect the NV center under pulsed mode operation. This camera is considered a lock-in camera because it can quickly store electron charges at 240 kHz into four different bins: I^+, I^-, Q^+, and Q^-. Because the time collected on the 4 bins can be different, we can use the I bins to store the useful data and photons collected during initialization are collected on the Q bins as trash. The downside of this camera is the dark counts and collection efficiency compared to the EMCCD are worse. Only about 20% of our photons which reach the camera are collected compared to nearly 100% for the EMCCD camera. The quantum efficiency of the two cameras are roughly the same.

5.2.7 Spectrometer

The spectrometer used in our experiments is a Princeton Instruments SpectraPro 2300i. The detection was done using a fiber coupled APD.

5.3 Microwave control

Coherent manipulation of the NV center ensembles were done using microwaves sourced from Stanford Research Instruments signal generators. A diagram of our microwaves is found in figure 5.6

The equipment used is found in table 5.7

The IQ Box is a essentially a switch that changes between positive and negative 0.5

Purpose	Vendor	Part Number
Microwave sources	Stanford Research Systems	SG384/123
TTL Signals for pulse sequence	SpinCore	PulseBlasterESR-PRO
Microwave Switches	Minicircuits	ZASWA-2-50DR+
Microwave Amplifier 10 - 1000 MHz	Mini-Circuits	ZHL-20W-13+
Microwave Amplifier 1800 - 4000 MHz	Mini-Circuits	ZHL-16W-43-S+
Low Power Microwave Combiner	Mini-Circuits	ZFRSC-42-S+
High Power Microwave Combiner	MECA	802-2-3.250WWP

Table 5.7: Microwave equipment

V quickly. This voltage allows us to control the phase of the microwaves between +x, -x, +y, and -y. At its core is an Analog Devices ADG734 Quad SPDT Switch.

5.4 Simple magnetometry experiment

This section describes a simple magnetometry experiment using the wide-field magnetometer. We fabricated microwires on the diamond, wire bonded to them and sent a current. The diamond was able to detect the magnetic field from the current.

5.4.1 Current through microwires

The microwires were fabricated on diamond using the following recipe

1. Start with a clean diamond, which has been acid cleaned and solvent cleaned. Dry on a hotplate for 5 min at 80C to make sure all solvents have evaporated.

2. Stick the diamond to $\approx 1"x1"$ silicon wafer

   (a) Clean silicon wafer with acetone and IPA

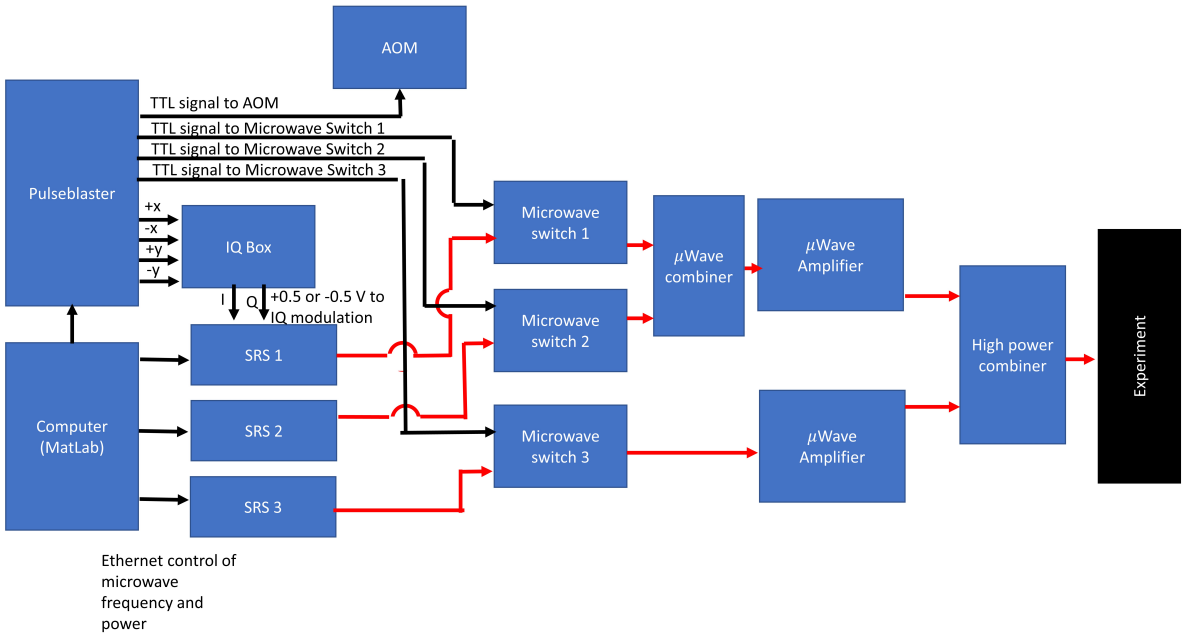

Figure 5.6: Schematic of microwave electronics. Black lines represent control signals while the red lines show the path of the microwaves.

(b) Bake wafer at 80C for 5 min to make sure all solvent has evaporated

(c) Spin PMMA A8 950 for 10 s at 3000 kRPM

(d) Immediately place diamond on the wafer

(e) Back at 180C for 2 min

3. spin HMDS at 4000 kRPM for 30 seconds

4. Bake at 115 C for 60 seconds

5. Spin AZP-4110 at 400 kRPM for 30 seconds

6. Bake at 95 C for 60 seconds

7. Use contact lithography tool SUSS MJB-3 at 7.5 mW/cm^2 of power

   (a) Expose for 40s or just before over exposure occurs

8. Develop in AZ400K 1:4 for 90 seconds

9. Descum for 30s in 300/100 Oxygen plasma (useful for better sticking of the wires but not necessary and may be skipped for shallow NV centers)

10. Deposit 10 nm Ti and 400 nm Au using electron beam evaporation (E-beam 3 in UCSB nanofabrication facility)

11. Lift off in Acetone

12. Follow with a clean in IPA

Figure 5.7 shows the shift in the cw-ESR peaks when current was flowing through the wire compared to no current.

By looking at different pixels of the image it is possible to map the magnetic field of this system.

5.5 Chapter conclusion

This chapter demonstrated how we designed our set-up to detect magnetic fields. In the next two chapters I will describe how to use this set-up to detect and quantitatively measure the magnetic spin bath inside the diamond and our progress towards using this set-up for bio-imaging.

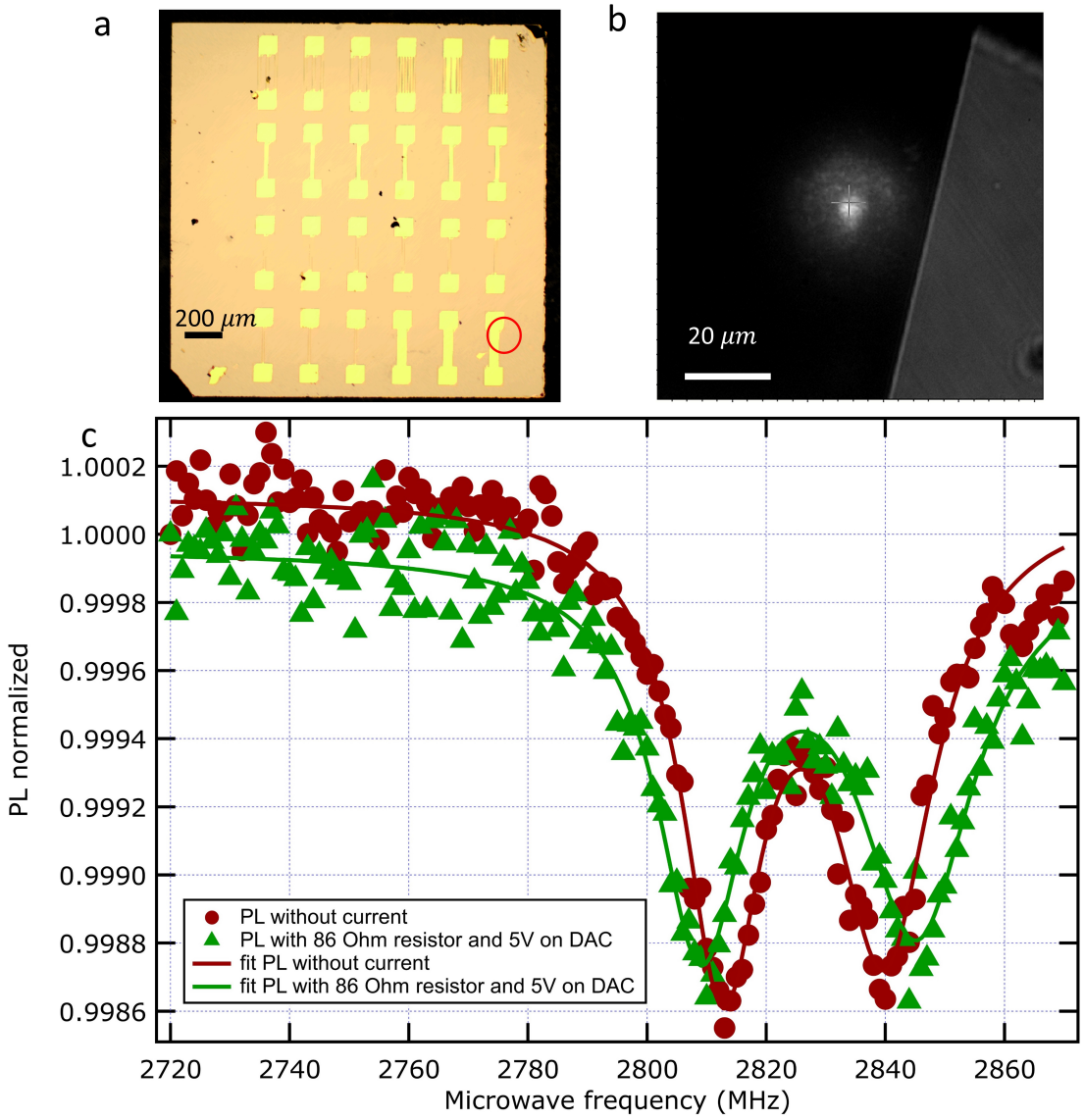

Figure 5.7: Magnetic field detection of current through a wire. a) Image of diamond membrane with microwires fabricated on the surface close to NV center ensemble. The red circle shows what is being imaged to the right b) Magnetometer image showing the NV centers being excited and the edge of a 50 μm wide wire. c) CW-ESR spectrum of the NV centers with an external magnetic field applied. The red shows the spectrum without current and the green shows the signal with current.

Chapter 6

Counting spins in the diamond crystal

Accurately counting paramagnetic spins is a challenging problem. Using traditional EPR tools one needs at least 10^{12} spins or 10^{8} spins with state of the art [35]. The spins we would like to count in our ensembles range from 10^{5} to 10^{7} total spin number. Most paramagnetic electron spins and nuclear spin baths cannot be detected optically. To detect these spins we employed double electron-electron resonance (DEER) techniques and used the NV center ensemble to detect its spin bath. It is important to understand the spin bath of the NV centers because the spin bath is the dominant source of decoherence.

The dominant spin bath in our samples are P1 centers, nitrogen in the diamond lattice. To better understand P1 centers' effect on NV centers we need to be able to measure their density and coherence properties.

NV center ensembles are also difficult to quantify once the NV centers can no longer be individually counted. Although the NV centers are fluorescence, fluorescence intensity measurements are not an accurate measurement scheme. I discuss using DEER and instantaneous spectral diffusion on NV centers to quantify the density of the $^-$NV centers in our diamonds.

The goal of this chapter is to present the data taking methods and analysis used to extract the data presented in Figures 3.7, 4.4, and 4.3.

The theory of this chapter relies on previous work towards understanding how different paramagnetic spin baths interact with one another and specifically how an NV center ensemble interacts with a P1 center bath. In particular, I use theory from Dobrovitski *et al* [31], Stepanov and Takahashi [108], and Romanelli and Kevan [96] to extract the interaction strength between paramagnetic spins in the diamond and extract densities.

6.1 P1 spin bath

Nitrogen not converted to an NV center in the diamond lattice is called a P1 center. The P1 center Hamiltonian is that of a spin 1/2 system with a hyperfine interaction with the nitrogen nuclear spin [114, 69].

$$H_{P1} = g\mu_B \boldsymbol{BS} + \boldsymbol{SAI} + \mu_N \boldsymbol{BI} \tag{6.1}$$

A is the hyperfine structure matrix. For the nitrogen - 15 isotope the perpendicular

components of A are 113.83 MHz and the parallel is 158.73 MHz.

$$\boldsymbol{A}_{^{15}\boldsymbol{N}} = \begin{bmatrix} -113.83 & 0 & 0 \\ 0 & -113.83 & 0 \\ 0 & 0 & -159.73 \end{bmatrix} \tag{6.2}$$

For the ^{14}nitrogen isotope the perpendicular components of A are 81.312 MHz and the parallel is -114.032 MHz.

$$\boldsymbol{A}_{^{14}\boldsymbol{N}} = \begin{bmatrix} 81.312 & 0 & 0 \\ 0 & 81.312 & 0 \\ 0 & 0 & -114.032 \end{bmatrix} \tag{6.3}$$

The quadrupole term for the ^{14}N P1 centers is small, $P_{\|} = -3.9$ MHz and is ignored in our calculations. The spin interaction values come from reference [27].

Using the MatLab package EasySpin it is possible to simulate where the P1 center will have transition frequencies [110]. In figure 6.1 the P1 center transitions are shown for an external magnetic field aligned along the $\langle 111 \rangle$ direction of the diamond and the RF fields perpendicular to the $\langle 111 \rangle$ direction. The parameters for ^{15}N were used. The external magnetic field strength is 20.02 mT and the linewidth is 1 MHz. The central two peaks are stronger because they consist of the 3 misaligned P1 center orientations. The weaker outer lines are from the $\langle 111 \rangle$ aligned P1 centers.

6.2 Interaction Hamiltonian

In order to use spin coherence measurements to quantitatively extract densities of a spin bath it is necessary to understand how spins couple to one another. Much of this

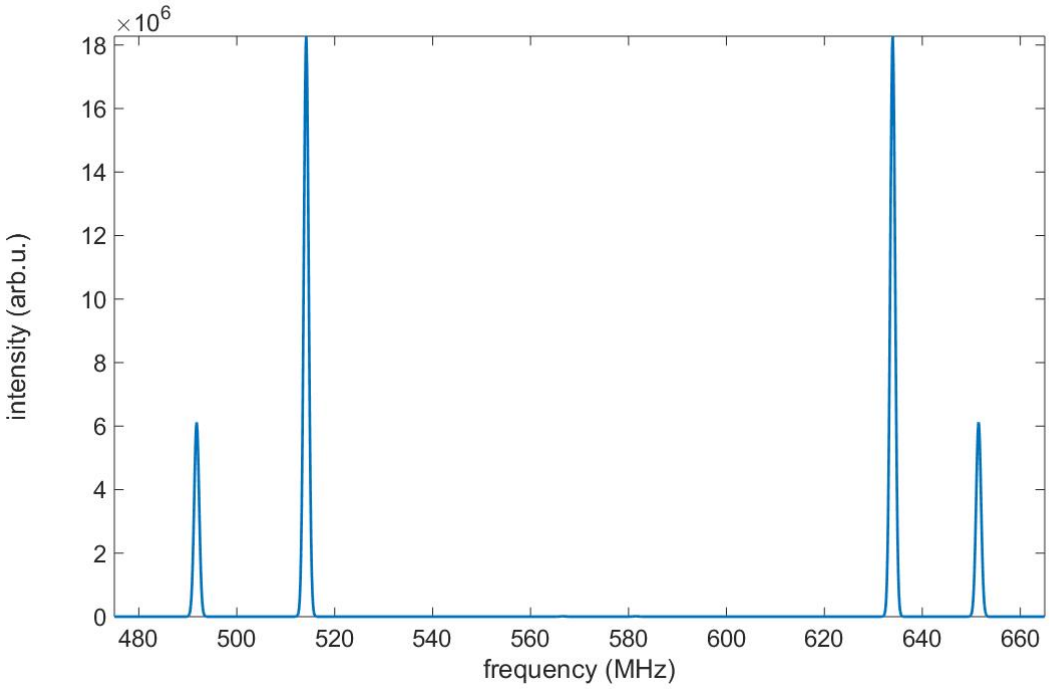

Figure 6.1: EasySpin simulation of the P1 center Hamiltonian for ^{15}N nucleus. The external field is 20.2 mT and the RF is perpendicular to the externally applied magnetic fields. The four orientations of the P1 center are shown. The center lines are the 3 degenerate misalinged orientations and the outer lines are the aligned $\langle 111 \rangle$ P1 centers.

explanation follows the source [31]. I use theory from Romanelli and Kevan [96] to find the final decay signal of the NV center ensemble spin-echo measurements. The following explanation holds for any 2 spin classes but for simplicity I will always label the operators in the Hamiltonian as being related to the NV or P1. Let us also assume the NV center is a quasi-spin 1/2.

The interaction Hamiltonian for a single NV center in a spin bath of k total P1 centers is shown in Equation 6.4 [31].

$$\frac{H_{int}}{\hbar} = \omega_0 S_z^{NV} + \omega_k \sum_k I_z^{P1} + \sum_k \frac{\gamma_{NV}\gamma_{P1}}{(|\boldsymbol{r_k}|^3)}(\boldsymbol{S^{NV}} \boldsymbol{I_k^{P1}} - 3(\boldsymbol{S^{NV}} \boldsymbol{n_k})(\boldsymbol{I_k^{P1}} \boldsymbol{n_k})) + H_B \quad (6.4)$$

ω_0 is the Larmor frequency of the NV center, ω_k is the Larmor frequency of the P1 centers. $\boldsymbol{I}$ is the spin operator for the P1 centers. $\boldsymbol{S}$ is the spin operator for the NV centers. $\boldsymbol{r_k}$ is the vector between the NV center and $P1_k$. γ_{P1} and γ_{NV} are the gyromagetic ratios of the P1 centers and NV centers respectively. $\boldsymbol{n_k}$ is the normalized vector between the NV center and $P1_k$, $\boldsymbol{n_k} = \frac{\boldsymbol{r_k}}{|\boldsymbol{r_k}|}$.

Let us start to simplify this Hamiltonian.

First, let us assume that during a measurement there is no change in the spin bath. This statement is known as the quasi-static regime. If this statement is true, we can drop the H_B term which includes interaction between the bath.

Next, let use assume the dominant polarization between the spins is along the z-axis and drop all non-secular terms. This occurs when the external magnetic field is larger

than hyperfine interaction of the P1 centers and the external field is aligned along the NV axis. This assumption can also be made at very large magnetic fields where the zero field splitting becomes a perturbation on the Hamiltonian. For our experiments we use relatively low magnetic fields (200G) aligned along the NV center axis.

Finally, let us bring the Hamiltonian into the rotating wave frame and assume the difference between the Larmor frequencies are large, $\omega_0 > \omega_k$ [105]. This statement is true for NV centers because of the NV zero field splitting of 2.87 GHz.

The interaction Hamiltonian for a single NV center in a bath of P1 centers becomes

$$H_{int} = \sum_k A_k S_z^{NV} I_z^{P1_k} \tag{6.5}$$

A_k is the interaction of the spin bath of P1 centers interacting with a singular NV center. Equation 6.6 shows the form of A given by Romanelli and Kevan [96] when the spins have the same quantization axis A becomes

$$A_k = \frac{\gamma_{NV}\gamma_{P1}}{|r_k|^3}(1 - 3\cos^2(\theta)) \tag{6.6}$$

This Hamiltonian is simply a spin with in a bath and has been well studied by the NMR community [2]. With this interaction Hamiltonian it is possible to simulate how a spin-echo of the NV center will decay.

The interaction Hamiltonian for a bath of NV centers in a bath of P1 centers is seen in equation 6.7

$$H_{int} = \sum_p \sum_k A_k S_z^{NV_p} I_z^{P1_k} \tag{6.7}$$

After applying a sequence with this Hamiltonian, one wants integrate over all spatial averaging of the NV spin configurations, where each NV sees a different P1 configuration. There are many excellent texts which describe how to do this integration, I refer the reader to [96] and [108].

For a spin echo sequence the an NV center will evolve in the following way

$$\rho(2\tau) = U(\tau)R_x(\pi)U(\tau)R(\pi/2)\rho(0)R_x^\dagger(\pi/2)U^\dagger(t)R_x^\dagger(\pi)U(\tau) \tag{6.8}$$

R is the rotation matrix about the x-axis described later in this chapter in Equation 6.19. The final signal which is read from the NV center is

$$\text{Signal} = \text{Trace}(\rho(2\tau)\sigma_y) \tag{6.9}$$

Using the notation of Romanelli and Kevan [96], after spatial averaging the final signal is proportional to a decay function $D(2\tau)$.

$$D(2\tau) = V_0 \exp\left(-8\pi^2/(9\sqrt(3))\gamma_N V \gamma_P 1\hbar n_{P1}\langle|X(t,s)||\rangle\right) \tag{6.10}$$

n_{P1} is the concentration of P1 centers in the system. γ_{NV} and γ_{P1} are gyromagnetic ratios for the NV centers and P1 centers respectively. The term $|X(t,s)|$ takes into account how the P1 centers can change over time during a measurement.

$$|X(t,x)| = \int_0^t s_{NV}(t')m_{P1}(t')dt' \tag{6.11}$$

s(t) is the magnetization of the NV centers and $m_{P1}(t)$ is the magnetization of the P1 centers.

The prefactor in D(t), $\frac{-8\pi^2}{9\sqrt{(3)}}\gamma_{NV}\gamma_{P1}\hbar$, for a diamond lattice is simplified to 292 kHz/ppm [108].

$$C = \frac{-8\pi^2}{9\sqrt{(3)}}\gamma_{NV}\gamma_{P1}\hbar C = 292kHz/ppm \tag{6.12}$$

By applying a π pulse on the P1 centers during a DEER measurement, one essentially changes the sign of the P1 interaction with the NV in the interaction Hamiltonian. A π pulse changes the sign of m_{P1} in the decay curve. Later in this chapter I will discuss how manipulating the P1 centers with microwaves can give decay curves where quantitative values can be extracted.

6.3 Correlation time

Before going into spin-counting it is necessary to ensure our diamond is in the quasi-static regime. All theory being used in this chapter makes this assumption. We do a correlation measurement to determine the time scale of our bath. A correlation measurement consists of stimulated echo [126, 127, 29, 63]. A stimulated echo can be thought of a Hahn echo where the central π pulse is split into 2 $\pi/2$ pulses. This measurement allows us to effectively store the phase collected on the z-axis and be T1 time scale limited. The final phase which is refocused is effected by the spin dynamics of the bath

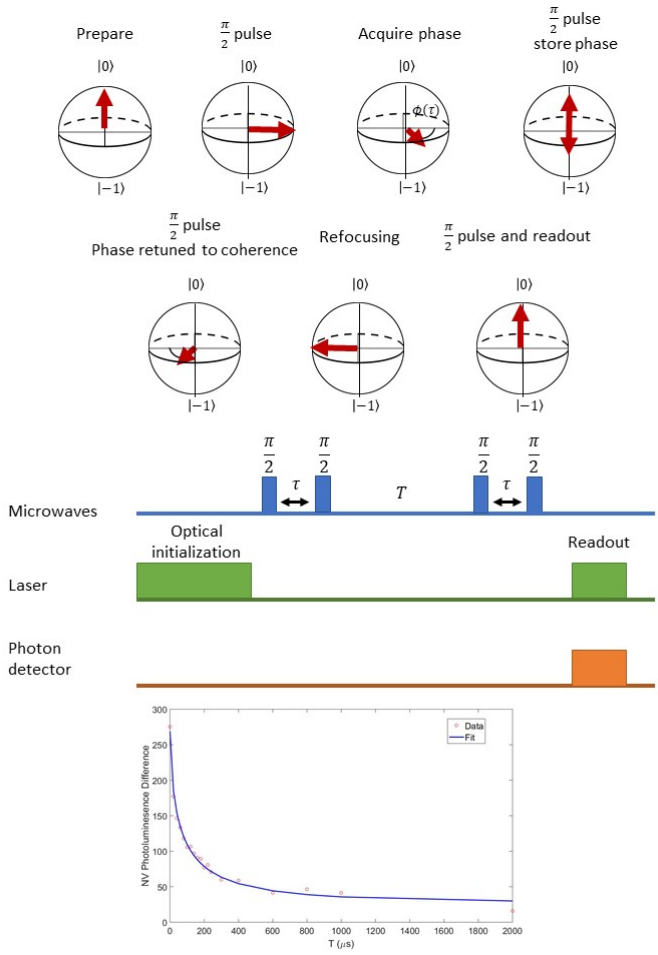

Figure 6.2: The pulse sequence, Bloch sphere representation and data for a correlation measurement. This decay after fitting to equation 6.13 is a correlation time of 1.7 ±0.4 ms. The bath has 22 ppm P1 centers. The rotations are always along the same rotation axis. The picture describes rotation about the x-axis.

in between the central π pulse. Figure 6.2 shows the measurement scheme, the Bloch sphere representation of the spin dynamics and the final signal. Stimulated echoes are very powerful measurements because they allow one to understand the spin environment on a time scale of T1 of the reporter spin.

When we analyze our data, we can use the fit function provided by Romanelli and

Kevan [96].

$$\text{CorrelationFit}(T) = A_0 \exp\left(-C n_{\text{Bath}} \frac{\tau}{2}\left(\frac{2\tau}{\tau_c} + \left(1 - \exp -\frac{2T}{\tau_c}\right)\right)\right) \tag{6.13}$$

A_0 is the photoluminesence prefactor for the NV center. C is the density prefactor defined earlier in the chapter. n_{Bath} is the density of the entire spin bath. τ_c is the correlation time. τ is the time the two pairs of $\pi/2$ pulses. T is the time between the second and third $\pi/2$ pulses.

Correlation time depends on the local spin environment, and hence will vary amongst spins. The distribution we use to describe this is for a magnetically diluted solid. This statement is valid since the spins are fixed in space in the diamond lattice and mostly interact with dipolar interactions. In Equation 6.15 W is frequency of a spin flip, f is the probability of a specific frequency of spin flips, W_max is the most probable frequency of spin flip [108, 100].

$$\tau_c = \frac{1}{W_{\text{max}}} \tag{6.14}$$

$$f(W, W_{max})dW = \sqrt{\frac{3W_{max}}{2\pi}} \frac{1}{W^{3/2}} \exp\left(-\frac{3W_{max}}{2W}\right)dW \tag{6.15}$$

W_{max} is the most probable rate of a flip in the bath of spins. The correlation time is defined as the inverse of W_{max}. It is the most probably time that a spin flip will occur. Because this distribution does not converge at infinity, we have to choose a time to cut

off normalizing to this function. When fitting our data we integrate this fit function between 0 and 10 MHz. 10 MHz was chosen because more than 90% of the spins are flipped with those bounds [108].

Our fit function to the data becomes

$$\mathrm{Fit}_{\mathrm{Correlation}}(T) = \frac{1}{\int_{0\mathrm{MHz}}^{10\mathrm{MHz}} f(W)dW} \int_{0\mathrm{MHz}}^{10MHz} f(W)\mathrm{SimpleFit}_{\mathrm{Correlation}}(T)dW \tag{6.16}$$

The fitting parameters are A_0, n_{Bath}, and $\mathrm{W}_{\mathrm{max}}$. This fit function gives us another way to probe the density of the entire spin bath. The density is often within the error bars for the P1 density measured via DEER. We experimentally see our density measurements measured with DEER and seen in figure 3.7 and using correlation measurements. This measurement gives us another way to check the density of our spin bath and know we are dominated by our P1 center bath. The diamond samples which we used to measure P1 densities all had correlation times greater than 1 ms. Because the DEER measurements occur on length scales of 2 - 30 μs, we assume we are in the quasi-static regime for our density measurements.

There are other ways to fit the correlation time as seen in references [63, 29]. It depends on what speed of the bath one wants to probe. It is possible to fit the beginning of the decay to an exponential and gain information about the fast flipping spins in the bath. One needs to fit the data in a way that makes sense to the questions being asked.

6.4 Double electron-electron resonance

We want to use the NV center to report information about its environment during optically detected magnetic resonance sequences. We will be using a class of measurements called double electron-electron resonance (DEER) to make the NV center ensemble reporter spins about the environment. DEER sometimes called electron-electron double resonance (ELDOR) is a class of measurements where an electron spin class senses another electron spin class [55]. This technique is particularly powerful when we have easy access to one spin class, in our case the NV center, but it is difficult to probe the other spins. It usually consists of two colors of microwaves being applied to two different resonant transitions. For spin-echo DEER measurements the coherence of the probe spin is changed when manipulating the pump spins. This phenomena allows us to use the NV center, which is very sensitive to its environment, to probe the P1 bath. Where traditional electron paramagnetic resonance (EPR) methods require 10^{12} spins or 10^{8} spins with state of the art equipment [36]. DEER techniques allow us to probe down to 10^{3} total spins. This number comes from the SNR we achieve in our samples after averaging for 1 day on 500 nm spots. We can also probe different areas of the diamond and map how evenly we incorporate P1 centers into the lattice during growth. Many groups have used DEER to understand the spin bath in diamond [62, 108]. DEER can also be used on single NV centers to probe near by spins [44, 97].

In the following sections I describe the information which can be retrieved using spin-echo DEER and correlation DEER sequences. I explain the sequences in an order which

I find easiest to understand. In practice, our measurements start with a simulation of the P1 spectrum so we know where to search for the resonant frequencies. We then apply spin-echo DEER while sweeping the frequency to know the exact transition frequencies. We apply correlation DEER to find the coherence time and Rabi frequency of our P1 centers. Finally, we do spin-echo DEER again to find the density of P1 centers. I will describe these measurements starting with the density measurement, followed by P1 spectra data, and ending with spin control measurements of the P1 centers.

6.5 Normalizing Data

Before we go too far into depth with DEER, I want to discuss what the y-axis "NV coherence means". In order to easily compare data and remove fluorescence change artifacts from the measurement we normalize our data by subtracting the projection of the signal on to the $|0\rangle$ and $|1\rangle$ states and dividing by the $|0\rangle$ and $|1\rangle$ fluorescence, equation 6.17

$$NVCoherence = \frac{|Sig\rangle_0 - |Sig\rangle_1}{|0\rangle - |1\rangle} \tag{6.17}$$

Any fluorescence change due to a transition into the neutral charge state is subtracted out. It is necessary to have the same dead time for all measurements to account for charge state changes. The division normalizes the fluorescence in a way that removes

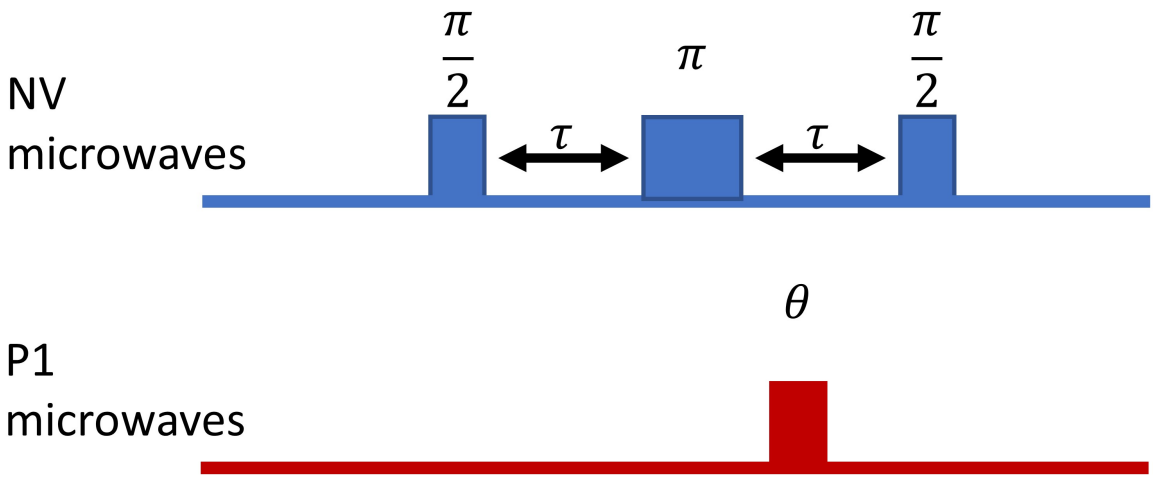

Figure 6.3: Generic spin-echo DEER sequence. A Hahn echo is sequence is applied to the NV centers which act as a probe and the P1 centers have an arbitrary length microwave applied

laser fluctuations.

6.6 Spin-echo DEER

Spin-echo DEER consists of applying a Hahn Echo on the NV center probe spins while applying a resonant pulse to a P1 center line. Figure 6.3 shows the general idea of the microwaves used for this sequence.

6.6.1 Spin-echo DEER for density measurements

When applying a Hahn echo sequence, one essentially decouples the NV center ensemble from the static magnetic field components of its environment. If you apply a π pulse on

the P1 centers simultaneously with the Hahn echo π pulse, one effectively recouples the static component of the P1 center coupling to the NV center signal. The denser the P1 center bath, the more the NV center will decohere due to the P1 center ensemble's π pulse.

To measure the density we use the pulse sequence shown in figure 6.4. The signal from this sequence can be calculated from equation 6.10. The values for the s_{NV} and m_{P1} are shown in table 6.1. When $T = 0$ the integral of $s_{NV} \cdot m_{P1}$ is zero, this means the static P1 bath doesn't couple into the Hahn echo at all.

Time	0 to τ	τ to $2\tau - T$	$2\tau - T$ to 2τ
s_{NV} value	1	-1	-1
m_{P1} value	$\pm 1/2$	$\pm 1/2$	$\mp 1/2$

Table 6.1: The values of m_{P1} and s_{NV} during a DEER spin-echo sequence. These values are used to calculate the decay signal.

The fit of the spin-echo DEER sequence becomes

$$\text{Fit}_{\text{SE-DEER}} = A_0 \exp\left(-C n_{P1} T\right) \tag{6.18}$$

Where C is the prefactor described earlier, n_{P1} is the density of P1 centers being flipped, and T is the time in the Hahn Echo sequence when the P1 π pulse was applied.

Because of the hyperfine structure as seen in figure 6.1, the decay constant of the exponential divided by C does not give the density of spins. More calibrations need to be done to extract the P1 densities

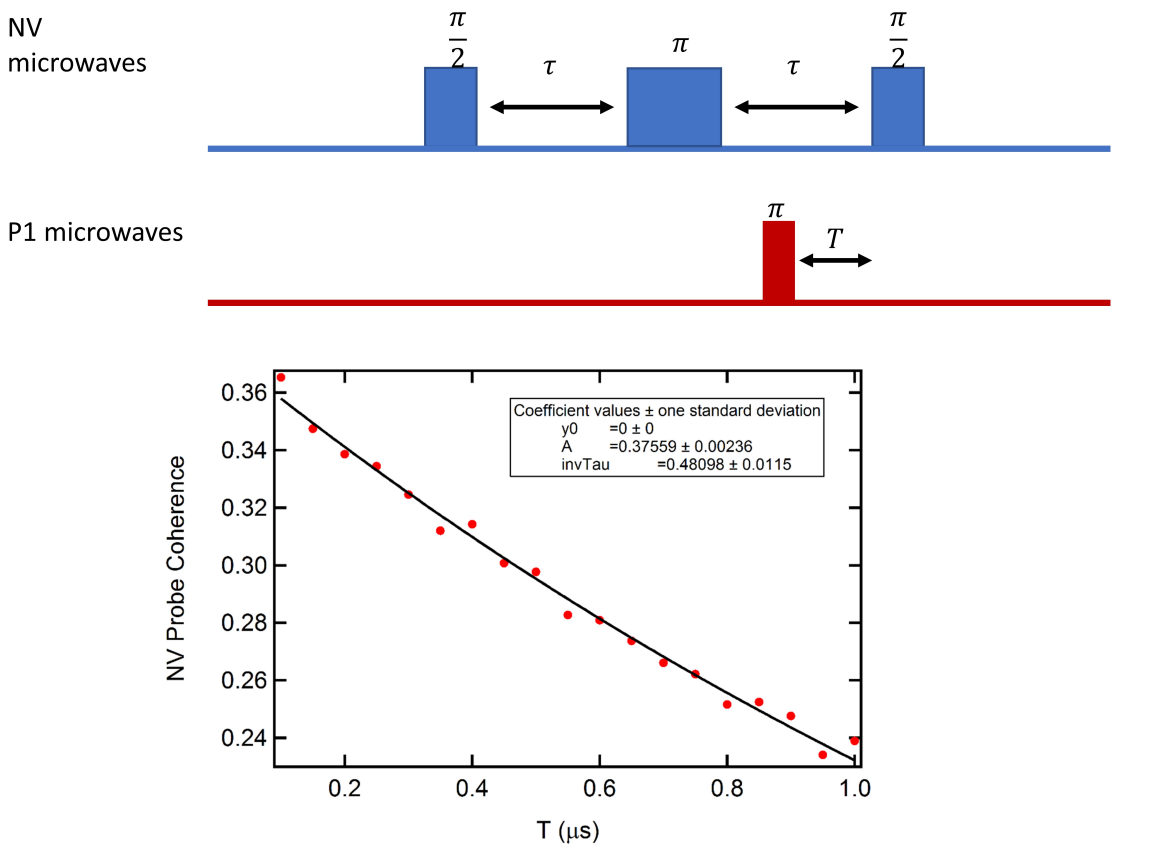

Figure 6.4: A pulse sequence for detecting the density of a spin class in diamond. We sweep a resonant π pulse into the Hahn Echo of the NV center. We keep τ of the Hahn echo fixed. The bottom shows the signal from this decay. When there is no P1 π pulse the coherence is high and as it is swept in the coherence drops.

6.6.2 Corrections to density measurement

The first challenge towards correct density measurements is that we do not drive every P1 center during a DEER experiment. We usually pick the most aligned P1 center hyperfine aligned to the external field. Because the next resonance is only 17 MHz away for ^{14}N and ^{15}N, we also drive some off resonance spins. We calibrate the fidelity of our pulse on the on-resonance and off-resonance spins and then calculate density. The B1 inhomogeneity, T_2^* of the P1 center, and offset frequency all effect the fidelity.

The inhomogeneity in the RF fields, sometimes called B1, is calculated by fitting an NV center Rabi. The Rabi time and T_2^* of the P1 center are found using a stimulated echo DEER explained later in the chapter.

Rabi simulations for density measurement corrections

This section details how to calculate the pulse fidelity of a Rabi experiment. We start with the rotation matrix for a Rabi experiment, R_x. This operator is for a rotation about the x axis when the drive frequency is off-resonant to the transition frequency. In this operator, t is the time the rotation is applied, Ω is the strength of the microwaves being applied, and δ is the offset of the drive frequency to the transition frequency.

$$R_x(t,\Omega,\delta) = \begin{pmatrix} \cos\frac{\sqrt{\Omega^2+\delta^2}t}{2} - i\delta\frac{\sin\frac{\sqrt{\Omega^2+\delta^2}t}{2}}{\sqrt{\Omega^2+\delta^2}} & -\frac{i\Omega\sin\frac{\sqrt{\Omega^2+\delta^2}t}{2}}{\sqrt{\Omega^2+\delta^2}} \\ -\frac{i\Omega\sin\frac{\sqrt{\Omega^2+\delta^2}t}{2}}{\sqrt{\Omega^2+\delta^2}} & \cos\frac{\sqrt{\Omega^2+\delta^2}t}{2} + i\delta\frac{\sin\frac{\sqrt{\Omega^2+\delta^2}t}{2}}{\sqrt{\Omega^2+\delta^2}} \end{pmatrix} \tag{6.19}$$

The density matrix of the spin after applying the Rabi rotation operator becomes ρ_{Rabi} see equation 6.20. The density matrix can be used to calculate the z projection, flip angle and fidelity of the pulse applied.

$$\rho_{\text{Rabi}}(\Omega, \delta, t) = R_x(\Omega, \delta, t)\rho_0 R_x(\Omega, \delta, t) \tag{6.20}$$

The fidelity of a pulse is calculated by taking the trace of the projection onto the one state.

$$\text{Fidelity} = Tr(\rho_{Rabi}(\Omega, \delta, t) \cdot \sigma_1) \tag{6.21}$$

The flip angle is calculated by taking the arccos of trace of the projection onto the z pauli matrix.

$$\text{Angle} = \arccos Tr(\rho_{Rabi}(\Omega, \delta, t) \cdot \sigma_z) \tag{6.22}$$

It is necessary to further correct these values by the spread in Ω caused by the inhomogeneity in B1 and the spread in δ caused by the linewidth of the transition frequency.

We assume a Gaussian distribution of B1 fields. The distribution is

$$G(f) = \frac{1}{2\pi} \exp -\frac{1}{2} \frac{f}{\sigma_\Omega}^2 \tag{6.23}$$

where f is a frequency. σ_Ω is the full width half max of the distribution in Rabi frequency Ω.

The distribution of the drive frequencies is a Lorentzian due to the mono-exponential decay of the Ramsey decay. Some of our decays are not exact mono-exponentials but the Lorentzian fit is fairly accurate for the spectrum. The parameter f is a frequency, $\Delta\omega$ is the detuning from the drive frequency and Γ is the line-width of the transition.

$$L(f) = \frac{1}{2\pi} \frac{\Gamma}{(\Delta\omega - f)^2 + (\frac{\Gamma}{2})^2} \tag{6.24}$$

We correct the fidelity by integrating over these line shapes. The corrected fidelity becomes

$$\frac{1}{\int_{-10\sigma_\Omega}^{10\sigma_\Omega} G(f)df} \frac{1}{\int_{-10\Delta\Gamma}^{10\Delta\Gamma} L(f)df} \int_{-10\Delta\Gamma}^{10\Delta\Gamma} \int_{-10\sigma_\Omega}^{10\sigma_\Omega} G(f_1)L(f_2)Re(Tr(\sigma_1 \cdot \rho_{Rabi}(f_1 + \Omega_0, f_2, t)))df_1 df_2 \tag{6.25}$$

For example, with the parameters found in table 6.2 we can correct the fidelity of our

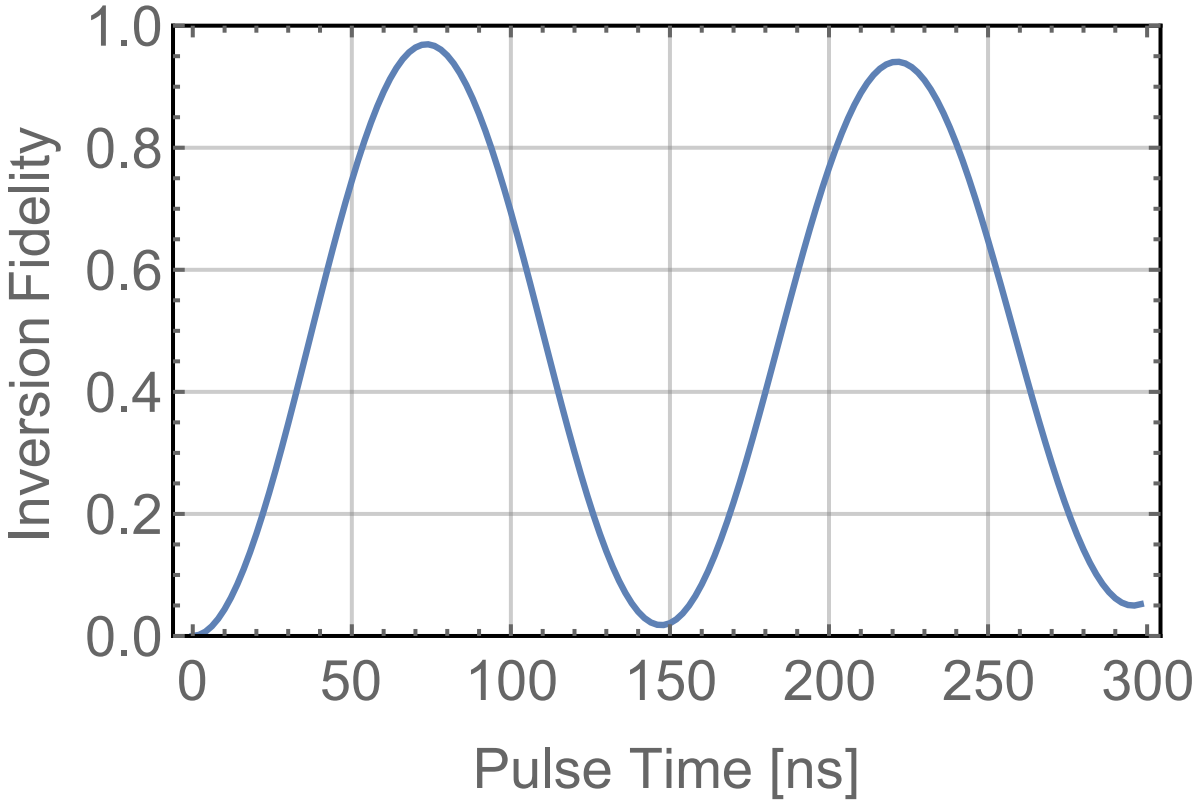

Figure 6.5: Simulation of the inversion fidelity during a Rabi experiment using parameters from table 6.5. Please note that at the "π" time the fidelity is not equal to 1.

π pulses as seen in figure 6.5

Parameter	Measured Value	Unit	Notes
Ω_0	$2\pi/(149)$	$rad \cdot GHz$	Average Rabi frequency
δ	0	$rad \cdot GHz$	Driving on resonance
Γ	0.0044	$rad \cdot GHz$	$2/T_2^*$
σ_Ω	0.0011	$rad \cdot GHz$	0.026Ω

Table 6.2: Table of experimental parameters used to simulate Rabi experiments

6.6.3 Calculating density from spin-echo DEER

The final density after correction for values becomes

$$\rho_{\mathrm{P1}} = \frac{invTau}{C} \frac{N_{HF}}{\mathrm{fid}_{\mathrm{OnResonant}} + 3 * \mathrm{fid}_{\mathrm{OffResonant}}} \tag{6.26}$$

As an exercise, let us work though a density measurement of the data shown in figure 6.4. The relevant values for the calibration are in table 6.3. Using those values the fidelity of the on resonance line is 0.98 and the fidelity of the off resonance line is 0.10. The decay constant for the data is 480 ± 10 kHz. The off resonance transition is actually 3 overlapped transitions. This data was taken on ^{14}N data where each line has 1/12 the total spin number. In ^{14}N each line as 1/12 the total spin number.

Parameter	2 π Rabi time (ns)	T_2^* (ns)	B1 inhomogeneity (%)
Value	93.4 ± 0.8	300	2.6

Table 6.3: Table of experimental parameters calibrate spin-echo DEER calculation

The B1 inhomogeneity is calculated from the parameter σ_Ω as seen in Equation 6.23. $\mathrm{B1}_{\mathrm{inhomogeneity}} = \frac{\sigma_\Omega}{\Omega}$. It is calculated by taking a Rabi measurement on an NV center. We assume the prefactor is the same for P1 centers and NV centers in the same location.

Parameter	inverse τ (kHz)	Fid. on res.	Fid. off res.	H.F. Correction
Value	480 ± 10	0.98	0.1	12

Table 6.4: Sample parameters to take into account for density measurements

$$\rho_{\mathrm{P1}} = \frac{480kHz}{292kHz/ppm} \frac{8}{0.98 + 3 * 0.10} \tag{6.27}$$

The P1 density of the sample is measured to be 15 ppm. In chapter 3 I show how we can use this measurement technique to feed back on our growth. Using DEER we were able to see how much nitrogen I was incorporating during growth. P1 density during growth was previously unknown due to the small spin numbers.

6.6.4 Spin-echo DEER for P1 spectrum measurements

To get the spectrum of the P1 centers using DEER we fix τ and T during a spin-echo DEER and sweep the frequency of the P1 centers. When the microwaves become on resonance with a P1 center transition, the coherence of the NV center will decay. In figure 6.6 I show the P1 spectrum for a ^{15}N sample as well as the EasySpin simulation and the pulses sequence for the microwaves. Because our external magnetic field and B1 field are not perpendicular we get forbidden transitions not seen in figure 6.1. The external magnetic field is aligned along the $\langle 111 \rangle$ axis of the diamond while the B1 is aligned along the $\langle 100 \rangle$ so they are 109.5 degrees from one another. In figure 6.7 I show a ^{14}N spectrum. When doing these measurements it is useful to use low microwave powers to prevent line broadening and turning spins from multiple spin classes. By fitting these spectrum we determine the resonant frequencies of our P1 centers used in the density measurement.

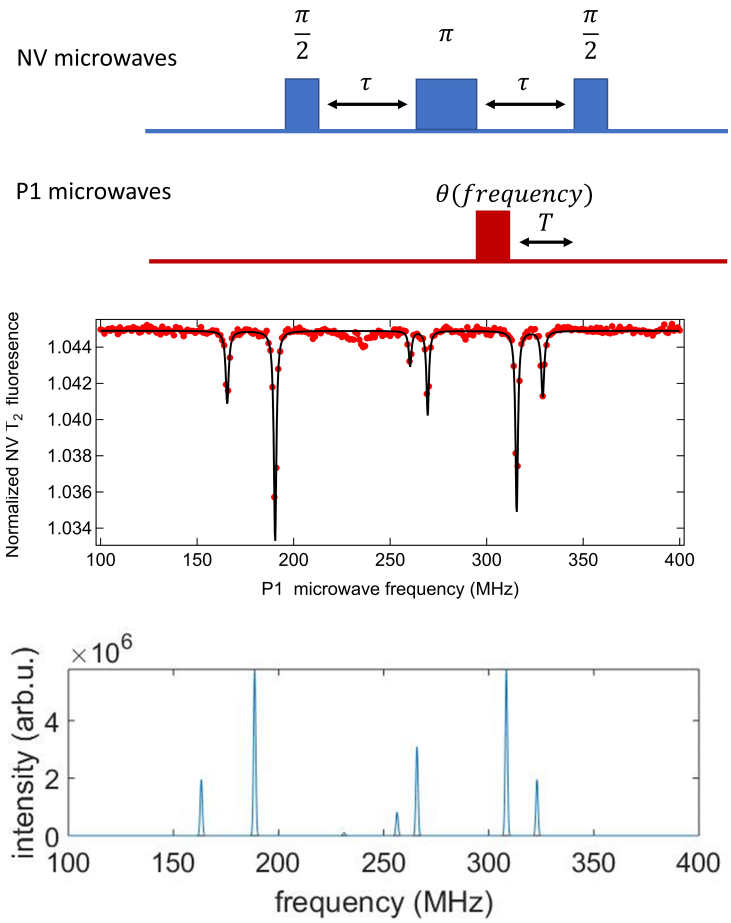

Figure 6.6: ^{15}P1 spectrum taken using spin-echo DEER. The top plot is data. The bottom plot is an EasySpin simulation. The field for this experiment was 8.2 mT. The central two peaks are double quantum flips between the nuclear and electron spins, which are allowed because the external magnetic field and B1 are not perpendicular.

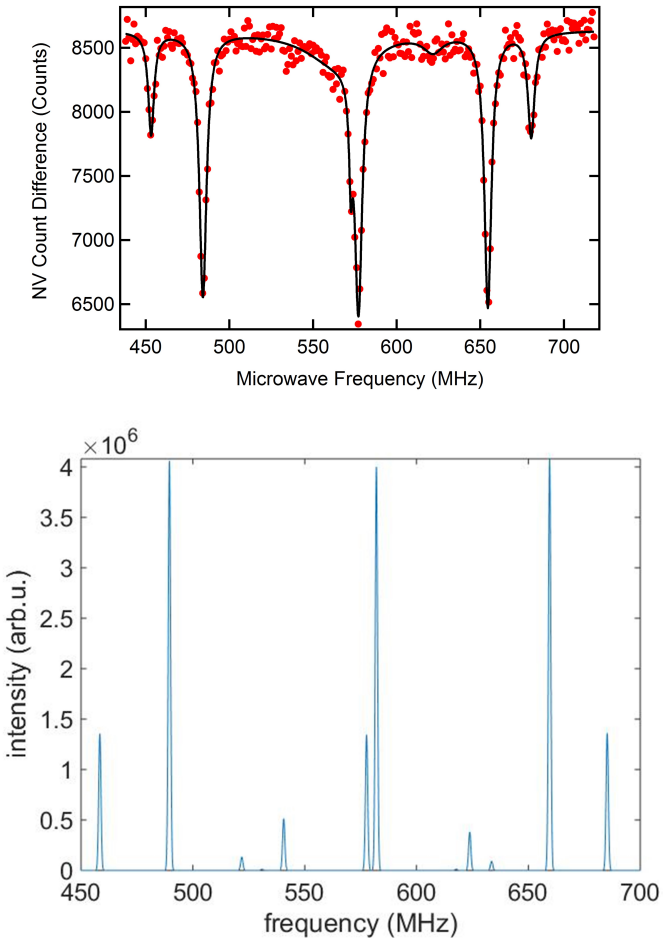

Figure 6.7: ^{14}P1 spectrum taken using spin-echo DEER. The top plot is data. The bottom plot is an EasySpin simulation. The field for this experiment was 20 mT. The peaks between 500 MHz and 650 MHz occur due to double quantum transitions between the nuclear and electron spins. They are allowed because the external magnetic field and B1 are not perpendicular.

6.7 Stimulated-echo DEER

Stimulated echo DEER or 3-pulse DEER provides a way to probe the P1 center bath on a time scale of T1 of the NV center [88].

6.7.1 P1 Rabi Experiment

Changes in the P1 bath will change the coherence of the NV center, which changes the fluoresence of the NV center during readout. During a Rabi experiment the P1 spins are turned which changes the refocusing after the third NV center probe $\pi/2$ pulse. The largest change in the spin bath occurs when the P1 centers have totally flipped, a π pulse. No change occurs to the coherence when the spins are returned to their original state, a 2π pulse. Figure 6.8 shows an example of this experiment. Fitting to the oscillations gives the Rabi time of the P1 center used during P1 density measurements.

6.7.2 P1 Ramsey Experiment

A Ramsey measurement can be performed on the P1 centers in much the same way as the Rabi. As the P1 center polarization on the z-axis after the second P1 $\pi/2$ pulse the coherence of the NV center changes at the end of the stimulated echo. When the P1 center is fully decayed it has equal polarization difference on the z-axis and the NV center coherence stops changing. The coherence changes because the phase accumulated in the first τ is different from the phase accumulated in the second τ.

When fitting the data it is important to take into account that the strength of the

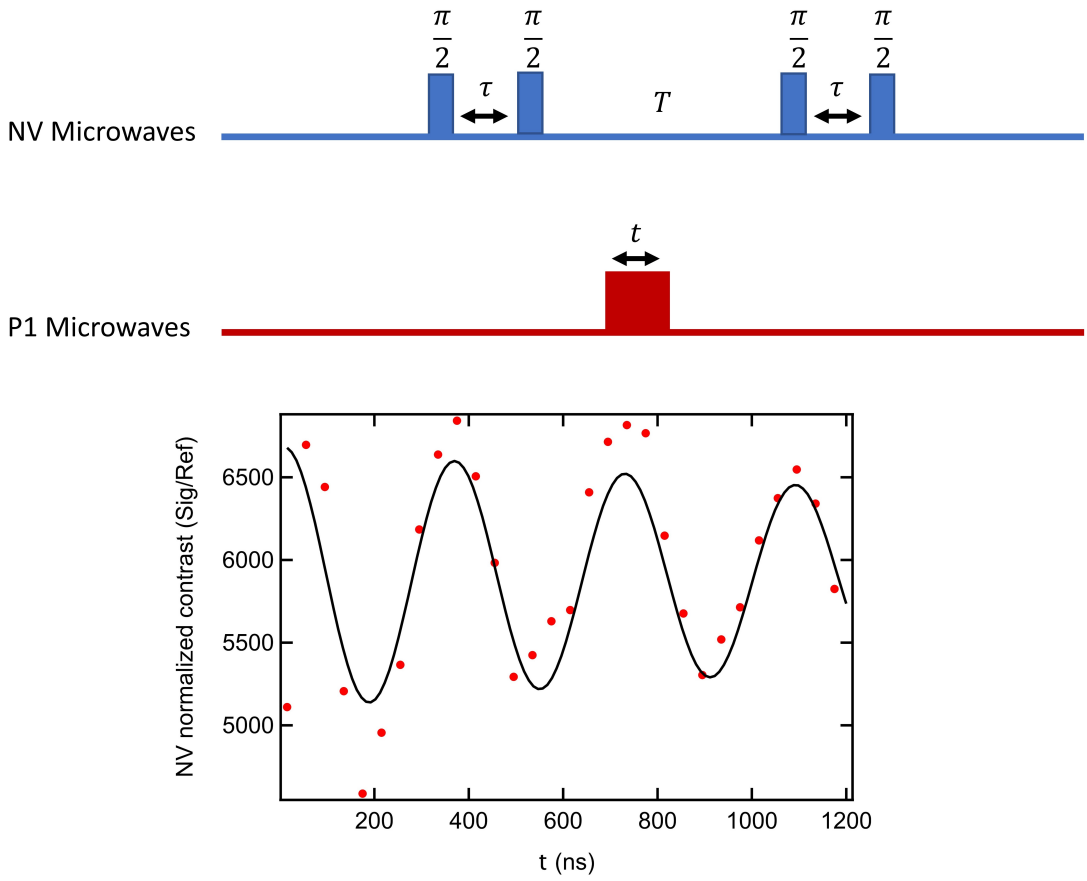

Figure 6.8: This figure shows how a Rabi sequence on the P1 centers between the second and third $\pi/2$ pulses on the NV center. Changes in the P1 bath will change the coherence of the NV center, which changes the fluorescence of the NV center during readout. The difference between the $|0\rangle$ and $|1\rangle$ states is plotted versus the length of the pulse applied to the P1 center. In this measurement the P1 center has a Rabi time of 360 ± 4 ns.

curve is modulated by the NV coherence. The Ramsey signal comes as an exponential in the NV center signal. The fit is shown in equation 6.28

$$\text{Stim. Echo Sig.} = A_0 \exp -(\sum_N B_N \cos\left(2\pi\delta_N + \phi_N\right) \exp -\frac{t}{T^*_{2N}}) \tag{6.28}$$

In this fit A_0 is a calibration factor to photon counts. N is the number of P1 resonances being addressed by the pulse sequence. In the case of figure 6.9, N is 2 because two lines are being addressed. One line has one orientation of P1 centers spins and the other has three overlapped orientations of P1 center spins. T^*_{2N} is the coherence time of the Nth transition. δ_N is the offset frequency of the microwaves to the transition frequency. ϕ_N is the offset phase of the signal for the Nth transition frequency.

6.8 NV density analysis

Because sensitivity of a magnetometer scales with $\frac{1}{T^*_2 N_{NV}}$, where N_{NV} is the number of NV centers, it is important to count the NV centers in the magntometer to accurately gaugee the sensitivity. The rest of this chapter is dedicated to accurately measuring the NV ensemble density. The three methods we use are direct counting, DEER between NV centers, and instantaneous spectral diffusion. Much of the theory used for P1 centers is also used for counting NV centers. The subtleties between measurements are described in each section. The two larges differences between P1 center counting and NV center counting are taking into account the spin 1 nature of the NV center and accounting for the zero field splitting along the crystal axis.

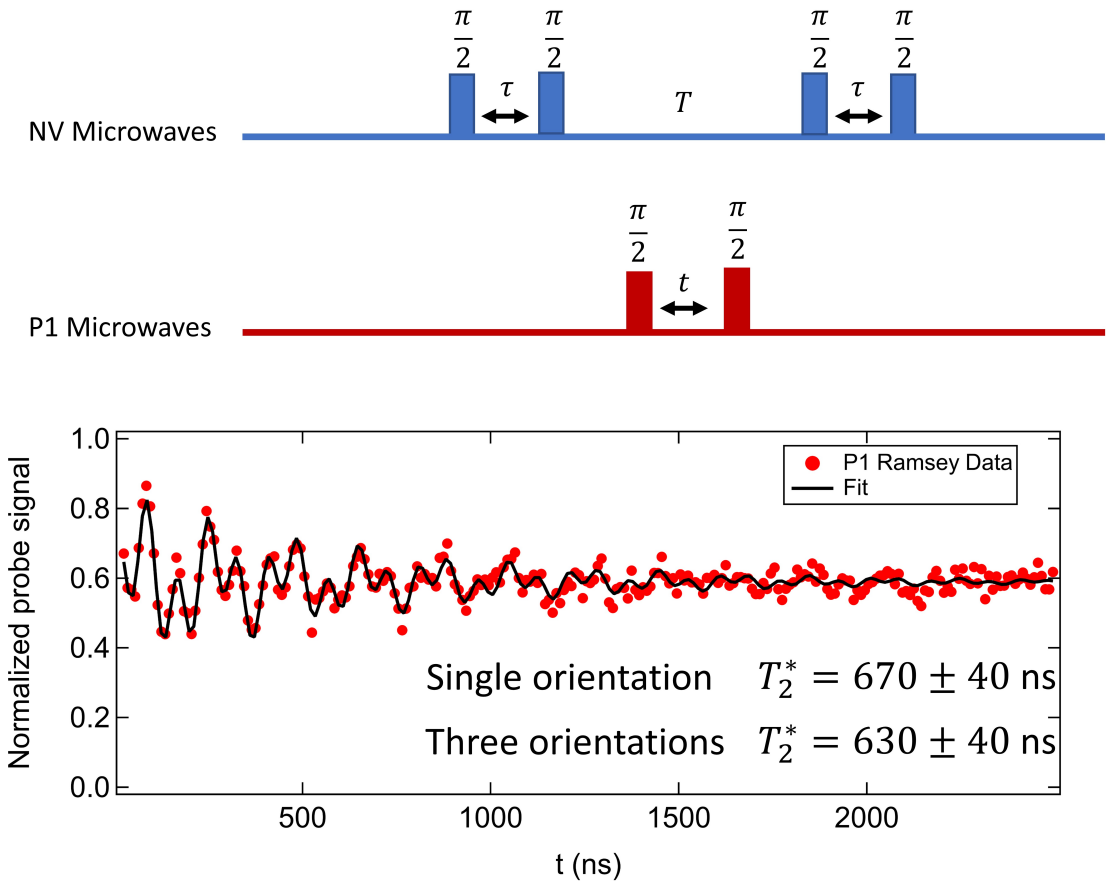

Figure 6.9: This figure shows the pulse sequence applied to retrieve the T_2^* of the P1 centers.

6.9 Counting NV spins

When spin numbers are low enough the NV centers can be counted and small ensembles can be estimated using a maximum likely estimate. Counting NV centers can be done by looking at the spin interactions between different orientations of the NV centers, this method is doing DEER between NV centers. Finally, one can probe the NV center interaction between its own spin class to estimate the density. This method is known as instantaneous spectral diffusion.

6.10 Maximum likelihood estimation

This section is adapted with permission from the supplement of C.A. McLellan *et al* Nano Letters 2016, 16, 4, 2450-2454. Copyright (2016) American Chemical Society [76].

For small ensembles it is possible to count the number of hyperfine signatures in a diffraction limited spot and estimate the density using a maximum likelihood estimation [128]. For electron irradiated nitrogen δ-doped samples this method was used. In an irradiated area we know the probability (P) of finding one to four 15N hyperfine orientations (l) in a diffraction limited spot. We assume a Poisson distribution of our NVs over the irradiated area. Using equation 6.29 and numerically solving in Mathematica, we estimate , the estimated number of NVs in a diffraction limited spot.

$$P(l,\lambda) = \sum_{n=1}^{\infty} \frac{\lambda^n \exp(-\lambda)}{n!} \left(\frac{S(l,n)}{4^n} \frac{4!}{(4-l)!}\right) \tag{6.29}$$

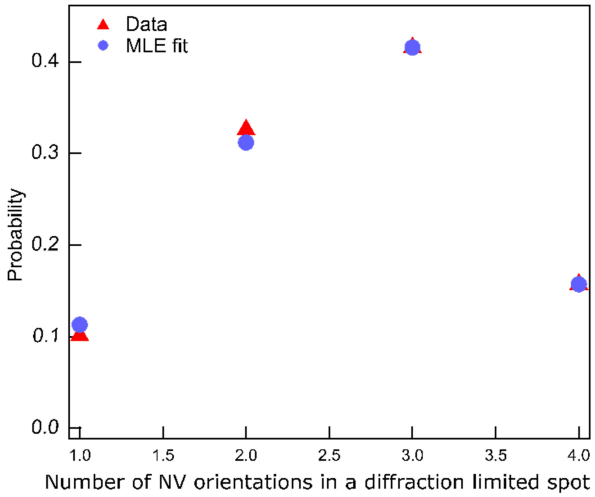

Figure 6.10: The probability of finding 1 to 4 NV orientations in a diffraction limited spot for the irradiation dose $2 * 10^{18} e/cm^2$ with 200 keV incident electrons. The red triangles is the data for a 27 μm^2 area. The blue circles is the MLE fit to the data.

This equation sums over all possible number of NVs (n) from 1 to infinity. S is the Stirling number of the second kind, which accounts for the number of ways n number of NVs can be sorted into l number of orientations. Figure 6.10 shows the data for the a 200keV election irradiation spot with a dose of $2x10^{1}8e/cm^2$. The red triangles are the data and the blue circles is the MLE fit using λ of 4.18 NVs in a diffraction limited spot.

6.11 NV-NV DEER

NV-NV DEER density measurements are performed the same way as NV-P1 DEER density measurements. Because our external field is aligned along the $\langle 111 \rangle$ we use the three misaligned NV centers as our probe and our aligned NV centers as our pump. There

is an extra correction factor because the NV centers do not have the same z-axis due to the zero field splitting. The correction is seen in the interaction Hamiltonian between the NV centers. The A term in equation 6.6 becomes

$$A_{NV,NV} = \frac{\gamma_{NV}\gamma NV}{|r_{p,k}|^3}(\frac{1}{\sqrt{\tan^2(\alpha)+1}})(1-3(\frac{\tan(\alpha)}{2}\sin(2\theta)\cos(\phi)+\cos^2(\theta))) \quad (6.30)$$

Spatial averaging has an analytic solution when the spins are all parallel or perpendicular to one another, $\alpha = 0$ and $\alpha = 90°$ respectively [96]. The spatial averaging of the signal must be done numerically. For NV centers where $\alpha = 109.4°$ the spatial averaging needs to be done numerically.

The final result is the prefactor C is corrected by $\frac{1}{0.86}$.

6.12 Instantaneous spectral diffusion

This section focuses on how to measure a Hahn echo and detect the instantaneous diffusion phenomenon. The basic idea of instantaneous diffusion is to decouple the probe spins from the probe spin ensemble. Instantaneous diffusion measurements can be thought of as doing DEER measurements on the probe spins. Decoupling is done by changing the central π pulse on the spin to flip fewer probe spins during a Hahn echo (fig 6.11). By plotting $\frac{1}{T_2^*}$ versus the fidelity of the central pulse one can extract the density of the probe spins (fig 6.13). [4] [125]

I first describe the data taking technique then end with analysis of final signal. To

extract a correct density it is necessary to collect and analyze the coherence data correctly. Three important considerations to address are removing the FID that leaks into the signal at short times for $\theta \neq \pi$, correctly calculating the fidelity for a given pulse length, and normalizing the data to easily fit the data.

Phase Cycling

Phase cycling is a method to suppress unwanted signals while selecting only wanted coherence pathways by systematically changing the phase of the pulses applied and linearly adding or subtracting the signals together [39].

Figure 6.11 demonstrates why phase cycling is necessary for an instantaneous diffusion measurement. We assume the $\pi/2$ pulses create perfect coherences. The central θ pulse can be though of doing a perfect π pulse on the instantaneous diffusion signal spins and not interacting with the remaining spins. The remaining spins, shown in purple, continue precess along the Bloch sphere and will detected as an FID signal on top of the echo decay signal.

In table 6.5 we show that by changing the central θ and final $\pi/2$ pulses in 90deg changes and linearly combining these signals it is possible to achieve the final signal with four times the echo signal and no FID signal [109].

Phase cycling in stimulated echoes is also possible and described in reference [113]

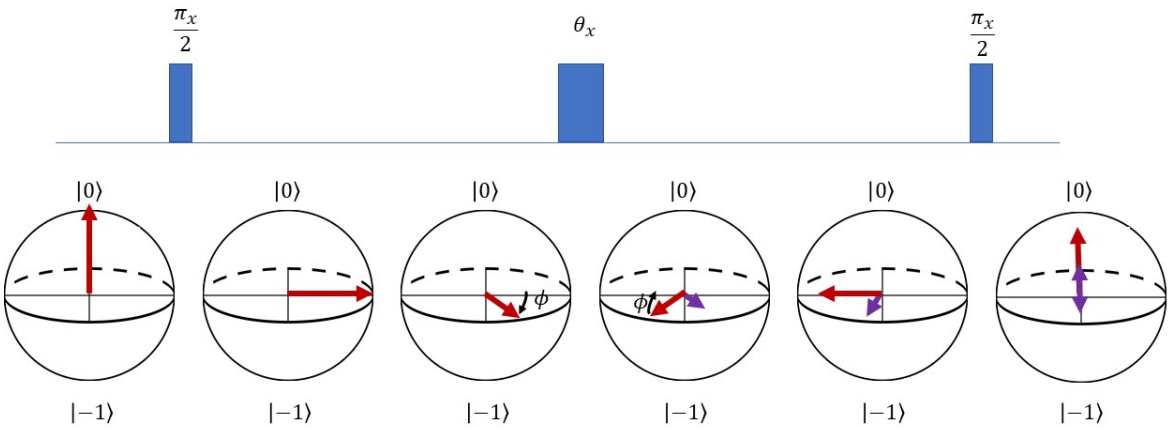

Figure 6.11: This sequence demonstrates on the Bloch sphere how an FID signal can leak into the Hahn echo signal when the central pulse is not a π pulse. This image assumes the $\pi/2$ pulse create perfect coherences. This picture shows rotation pulses all about the +x-axis

Pulse Label	Phase of pulses	Hahn Echo Sign	FID Sign
A	$\frac{\pi}{2}_x - \theta_x - \frac{\pi}{2}_x$	+	+
B	$\frac{\pi}{2}_x - \theta_x - \frac{\pi}{2}_{-x}$	−	−
C	$\frac{\pi}{2}_x - \theta_y - \frac{\pi}{2}_x$	−	+
D	$\frac{\pi}{2}_x - \theta_y - \frac{\pi}{2}_{-x}$	+	−
$Signal = A - B - C + D$		4 $\text{Signal}_{HahnEcho}$	0 Signal_{FID}

Table 6.5: A chart describing the sign of the Hahn Echo and FID signal for each combination of pulse phases.

Fitting data

Finally it is necessary to discuss how to fit the data. The theory of fitting this data requires that the decay be a mono-exponential. There are two ways to extract this data

1. Fit the entire decay with an added mono exponential for each θ

2. Fit to short τ when the decay matches a mono-exponential

Fitting full decay

$$Signal = y_0 + A(1 + B\cos^4\frac{2\pi\tau}{T_c})\exp -\left(\frac{\tau}{T_{2Fix}}\right)^n \exp -\left(\frac{\tau}{T_{ID}}\right) \tag{6.31}$$

In this decay y_0 is set to 0 because the decay goes to 0 at time infinity. The parameter B is the strength of the ^{13}C peaks. T_C is the rate of the ^{13}C revivals. The fixed decay time of the system is T_{2Fix}. Exponential prefactor is n. The added decay time during instantaneous diffusion is T_{ID}. The time being between the pulses is τ.

Once one curve is fit for all parameters, the other flip angle data can keep only T_{ID} as a fitting parameter.

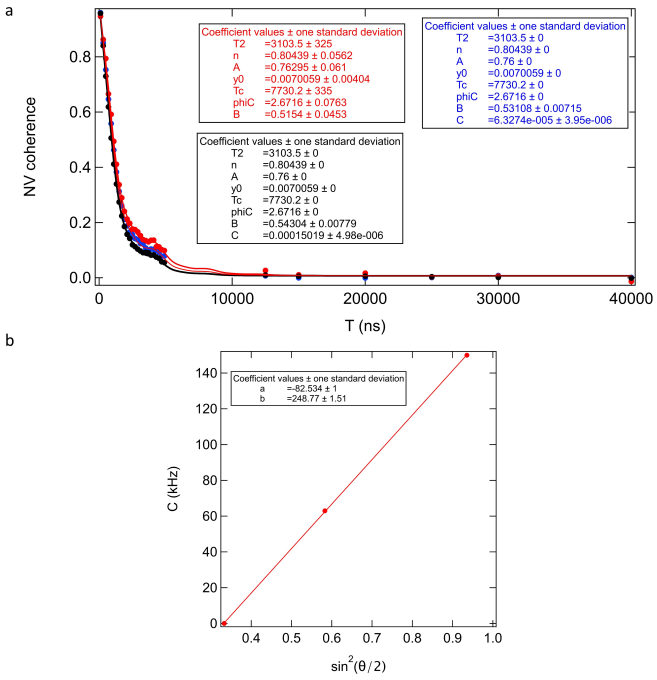

Figure 6.12: a) Decay from fitting the whole decay but adding an extra mono-exponential decay. b) is the data analyzed to extract density.

An example of this data set is seen in Figure 6.12.

Fitting short Tau

Because the decay constant for our Hahn echo signals is not fit to a mono-exponential, it is difficult to extract correct densities fitting the entire curve with free parameters. To get around this only a small section of points can be fit. The fit function becomes

$$Signal = y_0 + A(1 + B\cos^4\frac{2\pi\tau}{T_c})\exp - \left(\frac{\tau}{T_2}\right) \tag{6.32}$$

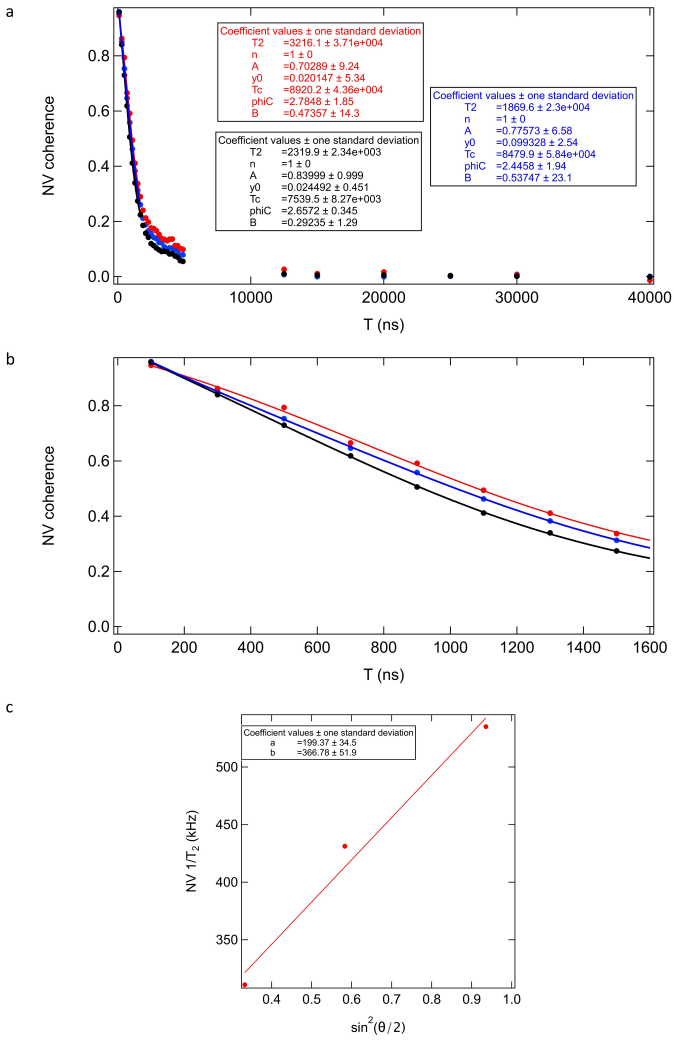

Figure 6.13: Measuring ID at short tau. A) fit compared to the full decay b) zoom in of the fit points c) the density extacted from this method

An example of this data set is seen in Figure 6.13.

6.12.1 Analyzing instantaneous diffusion data

For each pulse used it is necessary to calibrate it to an angle using the Rabi simulations described earlier in this chapter. When $\frac{1}{T_2}$ versus the fidelity of the angle θ applied $(\sin^2\theta/2)$ a line should be formed. The slope of this line is proportional to the density of NV centers being addressed. One can think of the fidelity at 1 is equal to the entire spin bath decohering itself. At a fidelity of 0, which can never be reached but theorietically projected to, the spin echo is totally decohered from the bath.

The slope is proportional to the density with the same prefactor C, 292 kHz/ppm. When addressing an aligned NV class the density of the entire NV center ensemble

$$n_{NV} = \frac{4\text{Slope}}{C} \tag{6.33}$$

Using this data analysis we are able to extract NV densities such as those found in chapter 4. For the data shown the NV density was measured to be 3.40 ± 0.01 ppm NV centers in the diamond. This value is coming from the analysis shown in Figure 6.12.

6.13 Future work

Being able to probe dark spins in the bath opens up a lot of opportunities for both fundamental physics experiments, sensing exotic spin systems, and engineering better magnetometers.

Using high density samples and many of the techniques applied here groups have seen non-equilibrium spin dynamics [24, 23, 62]. One can think of applying these techniques to dense 2-D layers and exploring physics in that regime.

Understanding near surface spins is an outstanding challenge in NV centers and could open new ways to probe phenomena at the surface. Applying DEER techniques could allow for more information and sensing capabilities near the surface [98, 95].

Being able to detect small numbers of dark-spins is very powerful. There is plenty of room to explore more.

Chapter 7

Bio-sensing

There are many interesting biological magnetic signals [129]. There are bacteria which house magnetic nanoparticles [11], birds use magnetism to help them navigate [131], and electrically active cells such as neurons and cardiomyocytes (brain cells and heart cells) can produce magnetic fields when signaling [133, 130]. Many of these signals are still poorly understood due to lack of proper instrumentation for the signals. In the Jayich lab we have been focused developing a tool to image the magnetic fields of neuron action potentials.

This chapter could not have written without the help of the Glanzman lab at UCLA who showed Tim Eichhorn how to dissect Aplysia. Tim went on to teach me and the dissection section of this chapter comes from Tim's notes. Prof. Carol Vandenberg allowed us to use her patch clamp equipment and taught us how to make a cell medium. The Oakley Lab kindly let us use their lab space for some of our experiments and perform

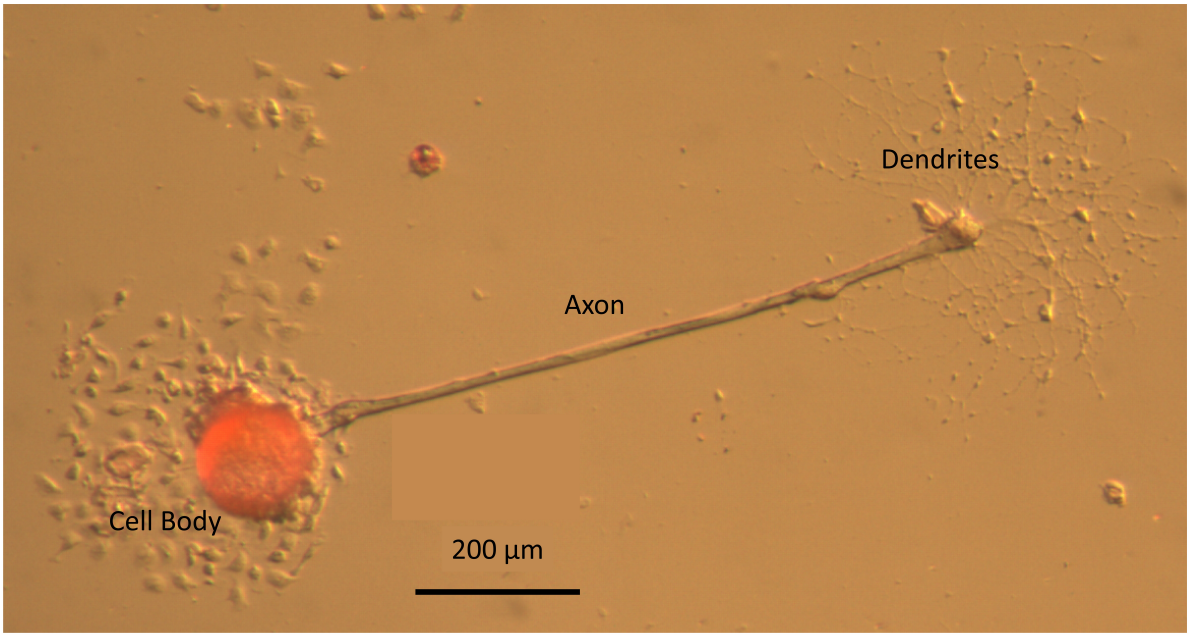

Figure 7.1: *Aplysia californica* neuron: A neuron from an aplysia extracted and plated by the Jayich lab.

the dissection of aplysia. Desmond Ramirez in the Oakley Lab helped train us in many of the experimental techniques in this chapter.

7.1 Neurons

Neurons are the signaling cells in the nervous system of animals. They are responsible for brain activity and sensing. They consist of cell body, an axon and dendrites. A neuron can send an electro-chemical signal down its axon to communicate with other neurons and receive signals [18]. Although first discovered in 1865, studying neuron action potentials is still active area or research [101]. There are many ways to detect neuron action potentials below are a few common ways to detect neurons today.

7.1.1 Detecting single neuron action potentials

Biologists currently have many tools to detect neuron action potentials. Most them consist of detecting the electrical signals associated with action potentials rather than the magnetic signals. The challenge with detecting electrical signals is the Debye length inside a cell medium is only a few nanometers [75]. This length scale requires electrical signal detectors to be very close to the neuron and therefor are invasive methods.

Electrophysiology

Electrophysiology consists of bringing a micro-electron inside, near or just at the surface of the cell and another probe inside the medium surrounding the cell. The probes can measure the current through the cell membrane or the voltage drop across the cell membrane to the surrounding medium. The first method is called voltage-clamp and the second method is called current-clamp [83]. Using a voltage-clamp method Hodgkin and Huxley recorded the action potential of a squid (the animal not the sensor) axon in 1952 [50, 49]. Using this data they were able to detect the ion currents and created a simple electrical model for neurons. This method of electrophysiology is still commonly used.

One can also current clamp the cell where the current between two electrodes is kept constant. When the voltage drop across the cell membrane goes above a critical value the cell will have a rapid change in voltage. This change in voltage is the action potential.

Voltage sensitive dyes

Voltage sensitive dyes allow for sensing of neurons all optically. The dye sits on the cell membrane and will change its fluorescence intensity or color depending on the voltage drop across the membrane. A laser is then used to excite the dye. By mapping the fluorescence of the dyes with an optical microscope and photon detector or camera it is possible to map out the action potentials. The limitations with this method is the laser used is photo-toxic and the dyes them selves can also be toxic, limiting the amount of time an experiment can be performed [20].

Calcium dyes

Similar to voltage sensitive dyes, calcium dyes change their fluorescence in the presence of calcium ions. These dyes can also be photo-toxic limiting the amount of time they can be used [51].

Nano-wires

Nano-wires are a variation on a theme of the electro-physiology techniques. Rather than a large electrode, small nano-wires are brought very close to the cell. This method is much less invasive than traditional electro-physiology but it still requires the neuron to be in contact with the wire [89].

Figure 7.2: *Aplysia californica*: Picture of an aplysia in the Jayich lab's tank in the Marine Science building at UCSB.

7.2 Aplysia californica

The model animal we studied is the *Aplysia californica*. It is a snail native to Santa Barbara and is a model animal for many biological studies [79]. Their neurons have lead to many breakthroughs in neuronscience [41]. Figure 7.2 shows an picture of one of the aplysia used in our experiments.

7.3 Aplysia californica Experiments

To do experiments we needed to plate neurons on diamond. Although diamond is biocompatible, making a biocompatible diamond probe is non-trivial as many glues are toxic.

What we found is gluing our samples with Norland glue to a glass coverslip did not limit the lifetime of the neurons.

To do neurophysiology experiments it is necessary to electrically isolate the RF from the cell bath. We did this be depositing the metal for the waveguides in the order Ti:Au:Pt 10:300:10 nm. Then we coved the waveguides with silicon dioxide using a plasma enhanced chemical vapor deposition (PECVD) tool in the nanofabrication facility. We deposited the silicon dioxide in two steps to prevent pinholes from forming.

7.4 Plating neurons on diamond

To plate the neurons we used a method derived from the Glanzman lab at UCLA. These directions come from notes written by Tim Eichhorn. We also referenced work by Zhao and colleagues to prepare the neurons [136].

7.4.1 Preparation of materials

Preparing L15 medium

This section describes how to prepare the cell medium.

1. Measure 90 mL of distilled water in a graduated cylinder

2. Pour water in a beaker and stir with a magnetic stir plate while adding L-15 pounder. While stirring add all the salts in the order given in Table 7.1

Material	Type
L-15 with L-glutamine	13.8 g/l
NaCl	12.5 g/l
Dextrose	6.24 g/l
$MgSO_4$ $7H_2O$	6.42 g/l
KCl	344 mg/l
$MgCl_2$ $6H_2O$	5.7 g/l
$CaCl_2$	1.49 g/l
HEPES	3.53 g/l

Table 7.1: Materials needed for L15 medium

3. Using a pH meter, adjust the pH to between 7.4 and 7.5 by adding 1 M HCl or 1M NaOH

4. Fill solution back into graduate cylinder and add distilled water to match the final volume needed and seal with a parafilm

5. Add 10 ml/l of 100x pen/strep

6. Sterilize by sending solution through a filtration system

7.4.2 Hemolymph collection

When working with aplysia it is necessary to store their neurons in aplysia hemolymph.

The collection was done with the following steps

1. Place aplysia in bucket with sea water. Add ice to the bucket.

2. Swaddle animal in a soaking pad so only the head is exposed.

3. With a sterolized razor blade make a 1 cm cut between the eyes

4. Collect the hemolymph in a 1000 ml beaker by holding the animal gently.

5. Dispose of the animal

6. Prepare the hemolymph in pairs of 50 ml aliquots and cnetrifuge in a 4C walk in fridge around 6000 rpm for 15 min. The supernatant should be clear.

7. Aliquot the supernatant in a 10 ml Falcon tube and store at -80 C

7.4.3 Protease

Protease was used to digest the tissue surrounding the neurons. Mix protease at a ratio of 10 mg/ml with L15 cell medium. The protease used is Sigma 049242078001

7.4.4 Cell medium

To prepare the cell medium combine 10 mL of hemolymph wiht 10 mL of L15 medium. Add 200 μl of L-glutamine (Sigma 59202C) as a nutrient for the plated cells.

7.4.5 Preparing the diamond

In order for the neuron to adhere to the diamond probe, the diamond has to be coated with a protein called Poly-L-lysine.

1. Mix 1 mg/ml poly-L-lysine in a borate solution (ph 8.2)

2. The Borate solution is 0.1 M Ma Borate and water

3. Cover the diamond with PLL solution over night.

4. Aspirate the diamond probe with saltwater 5 times.

5. Dry the diamond probe under a UV light for at least 1 hr

6. Place 2 ml of culture medium in the diamond probe dish

7.4.6 Glass pipettes

Glass pipettes were pulled using Sutter instruments BF150-86-7.6HP from the Vandeberg lab. These pipettes are pulled to about 500 nm tips and short enough to have some stiffness.

We used the parameters, pressure = 300, heat = 730 , pull = 60, velocity = 80, time = 200. I am not sure what the units are for this tool.

7.4.7 Aplysia dissection

Using a 60 ml syringe, a solution of MgCl in water was injected into the animal as an anesthetic. The animal is then pinned into a Sylgard dish 7.3

After being pinned to a dish and covered in sea water, one needs to make incissions. A small cut is made near the mount of the animal then an incision is made down the length of the animal. In Figure 7.4 one can see the organs inside the aplysia. The pleural-pedal ganglia are the orange dots marked by the arrow. Those ganglia house the neurons used in our experiments.

Figure 7.3: Aplysia pinned to a Sylgard dish for dissection

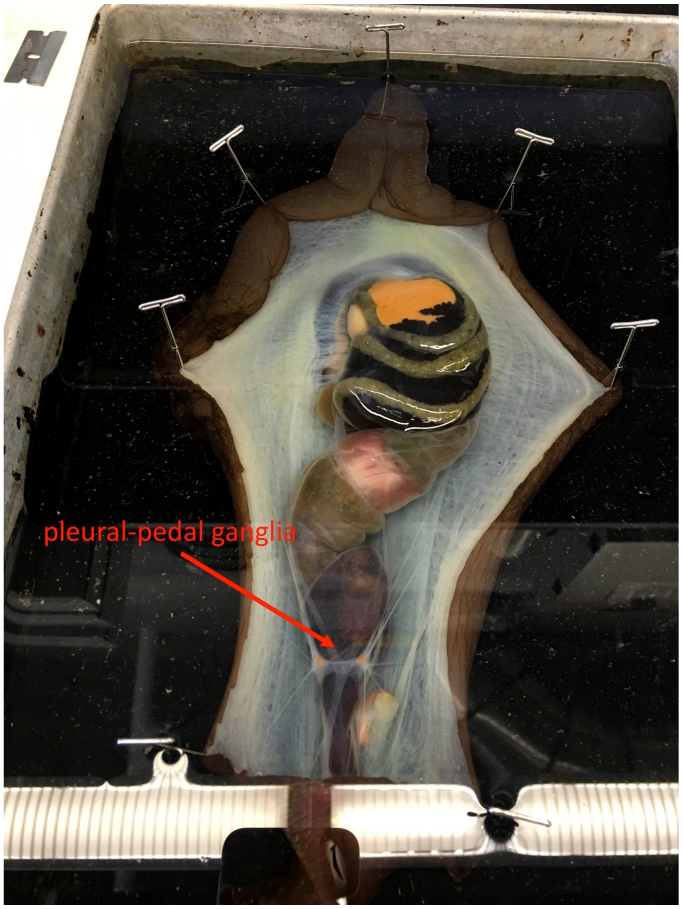

Figure 7.4: Dissected aplysia with ganglia visible

One then cuts out these ganglia and stores the in the prepared cell medium. These ganglia can be stored at 4 C for 24 hours.

Because Aplysia are invertebrate animals they can be disposed of in the trash.

7.4.8 Neuron extraction

To extract the neurons from the ganglia one needs to digest the connective tissue. This dissection is done by incubating the aplyia in the protease solution for at least 1.4 hours but no longer than 2.15 hrs at 34.5 C. The ganlia are then washed in sea water and put into culture medium in a Sylgard coated Maktek dish. THe connective tissue can then be cut with dissection scissors. Using forceps one can pull the tissue apart. Using small pins one can pin the ganglia to the Sylgard. Using the pulled pipettes one can carefully pull individual neurons from the ganglia see Figure 7.5. Using a 10 μl pipette one can transfer the cells from the dissection dish to the diamond probe. This process must be done very gently. The neurons are placed on top of the diamond and over the course of a day the neuron will adhere to the poly-l-lysine covered diamond.

7.5 Electrophysiology of neurons on diamond

With the cells plated on the diamond we can perform electrophysiology to know the cells are alive. We performed a current clamp measurement where we took an electrode and impaled a cell and put another electrode in the cell medium. By increasing the current we can cause the cell membrane voltage to above the threshold for action potentials. The

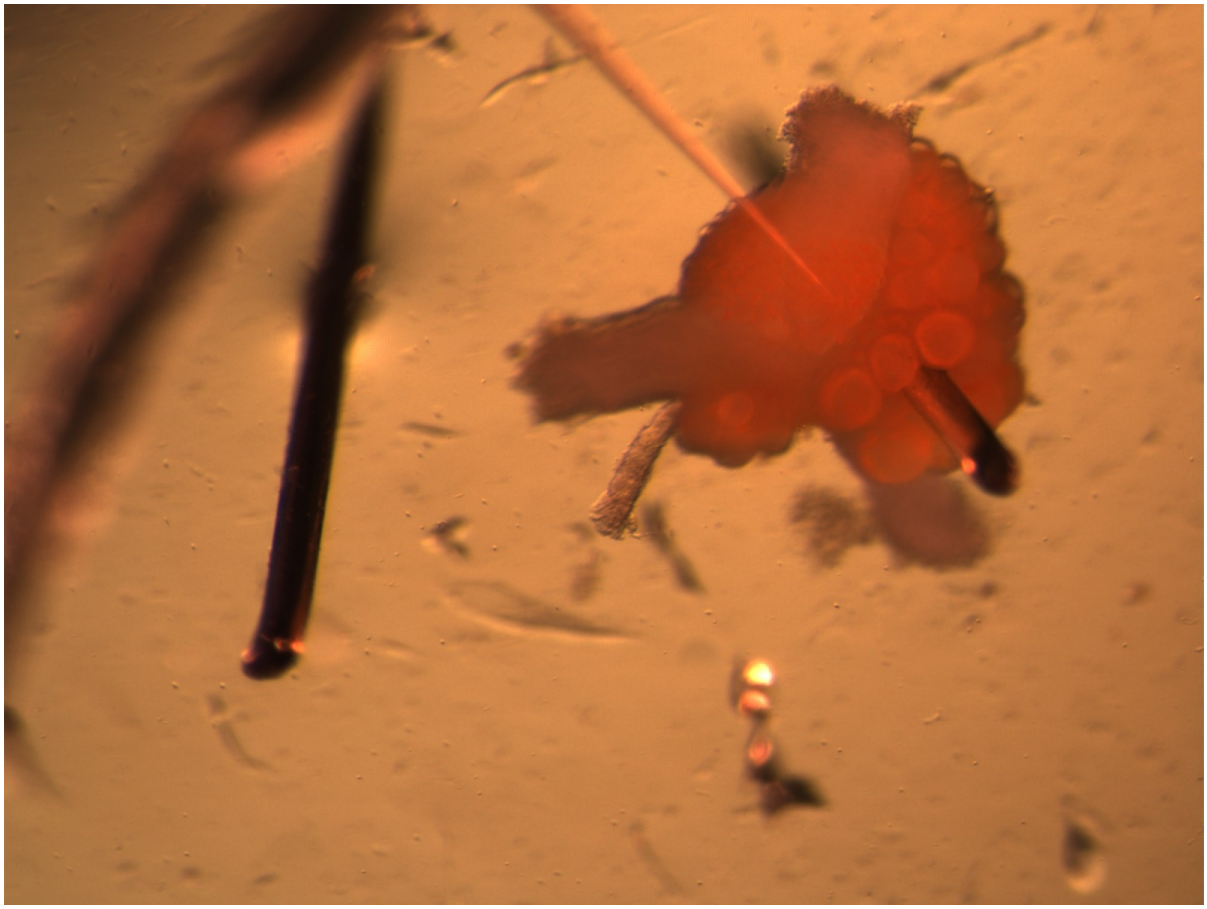

Figure 7.5: Aplysia ganglia pinned to a Sylgard dish. A small glass pipette is pulling individual neurons out of the ganlia

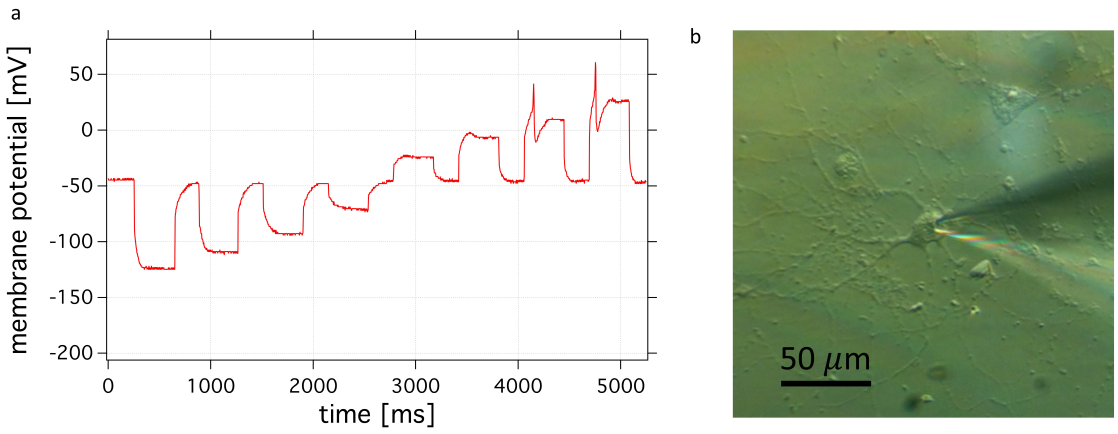

Figure 7.6: Electrophysiology experiment: A current clamp measurement taken on an *Aplysia californica* neuron. Once the voltage is brought above the threshold voltage the neuron will start to fire as seen by the spikes in voltage for the last two voltage steps.Image on the right shows a micro-pipette with silver chloride wire impaling the cell during a meausurement.

voltage will then spike. This experiment is shown in Figure 7.6. Because we can also do this experiment while shinging the laser in TIRF mode on the microscope, we demonstrated we are capable of detecting the NV center signal without hurting the neurons. The neuron only lives for about 1 hour after starting a current clamp measurement. We were able to do NV experiments before starting the current clamp measurement so we are able to know the cell can survive at least a few hours the diamond magnetometer experiment.

7.6 Magnetic field sensing of neurons

From the voltage signal detected during a current clamp experiment it is possible to simulate the magnetic field of action potential. The action potential occurs when there is a spike in the voltage due to the ion channels opening and sending an ion current down the axon. The model which I will use is from [9] and matches with more complex models [46, 132, 112]. At its core this model assumes the axon is a current carrying wire and applies Ampere's law to simulate the magnetic field.

7.6.1 Simulating the magnetic field of an action potential

Let us assume that axon is long so effects at the end of the axon can be ignored. Also, let us assume we are close enough to the neuron to ignore the back flow of ions, which cancels the magnetic field. Close enough is with-in 1 radius of the axon.

Starting withe Ampere's law for a current carrying wire, the magnitude of the magnetic field produced is

$$B_{wire} = \frac{\mu_0 I}{2\pi\rho} \tag{7.1}$$

Where I is the current flowing through the wire and ρ is the distance from the wire.

We can detect the voltage change across the axon over time during an action potential. We need to convert that information to current down the axon. Using Ohm's law the wire's current density, J, is

$$J = -\sigma\Delta\Phi(z, \rho, t) \tag{7.2}$$

Where σ is the conductivity of the wire. For a uniform wire the current, I, maybe expressed as

$$I = \pi r_a^2 J_z = \pi r_a^2 \sigma \frac{\partial \Phi(z, \rho, t)}{\partial z} \tag{7.3}$$

When conduction velocity, v_c is constant the spatial partial derivative of the potential can be related to the time derivative of the potential.

$$\frac{\partial \Phi(z, \rho, t)}{\partial t} = -v_c \frac{\partial \Phi(z, \rho, t)}{\partial z} \tag{7.4}$$

The current becomes

$$I = \frac{\pi r_a^2 \sigma}{v_c} \frac{\partial \Phi(z, \rho, t)}{\partial t} \tag{7.5}$$

The projected magnetic field is then

$$B(z, \rho, t) = \frac{\mu_0 r_a^2 \sigma}{2 v_c \rho} \frac{\partial \Phi(z, \rho, t)}{\partial t} \tag{7.6}$$

Using the parameters in Table 7.2 which are reasonable for an aplysia we can simulate the magnetic fields for neurons.

In Figure 7.7 we demonstrate the magnetic field simulated for one of the neurons we measured. Please note that the fields are nanoTesla strength on a milisecond time scale.

Parameter	Value	Unit
σ[26]	1	$\frac{1}{\Omega m}$
v_c[58]	0.75	$\frac{m}{s}$
r_a	15	μm
d	0.5	μm

Table 7.2: Aplysia neuron parameters for magnetic field simulation

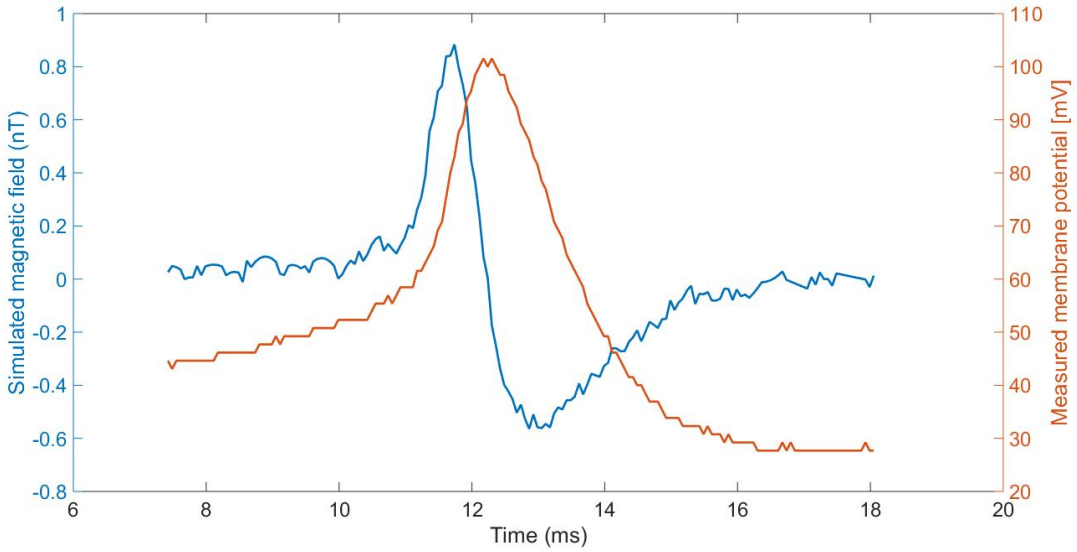

Figure 7.7: Neuron magnetic field simulation: Using data from a current clamp experiment and parameters reasonable for an *Aplysia californica* neuron the mangetic field produced 500 nm away from the neuron axon is plotted. Current clamp data is in orange and magnetic field simulation is in blue.

7.7 Future work

Although groups have been successful of detecting the magnetic field of single neurons firing with both SQUIDs and NV centers [8, 9], imaging many neurons has not been achieved. One of the challenges with our experiments is improvign the sensitivity of our magnetometer. To achieve imaging of a neuron we need a sensitivity of better than 300 nT/$\sqrt{Hz}$ in a 5x5 μm^2 sensing area. Currently, our diamond samples have sub 1

nT/$\sqrt{Hz}$ sensitivity in a 5x5 μm^2 area. Using pulsed methods with a lock-in camera and improving the sensitivity of our samples could help us achieve this goal. An outstanding challenge is combining the electro-physiology, neuron plating, and pulsed NV sensing.

Chapter 8

Outlook

Improving the sensitivity of the magnetometer is necessary for making a useful bio-compatible magnetometer. To this end we are exploring both new sensing modalities, such as pulsed ESR techniques but using a camera for detection, and improving the T_2^* of our sensors.

8.1 Improving T_2^* of NV centers

Because or NV centers are limited by the P1 spin bath it is possible to extend the coherence of the NV center by decoupling the P1 bath. Decoupling is done by applying a π pulse on the P1 centers during a Ramsey experiment or continuously driving the P1 centers during a Ramsey sequence. In Figure 8.2 one can see how we can extend the coherence for an NV center in both situations. We can extend a coherence time of 1.38 μs to 2.34 μs. The fit for the continuously driving data is not the best. The limit of this

coherence extension is the spin-echo T_2. For this sample, which has 6 ppm P1 center concentration the coherence is about 16 μs.

To further improve the sensitivity and effectiveness of P1 driving, we placed the NV center into a double quantum coherence (DQC) between the $|-1\rangle$ and $|+1\rangle$ states. By not using the $|0\rangle$ state, which is sensitive to electric fields, temperature and strain, the NV center is effectively decoupled from the effect of electric fields, temperature and strain. The coherence of the sample drops to 8 μs because the NV center is doubly sensitive to magnetic fields. By driving the P1 centers in a DQC configuration it is possible to extend coherence to 4 μs. Continuously driving the sample is similar to motional narrowing, or in this case spin-drive narrowing.

To keep improving this decoupling we are exploring pulses shaping used in other fields of quantum technologies [74]. Similar results have been presented by the Walsworth group [10].

8.2 Directions to take this research

8.2.1 Wide field imaging with NV centers

This thesis focused on ensembles and wide-field imaging of neurons but many other exciting applications can exist. Using this style of magnetometer can also be used to explore magnetic phenomena in condensced matter systems non-invasively. By taking an image magnetic field fluctuations can be correlated in space and time.

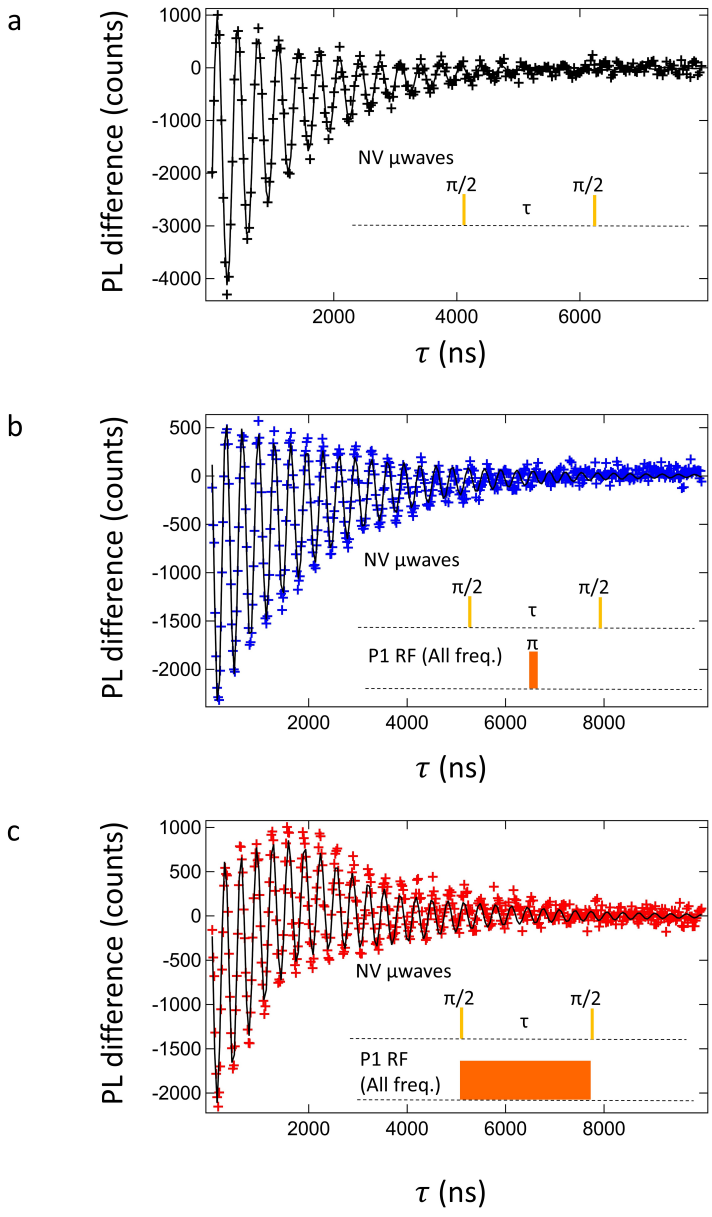

Figure 8.1: Ramsey experiments while driving P1 centers in a single quantum coherence configuration. a) A Ramsey experiment without driving the P1 centers, the coherence time is $1.38 \pm 0.03\mu$s. b) A π pulse is applied on the P1 centers half way through the measurement. The coherence time is $2.10 \pm 0.04\mu$s. c) All P1 center transitions are continuously driven. This experiment can be thought of as motionally narrowing the effect of the P1 centers. The coherence time is $2.34 \pm 0.09\mu$s.

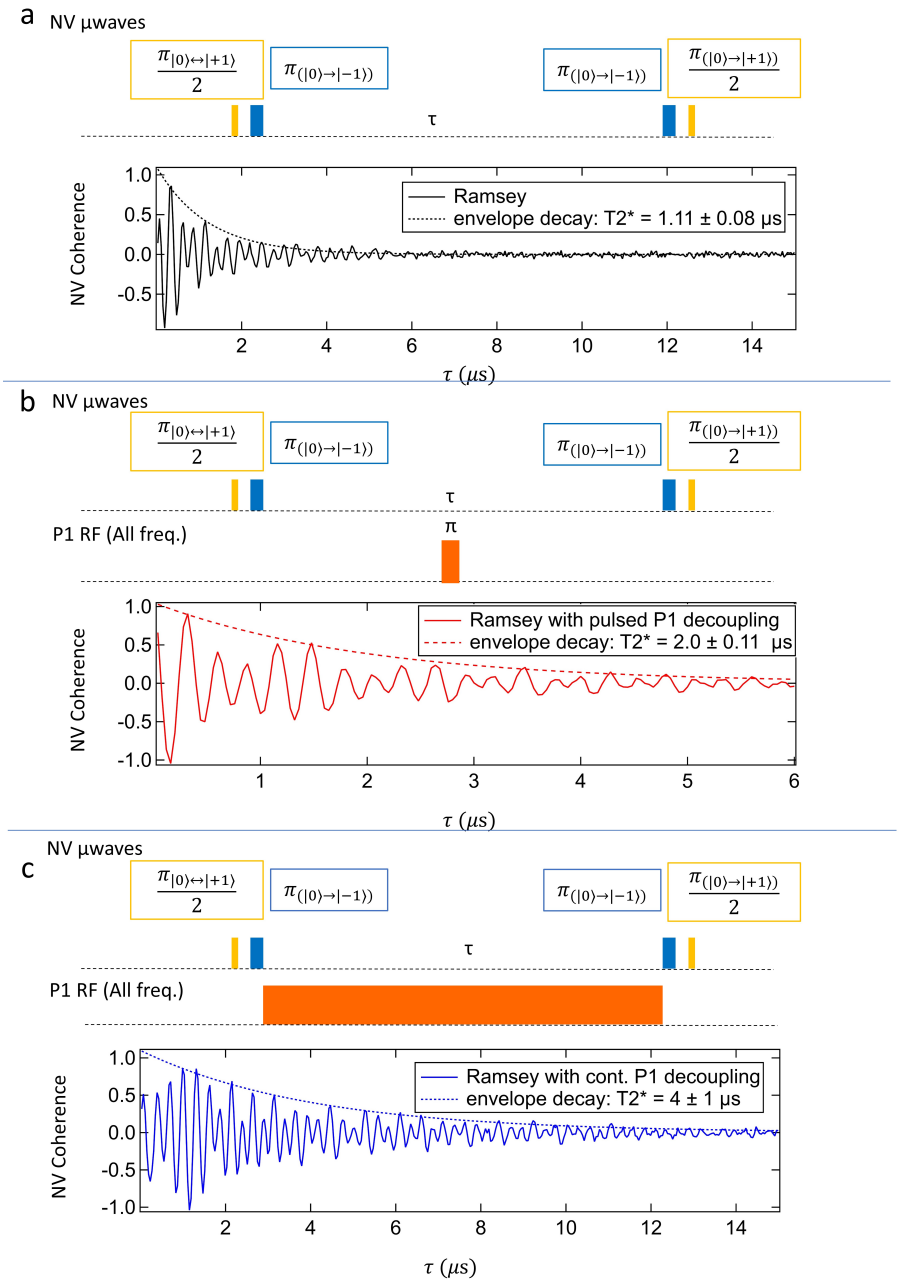

Figure 8.2: Ramsey experiments while driving P1 centers in double quantum coherence configuration. a) A Ramsey experiment without driving the P1 centers, the coherence time is $1.1 \pm 0.03\mu$s. b) A π pulse is applied on the P1 centers half way through the measurement. The coherence time is $2.0 \pm 0.11\mu$s. c) All P1 center transitions are continuously driven. The coherence time is $4 \pm 1\mu$s.

8.2.2 TEM irradiation

TEM irradiation was used to create large ensembles but TEMs are also excellent imaging tools. Exploring how to image where NV centers are placed in nano-structures could be an interesting direction.

8.2.3 Spin dynamics in spin ensembles

Understanding the fundamental physics of dense spin ensembles is an exciting direction of research. The ease tuning the density with our formation techniques could provide a new way to probe these phenomena.

Appendix A

NV center Hamiltonian calculations

A.0.1 Eigenvectors and eigenvalues under no external magnetic field

The NV center is a spin 1 system which corresponds to the following spin matrices

$$S_x = \begin{bmatrix} 0 & 1 & 0 \\ 1 & 0 & 1 \\ 0 & 1 & 0 \end{bmatrix} \quad S_y = \begin{bmatrix} 0 & -i & 0 \\ -i & 0 & i \\ 0 & i & 0 \end{bmatrix} \quad S_z = \begin{bmatrix} 1 & 0 & 0 \\ 0 & 0 & 0 \\ 0 & 0 & -1 \end{bmatrix} \tag{A.1}$$

The basis for the NV center will be chosen along the S_z axis such that

$$|+1\rangle = \begin{pmatrix} 1 \\ 0 \\ 0 \end{pmatrix} \quad |0\rangle = \begin{pmatrix} 0 \\ 1 \\ 0 \end{pmatrix} \quad |-1\rangle = \begin{pmatrix} 0 \\ 0 \\ 1 \end{pmatrix} \tag{A.2}$$

The ground state Hamiltonian of the NV, ignoring hyperfine and quadrapole interactions, maybe written as [32]

$$\mathcal{H}_{gs} = \mathcal{D}[S_z^2 - S(S+1)/3] \tag{A.3}$$

This may be rewritten as

$$\mathcal{H}_{gs} = \begin{bmatrix} D & 0 & 0 \\ 0 & 0 & 0 \\ 0 & 0 & D \end{bmatrix} - 2/3D\mathbb{1} \tag{A.4}$$

First solving $\mathcal{H}_{gs}$ for its eigenvalues

$$0 = \begin{vmatrix} D-\lambda & 0 & 0 \\ 0 & 0 & 0 \\ 0 & 0 & D-\lambda \end{vmatrix} = (D-\lambda)(-\lambda)(D-\lambda) \tag{A.5}$$

This equation has the solutions

$$\lambda_{x,y} = D \quad \lambda_z = 0 \tag{A.6}$$

Adjusting for the energy shift in the Hamiltonian leads to the eigenvalues for the NV center ground state.

$$\lambda_{x,y} = -1/3D \quad \lambda_z = -2/3D \tag{A.7}$$

The next step is to find the eigenvectors, which can obtained using the fact that the Schrödinger equation is diagonalizable.

$$U^{-1}\mathcal{H}_{gs}U = \Lambda_{\mathcal{H}_{gs}} \tag{A.8}$$

Where the column vectors in U is the eigenbasis for $\mathcal{H}_{gs}$ and $\Lambda_{\mathcal{H}_{gs}}$ is a diagonal matrix

with the eigenvalues of $\mathcal{H}_{gs}$ for its diagonal elements.

$$U = \begin{bmatrix} T_{+1X} & T_{+1Y} & T_{+1Z} \\ T_{0X} & T_{0Y} & T_{0Z} \\ T_{-1X} & T_{-1Y} & T_{-1Z} \end{bmatrix} \tag{A.9}$$

$$U^{-1} = \begin{bmatrix} T^*_{+1X} & T^*_{0X} & T^*_{-1X} \\ T^*_{+1Y} & T^*_{0Y} & T^*_{-1Y} \\ T^*_{+1Z} & T^*_{0Z} & T^*_{-1Z} \end{bmatrix} \tag{A.10}$$

$$\Lambda_{\mathcal{H}_{gs}} = \begin{bmatrix} D & 0 & 0 \\ 0 & D & 0 \\ 0 & 0 & 0 \end{bmatrix} \tag{A.11}$$

The solution of A.8 is

$$U = \begin{bmatrix} 1 & 0 & 0 \\ 0 & 0 & 1 \\ 0 & 1 & 0 \end{bmatrix} \tag{A.12}$$

This equation leads to the eigenvectors to be exactly the $|+1\rangle$, $|0\rangle$, $|-1\rangle$ states that were established for the system. This result makes sense as no mixing terms were included in the Hamiltonian.

Bibliography

[1] CNSI Seki PECVD. https://www.cnsi.ucsb.edu/resources/facilities/equipment/seki-diamond-cvd.

[2] A Abragam. Principles of nuclear magnetism (international series of monographs on physics), 1961.

[3] Victor Marcel Acosta. *Optical magnetometry with nitrogen-vacancy centers in diamond*. PhD thesis, University of California, Berkeley, 2011.

[4] S. Agnello, R. Boscaino, M. Cannas, and F. M. Gelardi. Instantaneous diffusion effect on spin-echo decay: Experimental investigation by spectral selective excitation. *Phys. Rev. B*, 64:174423, Oct 2001.

[5] WJ Baker, K Ambal, DP Waters, Rachel Baarda, Hiroki Morishita, Kipp van Schooten, Dane R McCamey, John M Lupton, and Christoph Boehme. Robust absolute magnetometry with organic thin-film devices. *Nature communications*, 3:898, 2012.

[6] MV Balabas, D Budker, J Kitching, PDD Schwindt, and JE Stalnaker. Magnetometry with millimeter-scale antirelaxation-coated alkali-metal vapor cells. *JOSA B*, 23(6):1001–1006, 2006.

[7] Gopalakrishnan Balasubramanian, Philipp Neumann, Daniel Twitchen, Matthew Markham, Roman Kolesov, Norikazu Mizuochi, Junichi Isoya, Jocelyn Achard, Johannes Beck, Julia Tissler, et al. Ultralong spin coherence time in isotopically engineered diamond. *Nature materials*, 8(5):383, 2009.

[8] JP Barach, JA Freeman, and JP Wikswo Jr. Experiments on the magnetic field of nerve action potentials. *Journal of Applied Physics*, 51(8):4532–4538, 1980.

[9] John F Barry, Matthew J Turner, Jennifer M Schloss, David R Glenn, Yuyu Song, Mikhail D Lukin, Hongkun Park, and Ronald L Walsworth. Optical magnetic

detection of single-neuron action potentials using quantum defects in diamond. *Proceedings of the National Academy of Sciences*, 113(49):14133–14138, 2016.

[10] Erik Bauch, Connor A Hart, Jennifer M Schloss, Matthew J Turner, John F Barry, Pauli Kehayias, and Ronald L Walsworth. Ultralong dephasing times in solid-state spin ensembles via quantum control. *arXiv preprint arXiv:1801.03793*, 2018.

[11] Richard Blakemore. Magnetotactic bacteria. *Science*, 190(4212):377–379, 1975.

[12] Chris Boesch. Nobel prizes for nuclear magnetic resonance: 2003 and historical perspectives. *Journal of magnetic resonance imaging*, 20(2):177–179, 2004.

[13] JC Bourgoin and B Massarani. Threshold energy for atomic displacement in diamond. *Physical Review B*, 14(8):3690, 1976.

[14] Andreas Brenneis, Louis Gaudreau, Max Seifert, Helmut Karl, Martin S Brandt, Hans Huebl, Jose A Garrido, Frank HL Koppens, and Alexander W Holleitner. Ultrafast electronic readout of diamond nitrogen–vacancy centres coupled to graphene. *Nature nanotechnology*, 10(2):135, 2015.

[15] Robert W Brown, E Mark Haacke, Y-C Norman Cheng, Michael R Thompson, and Ramesh Venkatesan. *Magnetic resonance imaging: physical principles and sequence design*. John Wiley & Sons, 2014.

[16] Dmitry Budker and Michael Romalis. Optical magnetometry. *Nature Physics*, 3(4):227, 2007.

[17] B Campbell and A Mainwood. Radiation damage of diamond by electron and gamma irradiation. *PHYSICA STATUS SOLIDI A APPLIED RESEARCH*, 181(1):99–108, 2000.

[18] Neil A Campbell, Lisa A Urry, Michael L Cain, Steven A Wasserman, and Peter V Minorsky. *Biology: a global approach*. Pearson Higher Ed, 2017.

[19] AM Chang, HD Hallen, L Harriott, HF Hess, HL Kao, J Kwo, RE Miller, R Wolfe, J Van der Ziel, and TY Chang. Scanning hall probe microscopy. *Applied physics letters*, 61(16):1974–1976, 1992.

[20] Sandrine Chemla and Frédéric Chavane. Voltage-sensitive dye imaging: technique review and models. *Journal of Physiology-Paris*, 104(1-2):40–50, 2010.

[21] L. Childress, M. V. Gurudev Dutt, J. M. Taylor, A. S. Zibrov, F. Jelezko, J. Wrachtrup, P. R. Hemmer, and M. D. Lukin. Coherent Dynamics of Coupled Electron and Nuclear Spin Qubits in Diamond. *Science*, 314(5797):281–285, October 2006.

[22] Lilian Isabel Childress. *Coherent manipulation of single quantum systems in the solid state*. PhD thesis, Harvard University, 2007.

[23] Joonhee Choi, Soonwon Choi, Georg Kucsko, Peter C Maurer, Brendan J Shields, Hitoshi Sumiya, Shinobu Onoda, Junichi Isoya, Eugene Demler, Fedor Jelezko, et al. Depolarization dynamics in a strongly interacting solid-state spin ensemble. *Physical review letters*, 118(9):093601, 2017.

[24] Soonwon Choi, Joonhee Choi, Renate Landig, Georg Kucsko, Hengyun Zhou, Junichi Isoya, Fedor Jelezko, Shinobu Onoda, Hitoshi Sumiya, Vedika Khemani, et al. Observation of discrete time-crystalline order in a disordered dipolar many-body system. *Nature*, 543(7644):221, 2017.

[25] CD Clark, PJ Kemmey, and EWJ Mitchell. Optical and electrical effects of radiation damage in diamond. *Discussions of the Faraday Society*, 31:96–106, 1961.

[26] John Clark and Robert Plonsey. A mathematical evaluation of the core conductor model. *Biophysical journal*, 6(1):95–112, 1966.

[27] A Cox, ME Newton, and JM Baker. 13c, 14n and 15n endor measurements on the single substitutional nitrogen centre (p1) in diamond. *Journal of Physics: Condensed Matter*, 6(2):551, 1994.

[28] Gordon Davies, Simon C Lawson, Alan T Collins, Alison Mainwood, and Sarah J Sharp. Vacancy-related centers in diamond. *Physical Review B*, 46(20):13157, 1992.

[29] Gijs De Lange, Toeno Van Der Sar, Machiel Blok, Zhi-Hui Wang, Viatcheslav Dobrovitski, and Ronald Hanson. Controlling the quantum dynamics of a mesoscopic spin bath in diamond. *Scientific reports*, 2:382, 2012.

[30] Siddharth Dhomkar, Jacob Henshaw, Harishankar Jayakumar, and Carlos A Meriles. Long-term data storage in diamond. *Science advances*, 2(10):e1600911, 2016.

[31] V. V. Dobrovitski, A. E. Feiguin, D. D. Awschalom, and R. Hanson. Decoherence dynamics of a single spin versus spin ensemble. *Phys. Rev. B*, 77:245212, Jun 2008.

[32] Marcus W Doherty, Neil B Manson, Paul Delaney, Fedor Jelezko, Joerg Wrachtrup, and Lloyd CL Hollenberg. The nitrogen-vacancy colour centre in diamond. *Physics Reports*, 528(1):1–45, 2013.

[33] A Dréau, M Lesik, L Rondin, P Spinicelli, O Arcizet, J-F Roch, and V Jacques. Avoiding power broadening in optically detected magnetic resonance of single nv defects for enhanced dc magnetic field sensitivity. *Physical Review B*, 84(19):195204, 2011.

[34] Dominique Drouin, Alexandre Réal Couture, Dany Joly, Xavier Tastet, Vincent Aimez, and Raynald Gauvin. Casino v2. 42—a fast and easy-to-use modeling tool for scanning electron microscopy and microanalysis users. *Scanning*, 29(3):92–101, 2007.

[35] Gareth R Eaton, Sandra S Eaton, David P Barr, and Ralph T Weber. *Quantitative EPR*. Springer Science & Business Media, 2010. pg. 4.

[36] Gareth R Eaton, Sandra S Eaton, Richard W Quine, Deborah Mitchell, Velavan Kathirvelu, and Ralph T Weber. A signal-to-noise standard for pulsed epr. *Journal of Magnetic Resonance*, 205(1):109–113, 2010.

[37] RL Fagaly. Superconducting quantum interference device instruments and applications. *Review of scientific instruments*, 77(10):101101, 2006.

[38] G. D. Fuchs, V. V. Dobrovitski, R. Hanson, A. Batra, C. D. Weis, T. Schenkel, and D. D. Awschalom. Excited-state spectroscopy using single spin manipulation in diamond. *Phys. Rev. Lett.*, 101:117601, Sep 2008.

[39] C Gemperle, G Aebli, A Schweiger, and RR Ernst. Phase cycling in pulse epr. *Journal of Magnetic Resonance (1969)*, 88(2):241–256, 1990.

[40] Christopher Gerry, Peter Knight, and Peter L Knight. *Introductory Quantum Optics*. Cambridge university press, 2005.

[41] David L Glanzman. Habituation in aplysia: the cheshire cat of neurobiology. *Neurobiology of learning and memory*, 92(2):147–154, 2009.

[42] David R Glenn, Dominik B Bucher, Junghyun Lee, Mikhail D Lukin, Hongkun Park, and Ronald L Walsworth. High-resolution magnetic resonance spectroscopy using a solid-state spin sensor. *Nature*, 555(7696):351, 2018.

[43] David J Griffiths. Electrodynamics. *Introduction to Electrodynamics, 3rd ed., Prentice Hall, Upper Saddle River, New Jersey*, pages 301–306, 1999.

[44] MS Grinolds, P Maletinsky, S Hong, MD Lukin, RL Walsworth, and A Yacoby. Quantum control of proximal spins using nanoscale magnetic resonance imaging. *Nature Physics*, 7(9):687, 2011.

[45] A Gruber, A Dräbenstedt, C Tietz, L Fleury, J Wrachtrup, and C Von Borczyskowski. Scanning confocal optical microscopy and magnetic resonance on single defect centers. *Science*, 276(5321):2012–2014, 1997.

[46] LT Hall, GCG Beart, EA Thomas, DA Simpson, LP McGuinness, JH Cole, JH Manton, RE Scholten, Fedor Jelezko, Jörg Wrachtrup, et al. High spatial and temporal resolution wide-field imaging of neuron activity using quantum nv-diamond. *Scientific reports*, 2:401, 2012.

[47] Kazushi Hayashi, Sadanori Yamanaka, Hideyuki Watanabe, Takashi Sekiguchi, Hideyo Okushi, and Koji Kajimura. Atomic force microscopy study of atomically flat (001) diamond surfaces treated with hydrogen plasma. *Applied surface science*, 125(1):120–124, 1998.

[48] Xing-Fei He, Neil B Manson, and Peter TH Fisk. Paramagnetic resonance of photoexcited n-v defects in diamond. ii. hyperfine interaction with the n 14 nucleus. *Physical Review B*, 47(14):8816, 1993.

[49] Alan L Hodgkin and Andrew F Huxley. A quantitative description of membrane current and its application to conduction and excitation in nerve. *The Journal of physiology*, 117(4):500–544, 1952.

[50] Allan L Hodgkin and Andrew F Huxley. The dual effect of membrane potential on sodium conductance in the giant axon of loligo. *The Journal of physiology*, 116(4):497–506, 1952.

[51] Ryota Homma, Bradley J Baker, Lei Jin, Olga Garaschuk, Arthur Konnerth, Lawrence B Cohen, Chun X Bleau, Marco Canepari, Maja Djurisic, and Dejan Zecevic. Wide-field and two-photon imaging of brain activity with voltage and calcium-sensitive dyes. In *Dynamic Brain Imaging*, pages 43–79. Springer, 2009.

[52] Z Huang, W-D Li, C Santori, VM Acosta, A Faraon, T Ishikawa, W Wu, D Winston, RS Williams, and RG Beausoleil. Diamond nitrogen-vacancy centers created by scanning focused helium ion beam and annealing. *Applied Physics Letters*, 103(8):081906, 2013.

[53] Michael Ilg, Christoph D Weis, Julian Schwartz, Arun Persaud, Qing Ji, Cheuk Chi Lo, Jeffrey Bokor, Alex Hegyi, Elshad Guliyev, Ivo W Rangelow, et al. Improved single ion implantation with scanning probe alignment. *Journal of Vacuum Science & Technology B, Nanotechnology and Microelectronics: Materials, Processing, Measurement, and Phenomena*, 30(6):06FD04, 2012.

[54] Arroyo Instruments. Arroyo6300 combo source users manual. https://www.arroyoinstruments.com/manuals/Arroyo6300ComboSourceUsersManual.pdf.

[55] Gunnar Jeschke, Grazyna Panek, Adelheid Godt, Alexander Bender, and Harald Paulsen. Data analysis procedures for pulse eldor measurements of broad distance distributions. *Applied Magnetic Resonance*, 26(1-2):223, 2004.

[56] Edwin Kim, Victor M Acosta, Erik Bauch, Dmitry Budker, and Philip R Hemmer. Electron spin resonance shift and linewidth broadening of nitrogen-vacancy centers in diamond as a function of electron irradiation dose. *Applied physics letters*, 101(8):082410, 2012.

[57] John R Kirtley, Lisa Paulius, Aaron J Rosenberg, Johanna C Palmstrom, Connor M Holland, Eric M Spanton, Daniel Schiessl, Colin L Jermain, Jonathan Gibbons, Y-K-K Fung, et al. Scanning squid susceptometers with sub-micron spatial resolution. *Review of Scientific Instruments*, 87(9):093702, 2016.

[58] H Koike. The extensibility of aplysia nerve and the determination of true axon length. *The Journal of physiology*, 390(1):469–487, 1987.

[59] J Koike, DM Parkin, and TE Mitchell. Displacement threshold energy for type iia diamond. *Applied physics letters*, 60(12):1450–1452, 1992.

[60] Satoshi Koizumi, Christoph Nebel, and Milos Nesladek. *Physics and applications of CVD diamond*. John Wiley & Sons, 2008.

[61] IK Kominis, TW Kornack, JC Allred, and MV Romalis. A subfemtotesla multichannel atomic magnetometer. *Nature*, 422(6932):596, 2003.

[62] Georg Kucsko, Soonwon Choi, Joonhee Choi, Peter C Maurer, Hengyun Zhou, Renate Landig, Hitoshi Sumiya, Shinobu Onoda, Junich Isoya, Fedor Jelezko, et al. Critical thermalization of a disordered dipolar spin system in diamond. *arXiv preprint arXiv:1609.08216*, 2016.

[63] Abdelghani Laraoui, Florian Dolde, Christian Burk, Friedemann Reinhard, Jörg Wrachtrup, and Carlos A Meriles. High-resolution correlation spectroscopy of 13 c spins near a nitrogen-vacancy centre in diamond. *Nature Communications*, 4:1651, 2013.

[64] C.L. Lee, E. Gu, M.D. Dawson, I. Friel, and G.A. Scarsbrook. Etching and microoptics fabrication in diamond using chlorine-based inductively-coupled plasma. *Diamond and Related Materials*, 17(7):1292 – 1296, 2008. Proceedings of Diamond 2007, the 18th European Conference on Diamond, Diamond-Like Materials, Carbon Nanotubes, Nitrides and Silicon Carbide.

[65] Kenneth W Lee, Donghun Lee, Preeti Ovartchaiyapong, Joaquin Minguzzi, Jero R Maze, and Ania C Bleszynski Jayich. Strain coupling of a mechanical resonator to a single quantum emitter in diamond. *Physical Review Applied*, 6(3):034005, 2016.

[66] Kenneth William Lee III. *Coherent Dynamics of a Hybrid Quantum Spin-Mechanical Oscillator System*. PhD thesis, University of California, Santa Barbara, 2017.

[67] Margarita Lesik, Piernicola Spinicelli, Sébastien Pezzagna, Patrick Happel, Vincent Jacques, Olivier Salord, Bernard Rasser, Anne Delobbe, Pierre Sudraud, Alexandre Tallaire, et al. Maskless and targeted creation of arrays of colour centres in diamond using focused ion beam technology. *physica status solidi (a)*, 210(10):2055–2059, 2013.

[68] Z. Z. Liang, X. Jia, H. A. Ma, C. Y. Zang, P. W. Zhu, Q. F. Guan, and H. Kanda. Synthesis of HPHT diamond containing high concentrations of nitrogen impurities using NaN3 as dopant in metal-carbon system. *Diamond and Related Materials*, 14(11):1932–1935, November 2005.

[69] J.H.N. Loubser and J.A. van Wyk. Electron spin resonance in the study of diamond. *Reports on Progress in Physics*, 41(8):1201, 1978.

[70] William Lowrie. *Fundamentals of Geophysics*, page 281. Cambridge university press, 2007.

[71] Patrick Maletinsky, Sungkun Hong, Michael Sean Grinolds, Birgit Hausmann, Mikhail D Lukin, Ronald L Walsworth, Marko Loncar, and Amir Yacoby. A robust scanning diamond sensor for nanoscale imaging with single nitrogen-vacancy centres. *Nature nanotechnology*, 7(5):320, 2012.

[72] HJ Mamin, M Kim, MH Sherwood, CT Rettner, K Ohno, DD Awschalom, and D Rugar. Nanoscale nuclear magnetic resonance with a nitrogen-vacancy spin sensor. *Science*, 339(6119):557–560, 2013.

[73] J Martin, R Wannemacher, J Teichert, L Bischoff, and B Köhler. Generation and detection of fluorescent color centers in diamond with submicron resolution. *Applied physics letters*, 75(20):3096–3098, 1999.

[74] John M Martinis and Michael R Geller. Fast adiabatic qubit gates using only σ z control. *Physical Review A*, 90(2):022307, 2014.

[75] Stuart McLaughlin. The electrostatic properties of membranes. *Annual review of biophysics and biophysical chemistry*, 18(1):113–136, 1989.

[76] Claire A McLellan, Bryan A Myers, Stephan Kraemer, Kenichi Ohno, David D Awschalom, and Ania C Bleszynski Jayich. Patterned formation of highly coherent nitrogen-vacancy centers using a focused electron irradiation technique. *Nano letters*, 16(4):2450–2454, 2016.

[77] J Meijer, B Burchard, M Domhan, C Wittmann, Torsten Gaebel, I Popa, F Jelezko, and J Wrachtrup. Generation of single color centers by focused nitrogen implantation. *Applied Physics Letters*, 87(26):261909, 2005.

[78] Koichi Momma and Fujio Izumi. ıt VESTA3 for three-dimensional visualization of crystal, volumetric and morphology data. *Journal of Applied Crystallography*, 44(6):1272–1276, December 2011.

[79] Leonid L Moroz. Aplysia. *Current biology: CB*, 21(2):R60, 2011.

[80] Bryan Andrew Myers. *Quantum decoherence of near-surface nitrogen-vacancy centers in diamond and implications for nanoscale imaging*. PhD thesis, University of California, Santa Barbara, 2016.

[81] Nature news article. Big diamonds grown faster. "http://www.nature.com/news/2002/020930/full/news020923-17.html", 2002.

[82] Katja C Nowack, Eric M Spanton, Matthias Baenninger, Markus König, John R Kirtley, Beena Kalisky, Christopher Ames, Philipp Leubner, Christoph Brüne, Hartmut Buhmann, et al. Imaging currents in hgte quantum wells in the quantum spin hall regime. *Nature materials*, 12(9):787, 2013.

[83] David Ogden and PETER STANFIELD. Patch clamp techniques for single channel and whole-cell recording. In *Microelectrode techniques: the Plymouth workshop handbook*, volume 2, 1994.

[84] Kenichi Ohno. *Nanometer-scale engineering of shallow spins in diamond*. University of California, Santa Barbara, Santa Barbara, Calif.], 2014.

[85] Kenichi Ohno, F Joseph Heremans, Lee C Bassett, Bryan A Myers, David M Toyli, Ania C Bleszynski Jayich, Christopher J Palmstrøm, and David D Awschalom. Engineering shallow spins in diamond with nitrogen delta-doping. *Applied Physics Letters*, 101(8):082413, 2012.

[86] Kenichi Ohno, F Joseph Heremans, Charles F de las Casas, Bryan A Myers, Benjamín J Alemán, Ania C Bleszynski Jayich, and David D Awschalom. Three-dimensional localization of spins in diamond using 12c implantation. *Applied Physics Letters*, 105(5):052406, 2014.

[87] Preeti Ovartchaiyapong. *Strain-coupled hybrid devices based on single-crystal diamond mechanical resonators and nitrogen-vacancy center qubits*. PhD thesis, University of California, Santa Barbara, 2016.

[88] Matthias Pannier, Stephan Veit, Adelheid Godt, Gunnar Jeschke, and Hans Wolfgang Spiess. Dead-time free measurement of dipole–dipole interactions between electron spins. *Journal of Magnetic Resonance*, 142(2):331–340, 2000.

[89] Fernando Patolsky, Brian P Timko, Guihua Yu, Ying Fang, Andrew B Greytak, Gengfeng Zheng, and Charles M Lieber. Detection, stimulation, and inhibition of neuronal signals with high-density nanowire transistor arrays. *Science*, 313(5790):1100–1104, 2006.

[90] Matthew Pelliccione, Alec Jenkins, Preeti Ovartchaiyapong, Christopher Reetz, Eve Emmanouilidou, Ni Ni, and Ania C Bleszynski Jayich. Scanned probe imaging of nanoscale magnetism at cryogenic temperatures with a single-spin quantum sensor. *Nature nanotechnology*, 11(8):700, 2016.

[91] Linh My Pham. *Magnetic field sensing with nitrogen-vacancy color centers in diamond*. PhD thesis, Harvard University, 2013.

[92] ZQ Qiu and Samuel D Bader. Surface magneto-optic kerr effect. *Review of Scientific Instruments*, 71(3):1243–1255, 2000.

[93] Atta-ur Rahman. *Solving problems with NMR spectroscopy*. Elsevier Academic Press, United Kingdom : San Diego, CA, second edition. edition, 2016.

[94] Jeronimo Maze Rios. *Quantum manipulation of nitrogen-vacancy centers in diamond: from basic properties to applications*. PhD thesis, Harvard University, 2010.

[95] Y Romach, C Müller, T Unden, LJ Rogers, T Isoda, KM Itoh, M Markham, A Stacey, J Meijer, S Pezzagna, et al. Spectroscopy of surface-induced noise using shallow spins in diamond. *Physical review letters*, 114(1):017601, 2015.

[96] M Romanelli and L Kevan. Evaluation and interpretation of electron spin-echo decay part i: Rigid samples. *Concepts in Magnetic Resonance: An Educational Journal*, 9(6):403–430, 1997.

[97] Emma L Rosenfeld, Linh M Pham, Mikhail D Lukin, and Ronald L Walsworth. Sensing coherent dynamics of electronic spin clusters in solids. *arXiv preprint arXiv:1801.00198*, 2017.

[98] T Rosskopf, A Dussaux, K Ohashi, M Loretz, Romana Schirhagl, H Watanabe, S Shikata, KM Itoh, and CL Degen. Investigation of surface magnetic noise by shallow spins in diamond. *Physical review letters*, 112(14):147602, 2014.

[99] D Rugar, HJ Mamin, P Guethner, SE Lambert, JE Stern, I McFadyen, and T Yogi. Magnetic force microscopy: General principles and application to longitudinal recording media. *Journal of Applied Physics*, 68(3):1169–1183, 1990.

[100] KM Salikhov, S.A. Dzuba, and A. M. Raitsimring. The theory of electron spin-echo signal decay resulting from dipole-dipole interactions between paramagnetic centers in solids. *Journal of Magnetic Resonance (1969)*, 42(2):255–276, 1981.

[101] Stephen M Schuetze. The discovery of the action potential. *Trends in Neurosciences*, 6:164–168, 1983.

[102] Arthur Schweiger and Gunnar Jeschke. *Principles of pulse electron paramagnetic resonance*. Oxford University Press on Demand, 2001.

[103] Brendan J Shields, Quirin P Unterreithmeier, Nathalie P de Leon, H Park, and Mikhail D Lukin. Efficient readout of a single spin state in diamond via spin-to-charge conversion. *Physical Review Letters*, 114(13):136402, 2015.

[104] David A Simpson, Robert G Ryan, Liam T Hall, Evgeniy Panchenko, Simon C Drew, Steven Petrou, Paul S Donnelly, Paul Mulvaney, and Lloyd CL Hollenberg. Electron paramagnetic resonance microscopy using spins in diamond under ambient conditions. *Nature communications*, 8(1):458, 2017.

[105] Charles P Slichter. *Principles of magnetic resonance*, volume 1. Springer Science & Business Media, 2013.

[106] RE Stallcup II and José M Pérez. Scanning tunneling microscopy studies of temperature-dependent etching of diamond (100) by atomic hydrogen. *Physical review letters*, 86(15):3368, 2001.

[107] Tobias Staudacher, Fazhan Shi, S Pezzagna, Jan Meijer, Jiangfeng Du, Carlos A Meriles, Friedemann Reinhard, and Joerg Wrachtrup. Nuclear magnetic resonance spectroscopy on a (5-nanometer) 3 sample volume. *Science*, 339(6119):561–563, 2013.

[108] Viktor Stepanov and Susumu Takahashi. Determination of nitrogen spin concentration in diamond using double electron-electron resonance. *Physical Review B*, 94(2):024421, 2016.

[109] S Stoll and B Kasumaj. Phase cycling in electron spin echo envelope modulation. *Applied Magnetic Resonance*, 35(1):15–32, 2008.

[110] Stefan Stoll and Arthur Schweiger. Easyspin, a comprehensive software package for spectral simulation and analysis in epr. *Journal of magnetic resonance*, 178(1):42–55, 2006.

[111] AM Stoneham. *Theory of Defects in Solids: Eletronic Structure of Defects in Insultors and Semiconductors*. Clarendon Press, 1975.

[112] KR Swinney and JP Wikswo Jr. A calculation of the magnetic field of a nerve action potential. *Biophysical journal*, 32(2):719–731, 1980.

[113] Claudia E Tait and Stefan Stoll. Coherent pump pulses in double electron electron resonance spectroscopy. *Physical Chemistry Chemical Physics*, 18(27):18470–18485, 2016.

[114] Susumu Takahashi, Ronald Hanson, Johan van Tol, Mark S. Sherwin, and David D. Awschalom. Quenching Spin Decoherence in Diamond through Spin Bath Polarization. *Physical Review Letters*, 101(4):047601, July 2008.

[115] J-P Tetienne, T Hingant, J-V Kim, L Herrera Diez, J-P Adam, K Garcia, J-F Roch, S Rohart, A Thiaville, D Ravelosona, et al. Nanoscale imaging and control of domain-wall hopping with a nitrogen-vacancy center microscope. *Science*, 344(6190):1366–1369, 2014.

[116] Jean-Philippe Tetienne, Nikolai Dontschuk, David A Broadway, Alastair Stacey, David A Simpson, and Lloyd CL Hollenberg. Quantum imaging of current flow in graphene. *Science Advances*, 3(4):e1602429, 2017.

[117] JP Tetienne, L Rondin, P Spinicelli, M Chipaux, T Debuisschert, JF Roch, and V Jacques. Magnetic-field-dependent photodynamics of single nv defects in diamond: an application to qualitative all-optical magnetic imaging. *New Journal of Physics*, 14(10):103033, 2012.

[118] Lucas Thiel, Dominik Rohner, Marc Ganzhorn, Patrick Appel, Elke Neu, B Müller, R Kleiner, D Koelle, and P Maletinsky. Quantitative nanoscale vortex imaging using a cryogenic quantum magnetometer. *Nature nanotechnology*, 11(8):677, 2016.

[119] Thorlabs. TCLDM9 manual. https://www.thorlabs.com/drawings/c5fab06f3c2e0aba-C4D6E2C7-F18A-5181-0AA99DD30821BA73/TCLDM9-Manual.pdf, June 2015.

[120] Emre Togan. *Optical Control of Individual Nitrogen-Vacancy Centers in Diamond*. PhD thesis, Harvard University, 2013.

[121] Emre Togan, Yiwen Chu, AS Trifonov, Liang Jiang, Jeronimo Maze, Lilian Childress, MV Gurudev Dutt, Anders Søndberg Sørensen, PR Hemmer, Alexander S Zibrov, et al. Quantum entanglement between an optical photon and a solid-state spin qubit. *Nature*, 466(7307):730, 2010.

[122] P Török, P Varga, Z Laczik, and GR Booker. Electromagnetic diffraction of light focused through a planar interface between materials of mismatched refractive indices: an integral representation. *JOSA A*, 12(2):325–332, 1995.

[123] David M Toyli, Christoph D Weis, Gregory D Fuchs, Thomas Schenkel, and David D Awschalom. Chip-scale nanofabrication of single spins and spin arrays in diamond. *Nano letters*, 10(8):3168–3172, 2010.

[124] Jeffrey Y Tsao. *Materials fundamentals of molecular beam epitaxy*. Academic Press, 2012.

[125] Alexei M Tyryshkin, Shinichi Tojo, John JL Morton, Helge Riemann, Nikolai V Abrosimov, Peter Becker, Hans-Joachim Pohl, Thomas Schenkel, Michael LW Thewalt, Kohei M Itoh, et al. Electron spin coherence exceeding seconds in high-purity silicon. *Nature materials*, 11(2):143, 2012.

[126] Eric van Oort and Max Glasbeek. Cross-relaxation dynamics of optically excited n-v centers in diamond. *Phys. Rev. B*, 40:6509–6517, Oct 1989.

[127] Eric Van Oort and Max Glasbeek. Optically detected low field electron spin echo envelope modulations of fluorescent nv centers in diamond. *Chemical Physics*, 143(1):131–140, 1990.

[128] Eric W. Weisstein. Maximum likelihood. https://mathworld.wolfram.com/MaximumLikelihood.html. Publisher: Wolfram Research, Inc.

[129] John P Wikswo. Biomagnetic sources and their models. In *Advances in biomagnetism*, pages 1–18. Springer, 1989.

[130] John P Wikswo, John P Barach, and John A Freeman. Magnetic field of a nerve impulse: first measurements. *Science*, 208(4439):53–55, 1980.

[131] Wolfgang Wiltschko and Roswitha Wiltschko. Magnetic orientation in birds. *Journal of Experimental Biology*, 199(1):29–38, 1996.

[132] James K Woosley, Bradley J Roth, and John P Wikswo Jr. The magnetic field of a single axon: A volume conductor model. *Mathematical biosciences*, 76(1):1–36, 1985.

[133] H Xia, A Ben-Amar Baranga, D Hoffman, and MV Romalis. Magnetoencephalography with an atomic magnetometer. *Applied Physics Letters*, 89(21):211104, 2006.

[134] Chih-shiue Yan, Yogesh K Vohra, Ho-kwang Mao, and Russell J Hemley. Very high growth rate chemical vapor deposition of single-crystal diamond. *Proceedings of the National Academy of Sciences*, 99(20):12523–12525, 2002.

[135] Yafei Zhang, Chuanyi Zang, Hongan Ma, Zhongzhu Liang, Lin Zhou, Shangsheng Li, and Xiaopeng Jia. HPHT synthesis of large single crystal diamond doped with high nitrogen concentration. *Diamond and Related Materials*, 17(2):209–211, February 2008.

[136] Yali Zhao, Dan O Wang, and Kelsey C Martin. Preparation of aplysia sensory-motor neuronal cell cultures. *JoVE (Journal of Visualized Experiments)*, (28):e1355, 2009.